2007

# Self-assembled Lipid Tubules: Structures, Mechanical Properties, And Applications.

Yue Zhao
*University of Central Florida*

# SELF-ASSEMBLED LIPID TUBULES: STRUCTURES, MECHANICAL PROPERTIES, AND APPLICATIONS

by

YUE ZHAO
B.S. Tsinghua Univesity, 2004

A dissertation submitted in partial fulfillment of the requirements
for the degree of Doctor of Philosophy
in the Department of Mechanical, Materials and Aerospace Engineering
in the College of Engineering and Computer Science
at the University of Central Florida
Orlando, Florida

Fall Term
2007

Major Professor: Dr. Jiyu Fang

# ABSTRACT

Self-assembled lipid tubules are interesting supramolecular structures for both basic research and technological applications. In this thesis work, we have synthesized lipid tubules of 1,2-bis(tricosa-10,12-dinoyl)-*sn*-glycero-3-phosphocholine ($DC_{8,9}PC$) by self-assembly and polymerization in solutions. The structures of $DC_{8,9}PC$ lipid tubules are characterized by transmission electron microscope (TEM), atomic force microscope (AFM), and optical microscope. TEM images confirm that lipid tubules are hollow cylinders with open ends, indicating their high surface-area to volume ratio. The external diameters of $DC_{8,9}PC$ tubules are 0.5 μm with little variation, but their length varies from 5 μm to 100 μm, and their wall thickness varies from a single bilayer to a stack of 14 lipid bilayers. The self-assembly mechanism of $DC_{8,9}PC$ lipid molecules is studied by imaging molecular ordering in lipid tubules with liquid crystals as an optical amplification-probe. This work demonstrates for the first time that both uniform and modulated molecular tilt orderings exist in the tubule walls, which have been predicted by current theories.

Axial and radial mechanical properties of $DC_{8,9}PC$ lipid tubules are studied with different loading methods. We find that the interface tension of the shrinking liquid droplets exerts compression force on the ends of the trapped lipid tubules, and causes them to buckle. This provides an efficient method to measure their mechanical properties. The bending rigidity and axial Young's modulus is calculated to be ~ $2.6\times10^{-18}$ $Nm^2$ and ~ 1.07 GPa, respectively. As the strain energy of the buckled tubules build up, they poke through the interface of shrinking liquid droplets and then adhere onto glass substrates to

form looplike shapes. The persistence length of $DC_{8,9}PC$ lipid tubules is measured accordingly to be ~ 41 μm by applying worm-like chain model. Radial deformation of the $DC_{8,9}PC$ lipid tubules is studied using AFM tips as nanoindenters. From measured force-distance curves, a reversible linear region that persists up to indentations of 15% of the tubule diameter is observed. We find that the elastic responses of $DC_{8,9}PC$ lipid tubules is sensitive to the thickness of tubule walls and the position along the long axis of $DC_{8,9}PC$ tubules. Finite element models have been established to model the lipid tubule—AFM tip system and to simulate the indentation process. Comparing simulating results with experimental force-displacement curves, the radial Young's modulus is estimated to be 705 MPa for $DC_{8,9}PC$ lipid tubules. The difference in axial and radial Young's moduli suggests an anisotropy of $DC_{8,9}PC$ lipid tubules in terms of their mechanical properties. Other interesting mechanical behaviors such as recovery and surface stiffening are observed and their mechanisms are discussed.

Due to the high aspect ratio of lipid tubules, the hierarchical assembly of lipid tubules into ordered arrays and desired architectures, which is critical in developing some of their applications, remains to be challenging. Two efficient methods for fabricating ordered arrays of lipid tubules on solid substrates have been developed. In the first method, $DC_{8,9}PC$ lipid tubules are positioned and aligned by combining surface patterning and dipcoating. The moving contact line of air-liquid interface during the dipping process is able to align lipid tubules on patterned Au substrates formed by microcontact printing. The density, position, and orientation of lipid tubules on patterned Au substrates are controlled by adsorption time, surface pattern, withdrawal direction and rates. In the second method, $DC_{8,9}PC$ lipid tubules are aligned and confined in the

recessed channels of a thin poly(dimethylsiloxane) (PDMS) stamp with capillary action. We find that the aligned lipid tubules can serve as an "ink" for microcontact printing. 2-D ordered arrays and 3-D cross-bar junctions are constructed on planar Au-coated mica, patterned Au electrodes, and curved glass tubules. It is believed that these two methods will open up simple ways to integrate lipid tubules with current fabrication technology and devices.

The hollow cylindrical shape and molecular order of bilayer walls, coupled with moderate stiffness, make $DC_{8,9}PC$ lipid tubules attractive as templates for controlled deposition of inorganic nanomaterials. Hybrid silica-lipid tubes are synthesized by sol-gel condensation of tetraethoxysilane (TEOS) on $DC_{8,9}PC$ lipid tubules. Meanwhile, by filling nematic liquid crystal into parallel aligned $DC_{8,9}PC$ tubules, an ordered array of optical anisotropic fibers are formed. These hybrid materials have great potentials in heterogeneous chiral catalysis and separation, sensors, photonic devices, and optical communications.

This dissertation is dedicated to my parents, my family, and my fiancé Kin Fai Au, who have given me unending love and support throughout the years.

# ACKNOWLEDGMENTS

I would like to thank those who contributed and supported through my graduate studies at the University of Central Florida. First of all I would like to express my sincere appreciation to my advisor, Professor Jiyu Fang, for his guidance and support; knowing him has improved me as a researcher and as a person. I am grateful to him for providing me with the opportunity to work in the research area of bio-nano-materials and letting me leading several important projects. Without his support and help, I would not be able to have so many achievements in my research work and I can not be who I am today.

Much gratitude is owed to my dissertation committee members Porf. Ranganathan Kumar, Porf. C. Suryanarayana, Porf. Shin-Tson Wu, and Porf. Qun Huo, as well as non-committee member Prof. Linan An, for all that they have taught me through my graduate studies and for their helps with this endeavor.

Many thanks are expressed to Nidhi Mahajan for her help on laboratory experiments, discussions, and inspirations. I would also like to thank Dr. Robert Lu, Ms. Jing Liu, and Dr. Jianhua Zou for helping me with surface characterization and analytical instrumentation. Special thanks go to Dr. Richard Zarda, Mr. Hari Subramaniam, and Ms. Ruchi Dave, whose patience and helps with Finite Element Modeling and Stress Analysis has been invaluable. Mr. Peng Zhang is also acknowledged for his help with a number of photo-lithography-related issues. In addition, I wish to thank Diana Gavira, who conducted the contact line alignment mechanism studies in the spring 2007 as an undergraduate research student.

I would also like to express thanks to many colleagues and friends, who have not only provided help with my research, but also made my time in Orlando most enjoyable. Thanks go to (in no particular order): Mr Tao Jiang, Mr. Shipeng Qiu, Dr. Yi-Hsin Lin, Dr. Yung-Hsun Wu, Dr. Sebastian Gauza, Dr. Haiqing Xianyu, Mr. David W. Fox, Ms. Amanda Parish, Ms. Shuba, Mr. Prabahaker Mohan, Dr. Weifeng Fei, Mr. Robin Ge, Mr. Ravi Palaniappan.

Moreover, the research in this dissertation has been supported by the National Science Foundation. I appreciated the financial support of the Advanced Materials Processing and Analysis Center, University of Central Florida.

Finally, I express the utmost thanks to my beloved parents for their endless love and support; while most importantly, I would like to thank my fiancé Kinfai Au for his moral support and love for the past seven years as we both worked toward the final goal.

# TABLE OF CONTENTS

LIST OF FIGURES ..... XII

LIST OF TABLES ..... XVIII

CHAPTER 1 INTRODUCTION ..... 1

1.1 Background and Motivations ..... 1

1.2 Research Goals ..... 2

1.3 Outlines ..... 2

CHAPTER 2 SYNTHESIS AND CHARACTERIZATION OF LIPID TUBULES ..... 3

2.1 Introduction ..... 3
2.1.1 Self-Assembly of Materials ..... 3
2.1.2 Molecular vs. Material Self-Assembly ..... 6
2.1.3 Types and Examples of Self-Assembly in Materials Science ..... 7
2.1.4 Molecular Aspects of Lipid Tubule Formation ..... 8
2.1.5 Process Development of Lipid Tubules Preparations ..... 12
2.1.5.1 Thermally Grown Process ..... 12
2.1.5.2 Solvent Grown Process ..... 13
2.1.6 Theoretical Considerations for Lipid Tubules Formations ..... 14

2.2 Formation of Lipid Tubules ..... 17
2.2.1 Design of Lipid Molecules Based on Their Molecular Features ..... 17
2.2.2 Self-Assembly of Lipid Tubules ..... 18
2.2.3 Polymerization of Lipid Tubules ..... 19

2.3 Characterization of Lipid Tubules ..... 20
2.3.1 Transmission Electron Microscopy ..... 20
2.3.2 Atomic Force Microscopy ..... 21
2.3.3 Liquid Crystal Imaging ..... 21

2.4 Conclusion ..... 26

CHAPTER 3 MECHANICAL PROPERTIES OF LIPID TUBULES ..... 27

3.1 Introduction ..... 27
3.1.1 Solid-Liquid-Air Triple Contact Line ..... 28
3.1.2 Atomic Force Microscope ..... 28

3.2 Axial Bending ..... 29
3.2.1 Experimental Methods ..... 29
3.2.2 Results and Discussion ..... 29
3.2.2.1 Axial Bending Mechanism ..... 29
3.2.2.2 Bending Rigidity and Elastic Modulus ..... 31
3.2.2.3 Strain Energy ..... 34
3.2.2.4 Persistence Length and Relative Flexibility ..... 34
3.2.2.5 Substrate Effect ..... 37

3.3 Radial Compression ..... 38
3.3.1 Experimental Methods ..... 38
3.3.2 Results and Discussion ..... 41
3.3.2.1 Small Deformation—Elastic Properties ..... 41
3.3.2.1.1 Stiffness ..... 41
3.3.2.1.2 Young's Modulus ..... 43
3.3.2.1.3 Stress Analysis of the Modeled Tube with a Wall Thickness of 70nm ..... 45
3.3.2.1.4 Shape Analysis in Thin and Thick Walled Tubes ..... 48
3.3.2.1.5 Stress Analysis in Thin and Thick Walled Tubes ..... 49
3.3.2.2 Large Deformation-Pushing the Limits ..... 53
3.3.2.2.1 Hysteresis and Collapse ..... 53
3.3.2.2.2 Recovery ..... 55
3.3.2.2.3 Critical Force ..... 56
3.3.2.2.4 End Effect ..... 57
3.3.2.2.5 Surface Stiffening ..... 60

3.4 Conclusion ..... 66

CHAPTER 4 ORDERED ARRAYS OF LIPID TUBULES ..... 69

4.1 Introduction ..... 69
4.1.1 Soft Lithography ..... 69
4.1.2 Hierarchical Assembly of Lipid Tubules on Substrates ..... 70

4.2 Experimental Methods ..... 71
4.2.1 Surface Pattern and Dip-coating Method ..... 71
4.2.1.1 Surface Design ..... 71
4.2.1.1.1 Substrate ..... 71
4.2.1.1.2 Self-Assembled Monolayers (SAMs) ..... 72
4.2.1.2 Dip-Coating ..... 73
4.2.2 Directly printing method ..... 75

4.3 Results and Discussion ..... 76
4.3.1 Surface Pattern and Dip-coating Method ..... 76
4.3.1.1 Degree of Alignment vs. Withdrawal Rate ..... 77
4.3.1.2 Density of Alignment vs. Adsorption Time ..... 78
4.3.1.3 Density of Alignment vs. Withdrawal Times ..... 79
4.3.1.4 Degree of Alignment vs. Width of Au Stripes ..... 80

4.3.2 Directly printing method ..... 81
4.3.2.1 2-D Ordered Arrays ..... 81
4.3.2.1.1 On Planer Au Surface ..... 81
4.3.2.1.2 On Patterned Au Electrodes ..... 83
4.3.2.1.3 On Curved Glass Tubes ..... 84
4.3.2.2 3-D Ordered Arrays ..... 86

4.4 Conclusion ..... 87

CHAPTER 5 TUBULE ARRAY TEMPLATING ..... 89

5.1 Introduction ..... 89

5.2 Experimental Method ..... 90
5.2.1 Hybrid Silica-Lipid Tubes ..... 90
5.2.2 Optical Anisotropy Fibers ..... 91

5.3 Results and Discussion ..... 93
5.3.1 Hybrid Silica-Lipid Tubules ..... 93
5.3.1.1 Scanning Electron Microscopy ..... 93
5.3.2 Optical Anisotropic Fibers ..... 96
5.3.2.1 Formation and Characterization ..... 96
5.3.2.2 Optical Anisotropy ..... 98
5.3.2.3 Ordered Arrays by Microfluid Method ..... 101
5.3.2.4 Zigzag Shapes by Moving Contact Line Method ..... 103
5.3.2.5 Loop-like Shapes by Shrinking Contact Line Method ..... 104

5.4 Conclusion ..... 105

APPENDIX FEA PROGRAMMING CODES ..... 106

REFERENCES ..... 109

# LIST OF FIGURES

Figure 1 Features of self-assembly. (*A*) Aggregation occurs when there is a net attraction and an equilibrium separation between the components. (*B* and *C*) Schematic illustration of the essential differences between irreversible aggregation and ordered self-assembly. (*B*) Components (shown in blue) that interact with one another irreversibly form disordered glasses (shown in green). (*C*) Components that can equilibrate, or adjust their positions once in contact, can form ordered crystals if the ordered form is the lowest-energy form (shown in red)[12] ..... 4

Figure 2 Schematic representations of some lipid-based microstructures along with a dimension bar. ..... 8

Figure 3 (a) Molecular graphic representation of $DC_{8,9}PC$ lipid prepared by B. Gaber. (b) Schematic of the possible variations which can be made in a lipid that might have an effect on microstructure formation[26] ..... 10

Figure 4 Illustration of the formation of lipid tubules. The lipid molecules pack with a 45° with respect to their neighbors within a lipid bilayer, which usually has a height of 6.6nm. A stack of three lipid bilayers forms a bilayer stripe. The bilayer stripe twists into a helical ribbon and further twists to form a cylindrical tubule. ..... 16

Figure 5 (a) The chemical structure of a diacetylenic lipid $DC_{8,9}PC$, along with a space-filling model. (b) Schematic showing nonparallel packing of neighboring molecules in right- or left-handed fashion. ..... 18

Figure 6 Schematic representation of the topotactic polymerization of diacetylenic moieties. ..... 19

Figure 7 TEM image of lipid tubules. The hollow structure, open ends, and wall thicknesses of lipid tubules are clearly shown. The image was taken at a accelerating voltage of 300 kV ..... 21

Figure 8 AFM tapping mode image of lipid tubules in solution. The image was taken at a scan rate of 0.5 Hz. ..... 21

Figure 9 (a-d) Polarizing microscope images of a lipid tubule below Nematic 5CB. Arrows indicate the directions of polarizer and analyzer. (e) Plots of the intensity of the transmitted light as function of the angle between tubule and analyzer. ..... 24

Figure 10 Nonpolarizing (a) and polarizing (b) microscope images of a lipid tubule below the nematic liquid-crystal 5CB. (c) Plots of the intensity of the transmitted light as a function of the fractional distance across the width of the helical stripes. ..... 25

Figure 11 Optical microscopy images of the deformation of lipid tubules trapped in a shrinking liquid droplet on a glass substrate. The liquid droplet was dried in air at ~ 23°. The radius of the droplet base decreases with the solvent evaporation. The long lipid tubule circled in (a) remains straight until it encounters the shrinking contact line. The Laplace pressure associated with the interface causes the lipid tubule to buckle (b). As the strain builds up in the bent tubule, it pokes through the interface (c) and adheres on the glass substrate (d). The short lipid tubule circled in (c) directly pokes the interface without buckling. ..... 30

Figure 12 Schematic of a lipid tubule with both ends trapped a liquid droplet on a substrate. Where $\gamma$ is the interface tension of liquid droplet, and $\theta$ is the contact angle of water with the hydrophilic tubule. The force ($F_{comp}$), which is applied on the tubule end, is related to the interface tension: $F_{comp} = 2\pi r_e \gamma \cos\theta$, where $r_e$ is the external radius of the lipid tubule. ..... 31

Figure 13 (a) Optical microscopy image of lipid tubules with different lengths on a glass substrate. Dilute tubule solution was applied on the glass substrate. This image was taken after the tubule solution was completely dried in air at ~ 23°. The critical length of unbent tubules was estimated to be15 ± 0.2 μm from a number of optical images. (b) TEM image of a straight lipid tubule dried on carbon coated grids. The TEM image was taken at room temperature. ..... 33

Figure 14 (a) Optical microscopy image of a tubule loop with the projection of a vector ($l$). (b) A plot of the second moment as a function of vector length ($l$). The persistence length is determined from the inverse of the slop of the plot. (c) A plot of the fourth moment as a function of vector length ($l$) to check probability density $P(\theta(l))$ is Gaussian distribution. ..... 36

Figure 15 Histograms of the end-to-end distances (a) and the contour lengths (b) of bent lipid tubules on hydrophilic glass substrates and hydrophobic DDT monolayers with Gaussian distributions. The contour length and end-to-end distance were measured by digitizing the trace of these bent lipid tubules from optical microscopy images into pixels to give the spatial coordinates of each position along the tubules with MATLAB software. ..... 38

Figure 16 Instrumental set up of Nanoindentation by AFM. The essential components include: a tip mounted on a soft cantilever; a position sensitive photodetector to sense the cantilever's deflection by tracing the laser from the laser diode and reflected by the cantilever and mirror; a feedback loop collect the information from the photodetector and control an actuator driver to move the probe by applying a high voltage; a display system collects the deflection value from the feedback loop and converts them into an image or a force-distance curve. ..... 40

Figure 17 Measure and calculate effective spring constants of lipid tubules. (a) Typical force-distance curves taken on a single lipid tubule (black for loading, gray for unloading) and on glass slide (only show loading curve). The abscissa measures the vertical position of the tip. The point of contact between lipid tubule and tip is set to

z=0. The ordinate measures the force exerted by the tip on the sample, which is derived from the cantilever deflection using a calibration factor. (b) For one spot on one tubule, we applied repeated force for 100 times, the measured effective spring constants were plotted against the experiment number (count). (c) Histogram and Gaussian-fitted curves of effective spring constant smeasured from 31 individual lipid tubules. ..... 43

Figure 18 The FEM model was reduced to a quarter by considering axial symmetry. .... 44

Figure 19 Comparing experimental force-displacement curve and finite element simulation result, we got the Young's Modulus is 705 MPa for lipid tubules with 10 bilayers wall. ..... 45

Figure 20 Von Mises stress analysis for the modeled tubes with 70nm wall thickness under different loadings (F) and displacements (D). ..... 47

Figure 21 Cross section views of the initial and final states of two modeled tubes with thick walls and thin walls, respectively. The outer diameter of both tubes are 500nm, wall thickness is 70 nm for thick walls (a,b), and 14 nm for thin walls (c,d). At the indentation depth of 75nm, the thick walls still keep a convex shape (b) while the thin walls change from a convex to a concave shape (d). ..... 49

Figure 22 The contour plot of Von Mises Stress on tubule models with different wall thickness. With increasing tubule wall thickness from 1 bilayer to 25 bilayers (a-d), the maximum stresses at the same displacement (75nm) increased from 1.541 MPa to 6.009 MPa. ..... 50

Figure 23 FZ curves of lipid tubules on glass substrate in water. The loading force is shown as a function of the distance traveled downward by the cantilever from its initial raised position. Four successive force curves are shown. F1 and F2 show repeated small indentations, followed by a larger indentation (F3) beyond the reversible region. The purple-brown curve shows the hysteresis upon retraction. F4 shows a large indentation with a jump at the force beyond 1.5 nN, indicating a damage or collapse and the backward curve shows that the deformation is irreversible. ..... 54

Figure 24 (A-C) AFM image of a lipid tubule before and after indentations in water. The images taken time was indicated. (a-c) Plots of cross sections of tubule before and after indentation (a,b) and before and after recovery (b,c). ..... 56

Figure 25 Typical force-distance (FZ) curves of lipid tubules in water and illustrations of the tip-sample contacts. The FZ curves contain drops in the force, which manifests the buckling or collapse of tubular walls. We define the critical force as the force at which the drop begins. The indentation rate was 182nm/s. ..... 57

Figure 26 The contour plot of Von Mises stress on a finite element model of the deformed tube under a radial load. The radius of the indenter is 15nm, the maximum

displacement of the indenter is 27.75nm, and the deformed area extends in axial direction for about 30nm. ..... 58

Figure 27 AFM 2D (a) and 3D (b) image of a lipid tubule on glass substrate. The red arrow pointed the indentation direction and showed some of the indentation positions on the end of the lipid tubule. (c) Cross section plot of the tubule height along the dash line indicated in (a). ..... 59

Figure 28 End effect on normalized spring constant of the indentation force-distance curves (a) and the critical forces for lipid tubules collapse (b). ..... 60

Figure 29 (a) Contact mode AFM image of a $DC_{8,9}PC$ tubule on glass substrate in water. (b) Corresponding cross section of the dash line shown in (a). (c) Corresponding cross section of the solid arrow indicated in (a). The four dots in (a) pointed out the indentation positions. ..... 61

Figure 30 Curve fittings by finite element modeling. The dash line is experimental results extracted from FZ curves at positions with four different wall thicknesses. Solid lines are force-displacement relations got from finite element models. The optimized fitting results are: (a) 4 bilayers, E=1.4 MPa; (b) 6 bilayers, E=960 MPa; (c) 8 bilayers, E=715 MPa; (d) 10 bilayers, E=610 MPa. ..... 62

Figure 31 Schematic illustration of the surface stiffening model. Left: 3D view. Right: cross section view. The layer with organ color indicated the stiffening layer. ..... 64

Figure 32 Outer radius dependence of effective Young's modulus. Purple dots are experimental results, red line is fitted result by the surface stiffening model. ..... 66

Figure 33 Schematic illustration of the origin of anisotropic mechanical properties of $DC_{8,9}PC$ lipid tubules. A portion of lipid bilayer walls (a) without loading; (b) with axial loading; (c) with radial loading. The main resistance to axial deformation (b) came from polymerized ene-yne linkages between lipid molecules, while the radial deformation resulted in interdigitations between lipid layers (c). ..... 68

Figure 34 Schematic illustration of the combination of μCP (a) and dip-coating (c) to position and align lipid tubules. (b) Contact mode frictional force images of patterned Au substrate. (d) Tapping mode topographic image of aligned tubules. .. 74

Figure 35 Schematic illustration of aligning lipid tubules by the moving contact line method ..... 75

Figure 36 PDMS stamp with aligned lipid tube "ink". (a-c) Schematic illustration of the microfluidic technique used to align lipid tubes in the recessed channels of a thin PDMS stamp. (a) Rectangular capillaries were formed by placing a PDMS stamp on a glass substrate. A drop of tube solution was placed along the one of opened ends. (b) The alignment of lipid tubes in the rectangular capillaries by capillary action. (c) The PDMS stamp was removed from the glass substrate before the tube solution-

filled capillaries were dried. (d) Optical image of the aligned lipid tubes confined in the recessed channels of the PDMS stamp. ..... 76

Figure 37 (a) Optical microscope image of aligned lipid tubules on the patterned Au substrate. Histograms of the angles of the aligned lipid tubules away from the withdrawal direction with the fitted Gaussian distribution at the withdrawal rate of 1 mm/min (b) and 10 mm/min (c)..... 77

Figure 38 Optical microscope images of aligned lipid tubules on the patterned Au substrate at a constant withdrawal rate of 10 mm/ min after 1 h (a) and 12 h adsorption (b). (c) Plots of the density of the aligned tubules vs adsorption time.... 78

Figure 39 Optical microscope images of aligned lipid tubules on the patterned Au substrate by first (a) and second (b) withdrawal processes at a constant withdrawal rate of 10 mm/min. (c) Plots of the density of the aligned tubules vs withdrawal times at different withdrawal rates..... 79

Figure 40 Optical microscopy images of the lipid tubules absorbed on the patterned Au substrates. The width of the Au stripes is 2 μm (a) and 10 μm (b). These images were taken in tubule solution. ..... 80

Figure 41 2-D ordered arrays of aligned lipid tubules on planar Au-coated mica. Tapping-mode AFM images of parallel aligned lipid tubes with a constant separation (a) and varied separations (b) on Au-coated mica. (c) Fluorescence microscopy image of cyanine dye-loaded tubule arrays. The white arrow in (c) indicates a partially loaded lipid tubule ..... 83

Figure 42 2-D ordered arrays of aligned lipid tubules on patterned Au electrodes. Optical microscopy images of 2-D ordered tubule arrays printed on a square Au electrode (a) and stripe Au electrodes (b) which are fabricated on silicon wafers. Tapping mode AFM image (c) of an aligned tube across the stripe Au electrodes and high profiles (d and e) along the line 1 and line 2 shown in (c). ..... 84

Figure 43 2-D arrays of aligned lipid tubules on curved glass tubes. (a-b) Schematic illustration of printing 2-D ordered tubule arrays on a glass tube with a thin PDMS stamp inked with aligned lipid tubules. (c-d) optical microscopy images of 2-D tubule arrays on the glass tube at different focal planes. ..... 86

Figure 44 3-D cross-bar junctions of aligned lipid tubes on planar Au-coated mica. Tapping-mode AFM images of a cross-bar junction of two aligned lipid tubules (a and b) and a cross-bar junction network of aligned lipid tubules (c). Figure 3a was taken in air. Figures 3b and 3c were taken in a humidity chamber. ..... 87

Figure 45 Schematic illustration of formation of lipid tubule array-templated synthesis of aligned and patterned silica-lipid hybrid cylinders. ..... 91

Figure 46 (a) SEM image of 2-D arrays of templated silica-lipid hybird cylinders formed by sol-gel reaction of TEOS on tubule walls on Au-coated mica substrate. (b) Energy dispersive spectrum confirms the deposition of silica..... 93

Figure 47 FT-IR spectra of hybrid silica-lipid tubules placed on Au-coated mica. (a) Region between 3200 and 2600 $cm^{-1}$. (b) Region between 1500 and 70 $cm^{-1}$. The hybrid silica-lipid cylinders were dried on Au-coated mica and then were heated to 110 $^{\circ}$C for 2 h. The spectra represent an average of four scans taken with a 2 $cm^{-1}$ resolution at room temperature. ..... 95

Figure 48 (a) Schematic illustration of the filling process of lipid tubules with the 5CB. (b and c) Polarizing optical microscopy images of lipid tubules with the 5CB core. (d) AFM image of lipid tubules with the 5CB core. The directions of polarizer and analyzer were indicated by white arrays in b and c. The high profile along the white line drawn in d is inserted. ..... 97

Figure 49 (a-d) Polarizing microscopy images of lipid tubules with the 5CB core. Images were taken the sample was rotated in the plane between crossed polarizers. White arrows in (b) indicate the directions of polarizer and analyzer..... 99

Figure 50 (a) Plots of the intensity of the transmitted light through the tubules with the 5CB core as function of the angle between the direction of the tubules and the analyzer. The intensity measurements on different tubules were performed by image analysis with MATLAB software. (b) A possible alignment of the 5CB in the hollow core of the cylindrical tubule. ..... 100

Figure 51 (a-c) Schematic illustration of the microfluidic technique used to align lipid tubule on a glass substrate and the formation of 2-D ordered arrays of aligned lipid tubules with the 5CB core. (d) AFM image of parallel aligned lipid tubules on a glass substrate. (e) Polarizing optical microscopy image of the parallel aligned lipid tubules with the 5CB core. White arrows indicate the directions of polarizer and analyze. ..... 102

Figure 52(a) Schematic illustration of the moving contact line in a confined space method used to form zig-zag shaped lipid tubules on a glass substrate. (b) AFM image of a zigzag shaped lipid tubule on a glass substrate. (c) Polarizing microscopy image of the zigzag shaped optical anisotropic fiber formed by lipid tubules with a 5CB core. White arrows in (c) indicate the directions of polarizer and analyzer. ..... 103

Figure 53 (a) Schematic illustration of the shrinking contact line of a droplet method used to form loop-like shaped lipid tubules on a glass substrate. (b) AFM image of a loop-like shaped lipid tubule on a glass substrate. (c) Polarizing microscopy image of a loop-like shaped optical anisotropic fiber formed by lipid tubules with a 5CB core. White arrows in (c) indicate the directions of polarizer and analyzer ..... 104

# LIST OF TABLES

Table 1 Summary of important examples of SA in materials science. ..... 7

Table 2 Comparisons of finites element models of lipid tubules with different wall thickness. ..... 52

Table 3 Young's Modulus of the lipid tubule (LT) decreased with increasing outer diameters. ..... 63

Table 4 Comparisons of methods for aligning and assembly lipid tubules. ..... 88

# CHAPTER 1
# INTRODUCTION

## 1.1 Background and Motivations

There has been much excitement about the possibility of using nano- and micro-sized structures for real world applications[1]. Molecular self-assembly is being used to fabricate microstructures that may have potential for material applications[2]. Learning from nature, biomolecular self-assembly is being used to construct microstructures on many different size scales[3]. Atomic force and scanning tunneling microscopy techniques are being used for atomic and molecular-scale manipulatio[4]. The enhanced understanding of the role of molecular architecture in determination of material properties coupled with the development of characterization techniques in nanoscales suggests that this area is ripe for breakthroughs.

This dissertation describes one approach based upon the molecular self-assembly of lipids to form submicrometer diameter tubules with the potential for real world applications. In order to use self-assembled lipid tubules for material development, several issues must be well addressed. First, the mechanism of the lipid tubules formation must be clearly understood. Second, the geometry features, physical properties, and chemical functionalities of lipid tubules must be well characterized. Third, methods must be developed to precisely control their density, position and orientation (hierarchy assembly) on different substrates. Finally, techniques must be advanced to utilize their geometries, properties, and hierarchy assemblies for real world applications. By addressing these four issues, this thesis work provides a paradigm for molecularly engineered structures.

## 1.2 Research Goals

The research presented here focuses on the following issues:

1. Synthesis and characterization of lipid tubules.

2. Mechanical properties of lipid tubules.

3. Hierarchical assembly of lipid tubules into ordered arrays on solid substrates.

4. Applications of 2-D ordered arrays of lipid tubules in templating and encapsulations.

## 1.3 Outlines

This work is structured according to the route of material design and development: structure—property—assembly—application. The first chapter briefly introduces the background of self-assembled lipid tubules and provides the impetus for investigating them. Chapter 2 describes lipid tubules, especially the lipid tubules of 1,2-bis(tricosa-10,12-dinoyl)-sn-glycero-3-phosphocholine ($DC_{8,9}PC$), in terms of their synthesis methods, formation mechanisms, and structural features. The subsequent unveiling of molecular ordering in tubule walls illuminates the key features which control the structures and mechanical properties of $DC_{8,9}PC$ tubules. In Chapter 3, mechanical properties of $DC_{8,9}PC$ tubules are studied by axial bending and radial compression. Elastic and plastic deformations of $DC_{8,9}PC$ tubules, along with their failure mechanisms, are discussed in details. Chapter 4 concentrates on the formation of ordered arrays of $DC_{8,9}PC$ tubules on solid substrates. In Chapter 5, applications of 2-D ordered arrays of $DC_{8,9}PC$ tubules in templating and encapsulations are covered.

# CHAPTER 2
# SYNTHESIS AND CHARACTERIZATION OF LIPID TUBULES

This chapter begins with a introduction of features, types, and examples of the self-assembled materials, and followed by a literature review of the formation of lipid tubules, especially the lipid tubules of 1,2-bis(tricosa-10,12-dinoyl)-*sn*-glycero-3-phosphocholine ($DC_{8,9}PC$). After that, synthesis methods of $DC_{8,9}PC$ tubules are described. Formation mechanisms of $DC_{8,9}PC$ tubules are theoretically discussed and experimentally validated. The size, shape, and molecular ordering of $DC_{8,9}PC$ tubules were characterized by electron microscopy technique, scanning probe microscopy technique, and liquid crystal imaging technique.

## 2.1 Introduction

### 2.1.1 Self-Assembly of Materials

Self-assembly (SA) is the autonomous organization of components into patterns or structures without human intervention[5]. There are six distinctive features of SA systems need to be taken into consideration.

First, the component of SA is not limited to molecules. Although the concepts of SA were developed with molecules, and self-assembling processes currently are best understood and most highly developed for molecules, components of any size (from molecules to galaxies) can self-assemble in a permissive environment[6]. Usually, a self-assembling system consists of a group of molecules or segments of a macromolecule that

interact with one another. These molecules or molecular segments may be the same or different.

Second, SA occurs when molecules interact with one another through a balance of attractive and repulsive interactions (Fig.1.A). These interactions are generally weak and noncovalent (van der Waals and Coulomb interactions, hydrophobic interactions, and hydrogen bonds) but relatively weak covalent bonds (coordination bonds) are recognized increasingly as appropriate for self-assembly[7,8]. By far, weak interactions still play a key role in the formation of the SA system, and SA extends the scope of chemical bonds to weak interactions[9].

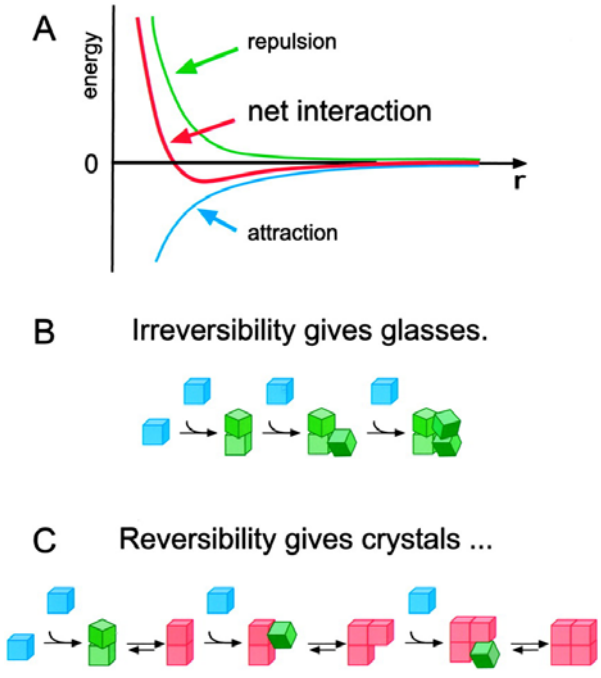


**Figure 1 Features of self-assembly. (*A*) Aggregation occurs when there is a net attraction and an equilibrium separation between the components. (*B* and *C*) Schematic illustration of the essential differences between irreversible aggregation and ordered self-assembly. (*B*) Components (shown in blue) that interact with one another irreversibly form disordered glasses (shown in green). (*C*) Components that can equilibrate, or adjust their positions once in contact, can form ordered crystals if the ordered form is the lowest-energy form (shown in red)[12].**

Third, the interaction between components leads them from some less ordered states (a solution, disordered aggregate or random coil) to a final state (a crystal or folded macromolecule) that is more ordered. This feature differentiates SA from common chemical reactions, where an ordered state may proceed towards a disordered state according to thermodynamic parameters.

Fourth, the thermodynamic stability allows SA process happening spontaneously. In covalent synthesis and polymerizations, scientists link atoms together in almost any desired conformation; self-assembling molecules, on the other hand, adopt a structure at the thermodynamic minimum (energetically most favored position). This thermodynamic stability also leads self-assembled structures to be relatively free of defects[10].

Fifth, the environment of SA normally is in solution or at an interface to allow the required motion of the components. The interaction of the components with their environment can strongly influence the course of the process. The sensitivity to external perturbations makes it possible to exert a fine control on the SA processes in order to obtain complex architectures[11].

Sixth, the reversibility or adjustability allows for formation and maintenance of the SA system. From the view of formation of ordered structures, the association must either be reversible or allow the components to adjust their positions within an aggregate once it has formed (Fig. 1B). The strength of the bonds between the components, therefore, must be comparable to the forces tending to disrupt them. For molecules, the forces are generated by thermal motion. Contrastingly, processes in which collision between molecules leads to irreversible sticking generate glasses, not crystals (Fig. 1C). From the view of maintenance, weak interactions allow rearrangements of the structure if

thermodynamic parameters change. If fluctuations further bring the thermodynamic variables back to the starting condition, the structure is likely to go back to its initial configuration.

The above six features of common SA systems is the base and guideline of our studies in the synthesis and characterizations of lipid tubules. As the self-assembly of lipid tubules involves both molecular assembly and ordered aggregation, it is helpful to grasp the similarities and differences of self-assembly at molecular level and beyond. It is also convenient to get a big picture of the catalog to which the self-assembled lipid tubules belong, by sorting SA and summarizing important SA examples in materials science.

### 2.1.2 Molecular vs. Material Self-Assembly

Molecular self-assembly can be defined as a process in which molecular units spontaneously form ordered molecular organizations, with structures and properties which are not found in the individual components[12]. The driving forces for this molecular organization are quite varied and can be non-covalent or weak covalent interactions (van der Waals, electrostatic, hydrogen and coordination bonds, and hydrophobic interactions)[13,14].

Material self-assembly chemistry transcends that of molecular assembly. It is distinct solid-state materials chemistry, where building blocks and their assemblages are unconstrained by scale and not restricted to just chemical bonding forces. The way to view material self-assembly over "all" scales is in terms of a map of bonding forces that over different length scales. In the self-assembly of larger components—meso- or

macroscopic objects—the forces responsible for material self-assembly include capillary, colloidal, elastic, electric, magnetic and shear.

### 2.1.3 Types and Examples of Self-Assembly in Materials Science

There are two main kinds of self-assembly: static and dynamic: static self-assembly (S) and dynamic self-assembly (D). The former one involves systems that are at global or local equilibrium and do not dissipate energy. For example, molecular crystals[6,15] are formed by static self-assembly; so are most folded, globular proteins. In static self-assembly, the formation of ordered structures may require energy (for example in the form of stirring), but once it is formed, it is stable. In dynamic self-assembly, the interactions responsible for the formation of structures or patterns between components only occur if the system is dissipating energy. The patterns formed by competition between reaction and diffusion in oscillating chemical reactions[16] are simple examples; biological cells are much more complex ones. The study of dynamic self-assembly is in its infancy.

Some important examples of SA in materials science are summarized in Table 1.

**Table 1 Summary of important examples of SA in materials science.**

| System | Type | Applications | Reference |
|---|---|---|---|
| Atomic, ionic, and molecular crystals | S | Optoelectronics | 17, 15, **Error Bookmark n defined.** |
| Lipid bilayers and lipid tubules | S | Biomembranes | 18 |
| Self-assembled monolayers (SAMs) | S | Microfabrication, sensors | 19 |

| | | | |
|---|---|---|---|
| Liquid crystals | S | Display | 20 |
| Macro- and mesoscopic structures | S or D | Electronic circuits | 21, 22, 23 |
| Oscillating reactions | D | Biological oscillations | 16 |
| Swarms and schools | D | Models for optimization | 24, 25 |

### 2.1.4 Molecular Aspects of Lipid Tubule Formation

Any serious attempts to use molecular self assembly for advanced material development must begin with a rational understanding of the relation between the molecular structure and the microstructure derived from it. A schematic representation of some of the structures that have been observed from lipid self-assembly is shown in Figure 2[26].

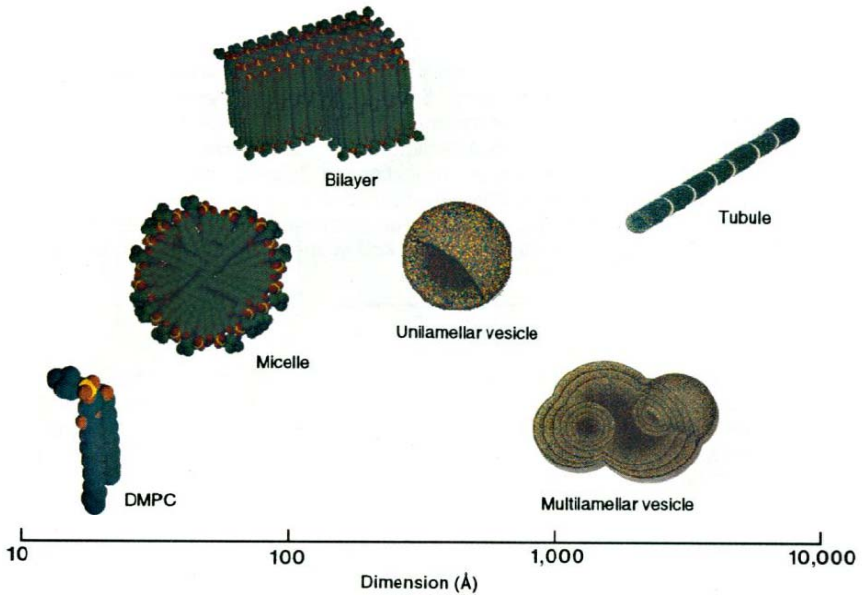


**Figure 2 Schematic representations of some lipid-based microstructures along with a dimension bar.**

Phospholipids are the basic building blocks of biological membranes. The fundamentals of self-assembled phospholipids micro- and nano- structures have been discussed in several recent books [27, 28] and review articles [29]. Since early 1980s, modifications to the molecular structure of phospholipids have been made to increase the versatility of liposomes as delivery agents for pharmaceutical agents[30]. Phospholipids with photopolymerizable diacetylenic moieties in the acyl chains were synthesized to increase the durability of liposomes[31,32,33]. Meanwhile, in 1983, Yager and Schoen observed the formation of a hollow cylindrical structure in copious quantities while studying the properties of the polymerizable diacetylenic phospholipid,1,2-bis (tricosa-l0,l2-diynoyl)-*sn*-glycero-3-phosphocholine ($DC_{8,9}PC$) [34]. These tubules appear to be similar in shape to a paper soda straw, with a diameter of 500nm, with lengths varying from a few to several hundred micrometers and wall thickness of 10 to 60 nm or more. The size and stability of tubules formed in water are sensitive to preparation conditions and thermal history[35,36]. Later on, in 1987, longer and more robust tubules were formed by different methods[37].

There are many molecular features that appear to be relevant to the self-assembly of tubular microstructures. These are shown in Fig. 3 along with a molecular graphic representation of $DC_{8,9}PC$. From the middle 1980s, Singh synthesized a number of molecules to assess the effect of variation of molecular features on the self-assembly of cylindrical microstructures. His first efforts were the synthesis of diacetylenic positional isomers of $DC_{8,9}PC$[38,39,40]. In 1988, detailed microscopic, calorimetric, and Fourier transform infrared (FTIR) spectroscopy studies have been conducted on the 27-

carbon acyl chain series ($DC_{m,n}PC$) with m varying from 4 to 15 and n varying from 6 to 17[41].

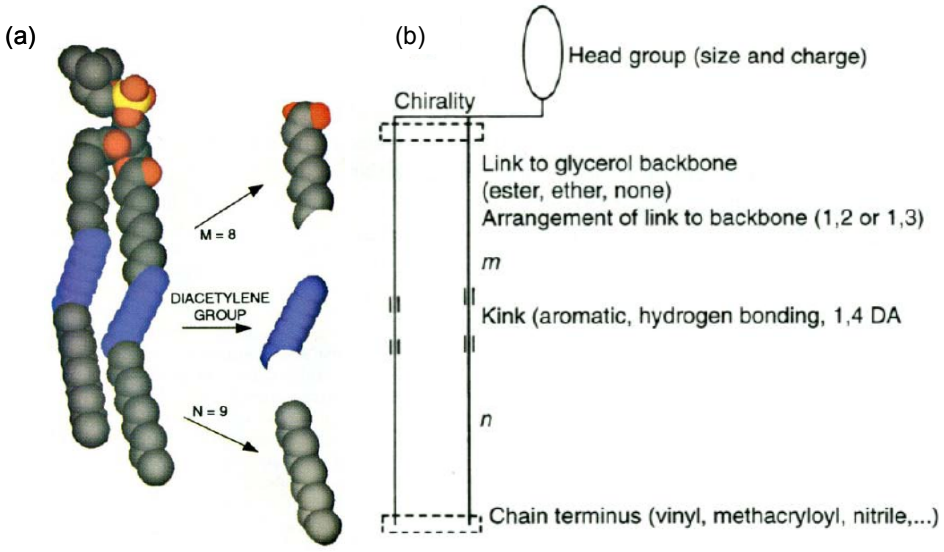


**Figure 3 (a) Molecular graphic representation of $DC_{8,9}PC$ lipid prepared by B. Gaber. (b) Schematic of the possible variations which can be made in a lipid that might have an effect on microstructure formation[26]**Error! Bookmark not defined.**.**

The most salient results of these studies were:

1) The nondiacetylenic versions of these molecules did not form tubules.

2) Molecules with nonsymmetrical positions of the diacetylenes in the acyl chain did not form tubules (m is not equal to n).

3) The position of the diacetylene group had little or no effect on the observed structure of tubules formed from these substances.

4) The acyl chains had very high *trans* conformational order.

FTIR and Raman studies on these materials suggest that the conformational order of acyl chains in the tubule morphology is very high[42,43]. X-ray diffraction and electron scattering studies have also been performed on wet tubules, on the

polycrystalline powder, and on Langmuir films made from $DC_{8,9}PC$[44,45,46]. The results are consistent with minimal interleaving of acyl chains and with the high *trans* conformational order observed the vibrational studies discussed above. Taken together, the studies described above suggest that the structure of the acyl tails is a significant feature for the formation of tubules.

In the late 1980s and early 1990s, after the effects of diacetylenic positional isomerization were studied, an investigation on the role of head group in tubule formation was carried out by Singh and his coworkers[47]. They found a nonchiral head group attached to similar acyl tails, as in the $DC_{8,9}PC$ molecule, did not form tubules but did form sheet-like structures that curled. Subsequently, a number of diacetylenic lipids with varying chirality, size, and charge of the head group were synthesized[48]. Cylinders were not initially observed in the case of solutions of lipids with chiral charged head groups[49]. When metallic counterions were added in the solutions, cylindrical structures with diameter of ~50nm or ~600nm were observed[50,51,52].

One technique that has been proved particularly useful in studying chiral lipid architectures is circular dichroism (CD) spectroscopy. Circular dichroism, the difference in the absorption of right and left circularly polarized light, arises from the chirality of the molecular architecture. This chirality can arise from either the structure of individual molecules or the chiral packing of molecules into larger aggregates. Kunitake et al. found that chiral bilayers can show greatly enhanced CD spectra[53]. $DC_{8,9}PC$ tubules were also found to have intense peaks in their CD spectra indicating large chiral correlations in the molecular packing[54]. This chiral order can no longer be maintained when the chains

became disordered at temperature above $T_m$, leading to a decrease in CD peak intensity by four orders of magnitude.

In 1996, CD experiments revealed that, in addition to chiral packing within the $DC_{8,9}PC$ bilayer, chiral correlations exist between bilayers in multi-bilayer tubules[55]. For the $DC_{8,9}PC$ single bilayer tubule formed in methanol/water solution, a sharp peak at 195 nm associated with chiral packing of the diacetylene group is the predominant spectral feature, while a broader peak at 202 nm due to chiral ordering of headgroups is seen in the multi-bilayer tubule formed in ethanol/water. The loss of chiral order is also reflected in the CD spectrum for $DC_{8,9}PC$ liposomes above the lipid melting temperature, where the peak magnitude is $10^4$ times smaller than that from the tubule[56].

In 1998, Thomas and coworkers have synthesized an analogue of $DC_{8,9}PC$ where the phosphate linkage between the choline headgroup and glycerol backbone is replaced by a phosphonate[57]. They find the tubules formed under similar conditions have twice the diameter of $DC_{8,9}PC$ tubules, but also to be significantly more fragile.

From above studies, it would seem that a highly ordered acyl tail, an "appropriate head group", and some degrees of chirality are requirements for lipid tubule formation.

### 2.1.5 Process Development of Lipid Tubules Preparations

#### 2.1.5.1 Thermally Grown Process

Thermally grow method involved raising the temperature of an aqueous vesicular dispersion above the chain melting temperature, $T_m$, of the diactylenic lipid (43°C for $DC_{8,9}PC$) followed by slow cooling to just below Tm as described by A. Singh

and J. Schnur[34,38,58]. Lipid tubules formed during the cooling process, where the lipid bilayers changed from the fluid lamellar phase (chain disordered phase), known as $L_\alpha$ phase, into the lamellar phase having crystal-like order, called $L_{\beta'}$ gel phase. Lipid tubules formed rapidly as the phase transition was passed. The structures formed are referred to as "thermally-grown tubules". Rudolph, Burke, and coworkers improved the formation efficiency by cycling the process[59]. This process led to almost 100% conversion of lipids into tubules.

2.1.5.2 Solvent Grown Process

Although the thermal process is attractive, it does not seem likely that this approach can lead to the easy production of large (kilograms to tons) amounts of lipid tubules because of the difficulty in controlling the required homogeneous temperature in very large vats. In order to overcome this problem, a process was developed for the formation of tubules in ethanol/lipid/water solution at constant temperature or over a narrow temperature range[37]. Two approaches have been used: (i) adding water to an ethanol solution of the diacetylenic lipid; and (ii) lowering the temperature of the ethanol/water/lipid solution until tubules precipitate. Lipid tubules formed in those manners are referred to as "solvent grown tubules".

By varying the initial conditions, some of the morphological properties of the resulting microstructures can be controlled. When a racemate is used, both left- and right-handed helices are formed as well as tubules[60]. The average lengths of the tubules were also found to be a function of the ethanol-water ratio. However, there was always a wide variation (greater than a factor of 2) in the lengths at all concentrations, with the median length from 12 to 170 microns. If temperature is precisely controlled, median lengths of

500 microns can be obtained. Indeed, tubules with length larger than 1200 microns were observed in the latter case. These tubules also exhibit a variation of the number of bilayers formed in tubule walls[61].

Rudolph et al.[62] observed that tubules could precipitate from acetonitrile suggests that bulk water is not a prerequisite for tubule formation. In contrast, liposomes require a water solution for formation, which suggests a different mechanism of formation. These results provide further evidence that features of the resulting microstructures can be controlled by varying the formation conditions.

### 2.1.6 Theoretical Considerations for Lipid Tubules Formations

In order to seriously consider the use of molecularly assembled microstructures in a general sense, it is important to understand the relation between the structure of the individual molecules comprising the microstructure and the geometry of the microstructures. If this is well understood, then it should be possible to tune the geometry for a particular application. Unfortunately, the level of our understanding has not yet reached at molecular level. However, there has been progress in macroscopic and continuum theory of tubules.

There have been three general approaches in the theory of tubule formation. First, de Gennes has argued that a narrow strip of a tilted chiral bilayer will buckle to form a tubule because of its spontaneous electric polarization[63]. His theory predicts that adding electrolytes to the solvent should increase the tubule diameter, because the electrostatic attraction would be screened by electrolytes in solution. However, experiments have shown that electrolytes in solution do not affect the formation or radius of tubules[64],

except for the particular case of tubules composed of amphiphiles with charged head groups[50]. Thus electrostatic interaction is probably not a dominant factor in tubule formation.

As the second theoretical approach, Lubensky and Prost developed a general phase diagram for membranes with in-plane orientational order, which predicts hollow cylinders as well as spheres, flat disks, and tori[65]. This theory predicts that the dimensions of the cylinders are determined by competition between edge and curvature energy. However, the predicted scaling of the diameter as a function of the length is not observed experimentally. Thus the competition between edge energy and curvature energy is also not a dominant factor in tubule formation.

The third approach, which is consistent with the experimental results on lipid tubules, is based on the chiral packing of the molecules in a membrane. Helfrich and Prost have shown that a tilted chiral bilayer will form a cylinder because of an intrinsic bending force strictly due to chirality[66]. Ou-Yang and Liu have developed a version of this theory based on an analogy with cholesteric liquid crystals[67,68]. Chappell and Yager have developed an analogous theory in which the direction of one-dimensional chains of molecules, rather than the direction of molecular tilt, defines a vector order parameter within the membranes[69,70]. Nelson and Powers have used the renormalization group to calculate the effects of thermal fluctuations on tubules[71,72]. Selinger and Schnur have advanced similar arguments to explain the helical substructure commonly seen in tubules[73]. The fundamental basis of this theoretical approach is that the interaction between molecules in bilayers is chiral. This chirality normally results from the three-dimensional chirality of the molecules, but it can also result from chiral symmetry

breaking in the arrangement of nonchiral molecules in the bilayer[47]. Because of this chirality, the molecules do not pack parallel to each other; each molecule instead packs at some favored angles with respect to its nearest neighbors. This favored twist from molecule to molecule leads the bilayer to twist out of the plane and to form a ribbon. Then, the ribbon closes its gaps to form a tubule (Fig.4). Very recently, Tu and Seifert have developed a concise theory of chiral lipid membranes (CLMs) and predicted that tubules with helically modulated tilting state are not equilibrium structures while the helical ripples in tubules are equilibrium structures[74].

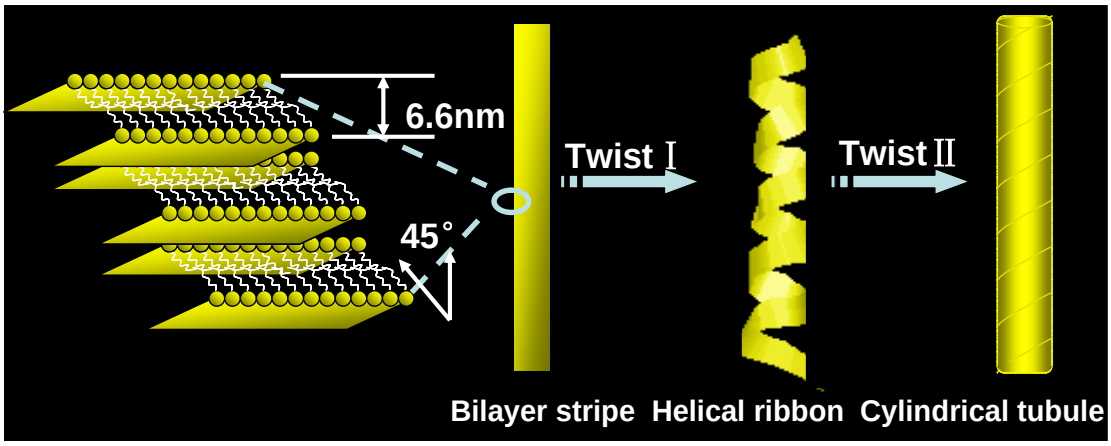


**Figure 4 Illustration of the formation of lipid tubules. The lipid molecules pack with a 45° with respect to their neighbors within a lipid bilayer, which usually has a height of 6.6nm. A stack of three lipid bilayers forms a bilayer stripe. The bilayer stripe twists into a helical ribbon and further twists to form a cylindrical tubule.**

It is interesting to note that tubular and helical structures seem to be rather common in nature. The recent flurry of activities in the area of nanotubes is a case in point[75,76]. It would not be surprising if some of the theoretical issues being addressed in lipid tubule formation were relevant to other cases of tubule or helix formation. For instance, structures strikingly similar to lipid tubules have been observed from

cholesterol-based solutions in bile[77]. These observations suggest that the chiral packing factors that affect tubule formation lead to molecular self-assembly of similar microstructures in a number of other systems.

## 2.2 Formation of Lipid Tubules

### 2.2.1 Design of Lipid Molecules Based on Their Molecular Features

The issues we have taken into consideration in designing and choosing lipid molecules are essentially molecular chirality and molecular rigidity. As we know, most chiral lipids form liposome (spherical bilayers vesicles) but not tubules or helical ribbons. Advancing the chiral assembly theory, we figured that it would be very helpful to put a kink into the acyl chains of lipid molecules. Indeed, the most striking feature of diacetylenic lipids is that the diacetylene group puts a kink into the acyl chain of the molecules, which can be seen in the space-filling model of Fig. 5(a). This kink imposes a steric hindrance to the molecules packing parallel to each other. Hence, the optimum packing of two neighboring molecules can have either of the two arrangements shown in Fig. 5(b). If the molecules had no stereocenter, those two arrangements would be degenerate. Because the molecule is chiral, the degeneracy between the two arrangements is lifted, and one of them is favored. This favored packing of molecules causes the favored twist of the lipid bilayer.

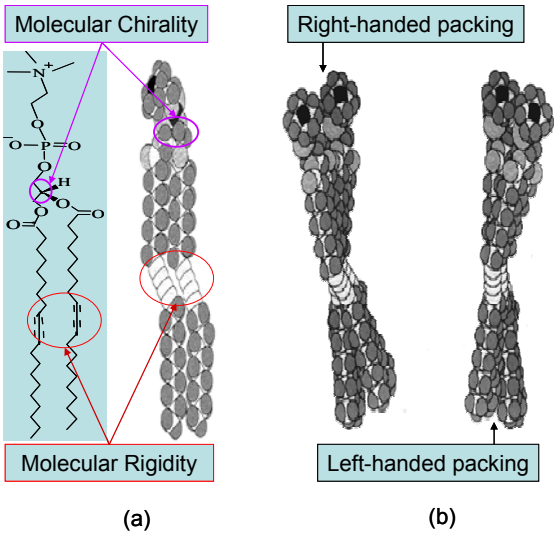


**Figure 5 (a) The chemical structure of a diacetylenic lipid $DC_{8,9}PC$, along with a space-filling model. (b) Schematic showing nonparallel packing of neighboring molecules in right- or left-handed fashion.**

Another important feature is strong intermolecular interactions, which can be transmitted through hydrogen bonding. Because of these interactions, the molecular shape strongly affects the way that neighboring molecules pack together, giving a strong preference for nonparallel alignment of molecules.

One point should be emphasized: the special feature of diacetylenic lipids is not the stereocenter, but rather the strong preference for some nonparallel packing of the molecules. The molecular chirality then selects a particular type of packing.

### 2.2.2 Self-Assembly of Lipid Tubules

In order to generate large amount (kilogram), long and relatively strong lipid tubules, we chose the solvent grown method to produce lipid tubules. First, we prepared a mixed solvent system of 70% ethanol and 30% water by volume, with 1,2-bis(tricosa-10,12-diynoyl)-*sn*-glycero-3-phosphochloline ($DC_{8,9}PC$) (Avanti Polar Lipids, Alabaster,

AL) concentration of 5mg/mL. Then, we heated the mixed solvent system to just above the chain melting temperature of $DC_{8,9}PC$ (43°C), followed by cooling of the mixture at a rate of ~0.5°C /min. The lipid tubules were precipitated at 27 °C.

Detailed optical and electron microscopy studies shows that the average length and inner diameter of lipid tubules depend on the cooling rate and solvent, while the outer diameter is independent on the cooling rate and solvent. Decreasing cooling rate has been found to increase the length and decrease the inner diameter of lipid tubules. Lipid tubules precipitated from a methanol/water solution have only single bilayer wall, with the thickness of ~8nm[78]; while lipid tubules obtained from ethanol/water or water have multiple bilayers walls.

### 2.2.3 Polymerization of Lipid Tubules

Lipid tubules were undergo the free-radical topotactic polymerization by a 1,4-reaction of the acetylenic carbons, when exposured to photons or electrons of sufficient energy, such as can be produced by ultraviolet (UV) radiation (in our case, 254nm UV irradiation for 20 mins at room temperature).

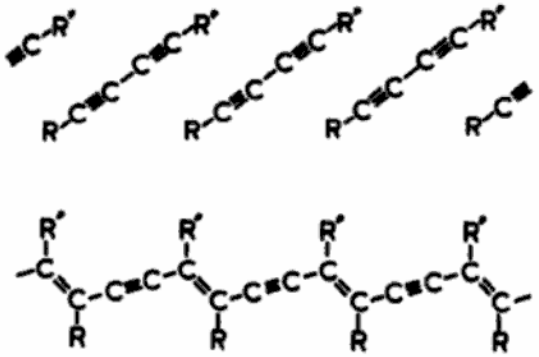

**Figure 6 Schematic representation of the topotactic polymerization of diacetylenic moieties.**

The topotactic polymerization of diacetylene is generally known to be acutely sensitive to the molecular order of molecular assemblies[79]. The particular molecular configuration and interaction leads to a well defined reaction product. In bulk reactions, the product is amorphous because the molecular order is destroyed during the reaction. In topochemical reactions, the product is topotactic as the reaction path is totally determined by the molecular order of the initial molecular assemblies. Different from bulk and topochemical reactions, topotactic reactions produce a product phase which has a small number of orientations with respect to the initial crystal[80]. The schematic representation in Figure 6 shows the orientation changes of diacetylenic moieties during topotactic polymerization.

## 2.3 Characterization of Lipid Tubules

### 2.3.1 Transmission Electron Microscopy

Transmission electron microscopic (TEM) measurements of $DC_{8,9}PC$ lipid tubules on carbon-coated grids were performed on a Tecnai F30 microscope with an accelerating voltage of 300 kV at room temperature. From TEM bright field image (Figure 7), it can be seen that the $DC_{8,9}PC$ tubules are hollow cylinders with two open ends, and both the internal surface and external surface are exposed to the aqueous environment. Therefore, they have high surface-area to volume ratio. We also found that $DC_{8,9}PC$ lipid tubules have an uniform outer diameter around 500nm, varied wall thickness from 7 nm to 100 nm, corresponding to a single $DC_{8,9}PC$ lipid bilayer to a stack of 14 lipid bilayers.

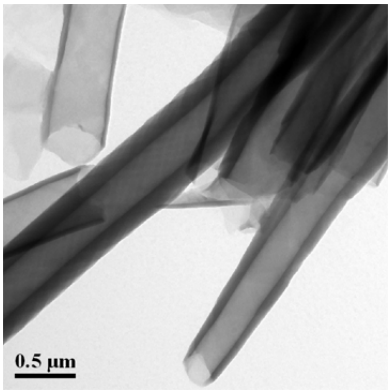


**Figure 7 TEM image of lipid tubules. The hollow structure, open ends, and wall thicknesses of lipid tubules are clearly shown. The image was taken at a accelerating voltage of 300 kV.**

### 2.3.2 Atomic Force Microscopy

Atomic force microscope (AFM) tapping mode image (Figure 8) shows that lipid tubules have different lengths in the range from 5 µm to 100 µm, all depends on the condition under which the self-assembly happens. Then, the aspect ratio spans the range between 10 and 200.

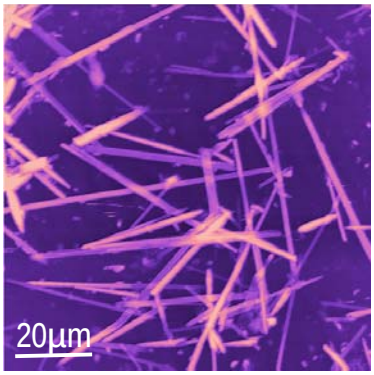


**Figure 8 AFM tapping mode image of lipid tubules in solution. The image was taken at a scan rate of 0.5 Hz.**

### 2.3.3 Liquid Crystal Imaging

Liquid-crystal imaging is a technique based on *liquid-crystal optical amplification*. As we know, liquid crystals are highly anisotropic fluids, in which molecules have long-range orientational order, but little positional order. This unique

feature permits liquid crystals to act as a sensitive material. The energy required to perturb the molecular order of liquid crystals is very small, and any defect or non-uniformity of the surface in contact with the liquid crystals leads to changes in the local order[81,82]. The surface-induced changes in the molecular order can extend over tens of micrometers into the bulk liquid-crystal phase on time scales of milliseconds. This in turn leads to observable optical patterns or textures in a polarizing optical microscope.

A drop of a tubule solution was placed and then dried on octadecyltrichloro-silane monolayer coated glass slides, which generate homeotropic alignment of liquid crystals. Sealed cells containing 4-pentyl-4'-cyanolbiphenyl (5CB) (BDH) or MLC-6609 (EM Laboratories, Elmsford, NY) liquid crystals were prepared with two glass slides. The $DC_{8,9}PC$ tubules were deposited on one of them. The two glass slides were separated by a 25μm Mylar spacer. Liquid-crystal orientation in the cells was examined by using a polarizing optical microscope (BX 40, Olympus), and images were captured by using a digital camera (C2020 Zoom, Olympus) mounted on the microscope. For the polarizing microscope, the optics was adjusted to complete extinction before placing samples on the stage.

It is known that birefringent liquid crystals can change the incident polarization by splitting linearly polarized light into two perpendicularly polarized components, thus creating an elliptically polarized beam of light with a component capable of passing through the analyzer. However, when the incident light beam is vibrating parallel to the optical axis of liquid crystals, they appear dark under crossed analyzer because there is no splitting of the beam, and this position is termed as extinction position**.** As long as the liquid crystal rotates away from the position of extinction, splitting of the beam occurs,

and they appear bright. Therefore, the brightness of liquid crystals viewed under crossed polarizer and analyzer relates to their orientation with respect to the polarization angle.

Figure 9 shows liquid-crystal 5CB images of a lipid tubule between crossed polarizer and analyzer. We found that the tubule is bright if the direction is parallel to the polarizer (Figure 9 a and c), and it becomes dark if the direction of its axis is 45° to the polarizer (Figure 9 b and d). Image analysis was preformed with MATLAB software. We measured the intensity of the transmitted light through the 5CB anchored on the surface of six tubules during their rotation to quantify the uniformity of azimuthal orientation of the 5CB with the image analysis. A strong modulation in the intensity of the transmitted light was observed (Figure 9e). The tubules show the maximum transmittance when they are parallel to the polarizer and the minimum transmittance when they are orientated by 45° with respect to the polarizer. In the dark state of lowest intensity (position of extinction), the liquid crystal should be parallel to either the polarizer or the analyzer, which is 45° to the tubule axis. Therefore, these measurements led us to conclude that the lipid tubules induce uniform azimuthal orientation of the 5CB in a direction that is ~45° to the tubule axis.

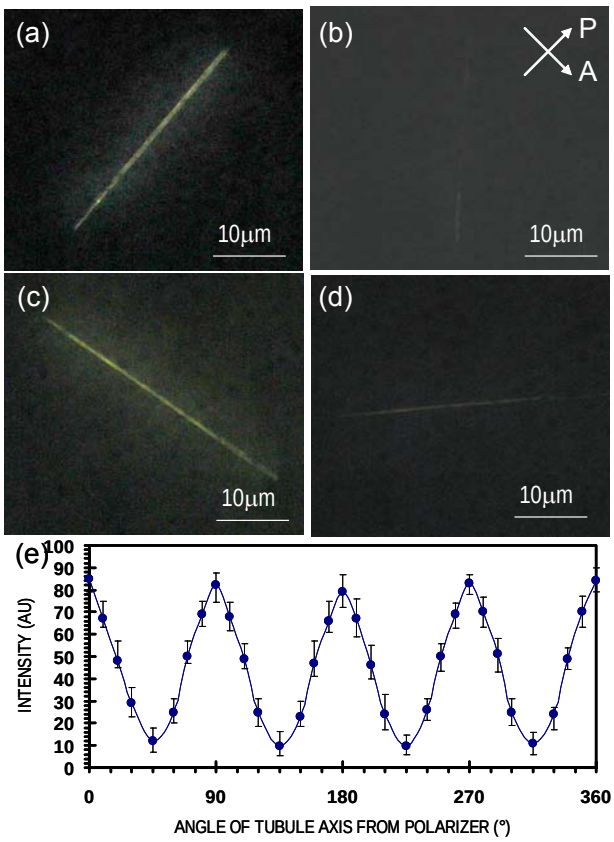


**Figure 9 (a-d) Polarizing microscope images of a lipid tubule below Nematic 5CB. Arrows indicate the directions of polarizer and analyzer. (e) Plots of the intensity of the transmitted light as function of the angle between tubule and analyzer.**

Not all lipid tubules below the 5CB show uniform brightness when they are viewed with a polarizing microscope. For example, we found that a featureless tubule in the unpolarizing optical microscopy (Figure 10a) shows birefringence helical stripes in the polarizing optical microscopy (Figure 10b). These birefringence stripes are a result of the orientation changes of the liquid-crystal 5CB on the tubule surface. They are lost when the 5CB is heated into the isotropic phase but reappear when the 5CB is cooled down to the nematic phase, which is clear evidence that the birefringence helical stripes in the liquid-crystal image are induced by the tubule. We measured the intensity of the

transmitted light across the width of the birefringence helical stripes with and found that the intensity has a minimum at both edges of the stripes and reaches a maximum in the middle of the stripes (Figure. 10c). The changes of the transmitted intensity reflect the variations of the tilt azimuth direction of the 5CB across the width of the birefringence stripes. We conclude that the observed birefringence helical stripes reflect the modulated tilt state of the lipid tubules. Based on statistic analysis of the liquid-crystal images of tubules, we found that ~10% of lipid tubules show the modulated tile state.

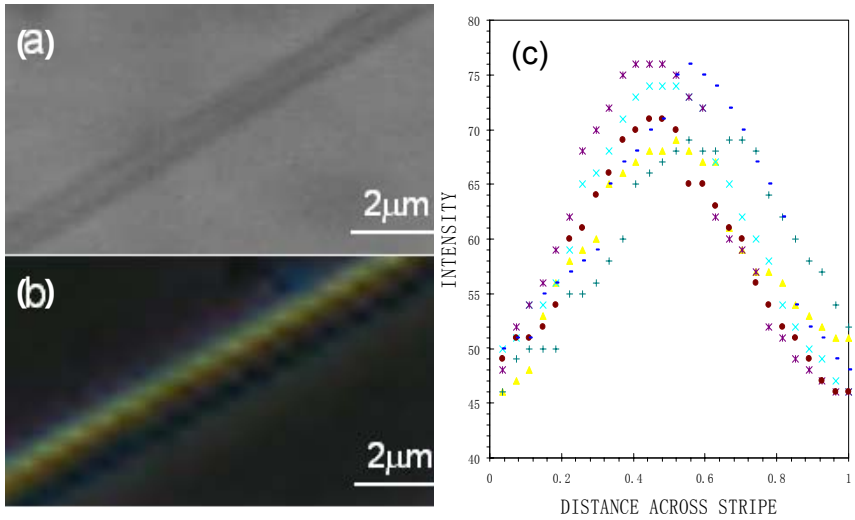


**Figure 10 Nonpolarizing (a) and polarizing (b) microscope images of a lipid tubule below the nematic liquid-crystal 5CB. (c) Plots of the intensity of the transmitted light as a function of the fractional distance across the width of the helical stripes.**

## 2.4 Conclusion

In this chapter, 1,2-bis(tricosa-10,12-dinoyl)-sn-glycero-3-phosphocholine ($DC_{8,9}PC$), a type of chiral amphiphilic molecules, was used to form tubular structures with controlled outer diameters and varied lengths and bilayer wall thicknesses. The structures of $DC_{8,9}PC$ lipid tubules were characterized by transmission electron microscope (TEM), atomic force microscope (AFM), and optical microscope. TEM images confirmed that lipid tubules were hollow cylinders with open ends, indicating their high surface-area to volume ratio. The external diameters of $DC_{8,9}PC$ tubules were 0.5μm with little variation, but their length varied from 5μm to 100μm, and their wall thickness varied from a single bilayer to a stack of 14 lipid bilayers. The self-assembly mechanism of $DC_{8,9}PC$ lipid molecules was examined by imaging molecular ordering in lipid tubules with liquid crystals as an optical amplification probe. I demonstrated for the first time that both uniform and modulated molecular tilt orderings existed in the tubule walls, which had been predicted by current theories.

# CHAPTER 3
# MECHANICAL PROPERTIES OF LIPID TUBULES

## 3.1 Introduction

The technological applications of $DC_{8,9}PC$ lipid tubules in inorganic tube synthesis[83,84] and drug delivery[85,86] rely on two essential properties. First, they have hollow cylindrical shapes with crystalline bilayer walls (Studied in Chapter 2). Second, they are relatively rigid structures. The rigidity of lipid tubules often apprehends from their straight shapes in optical and electron microscopy observations. However, the elastic and plastic deformations of lipid tubules have not been characterized explicitly. In this chapter, we will study the mechanical properties of $DC_{8,9}PC$ lipid tubules in terms of bending rigidity, persistence length, elastic modulus, and critical force for collapse.

From the technical point of view, the most fascinating features of lipid tubules are their open ended hollow structures. Both outer and inner surfaces could be used as templates to fabricate advanced materials. For these applications, we expect lipid tubules to be rigid enough to stand the radial deformation caused by depositing inorganic particles or loading agents. On the other hand, we hope lipid tubules to be flexible along the long axial direction, so we may bend them into desired shapes. To probe mechanical properties of $DC_{8,9}PC$ lipid tubules in axial and radial directions, shrinking liquid droplets method and nanoindentation technique were developed in this chapter.

### 3.1.1 Solid-Liquid-Air Triple Contact Line

It is known that the solid-liquid-air triple contact line is associated with a number of surface processes including wetting, dewetting, coating, painting, and lubrication[87]. Recently, the moving contact line of liquid droplets during wetting and dewetting on surfaces has been used in nanofluidic technology and nanofabrication. For example, the contact line of a receding meniscus has been used to stretch and align chain molecules such as DNA molecules[88], peptide tapes[89], lipid tubules[90], and tobacco mosaic virus[91]. Such a technique, referred as "molecular combing", is based on the surface tension of the liquid-air interface that pulls the molecules along the moving direction of the contact line. As a result, the molecules are aligned along the direction of motion of the meniscus. The contact line of a receding meniscus has also been used to bend DNA molecules, which are grafted at both ends on a vinyl-terminated silane monolayer into a looplike shape[92]. In this chapter, we study the axial deformation of $DC_{8,9}PC$ lipid tubules trapped inside shrinking liquid droplets on glass substrates.

### 3.1.2 Atomic Force Microscope

Atomic force microscope (AFM) has proved its value for probing micromechanical properties of soft materials by collecting force curves over a point on the materials surfaces. A force curve is a plot of the AFM cantilever defection as a function of the cantilever probe-sample separation. Through the analysis of the force curve with appropriate theoretic models, quantitative information can be obtained regarding the elastic properties of the soft materials. Recently, the AFM force curves have been extensively used to examine mechanical properties of soft materials, including

lysozyme[93], platelets[94], bacteriaphages[95], biological cells[96,97], lipid vesicles[98], polymer gels [99], polyelectrolyte capsules [100], human metaphase chromosomes [101], dendritic molecules[102], and phage capsid[103].

## 3.2 Axial Bending

### 3.2.1 Experimental Methods

A drop of dilute tubule solution was applied on a glass substrate and then allowed to dry in air at room temperature. We note that the drop first wets the glass surface to form a thin liquid film. Dewetting from the glass surface causes holes to open up in the thin liquid film, leading to the formation of a number of small droplets. 1-Dodecanethiol (DDT) (Aldrich) was dissolved in ethanol. Self-assembled monolayers (SAMs) were prepared on Au-coated mica substrates with the (111) surface (Molecular Imaging Inc.) through adsorption from 1mM DDT ethanol solution. A drop of the tubule solution was dried on the hydrophobic DDT SAMs in air at room temperature.

### 3.2.2 Results and Discussion

#### 3.2.2.1 Axial Bending Mechanism

Figure 11 shows optical microscopy images of lipid tubules trapped in a shrinking lipid droplet. As the solvent continuously evaporates the radius of the droplet base decreases. The long lipid tubule which is circled in Figure 11a remains straight until

it encounters the shrinking contact line. In this case, the gas-liquid interface applies a compressive load on the ends of the lipid tubule and causes it to buckle (Figure 11b). As the stain energy builds up in the buckled tubule, it pokes through the interface (Figure 11c) and adheres on the glass substrate, instead of snapping back to form a straight shape (Figure 11d). As can be seen, the short lipid tubule, which is circled in Figure 11c, directly pokes the interface without buckling. The competition between the elasticity of the lipid tubules and the compressive force determines whether the lipid tubules remain straight or not.

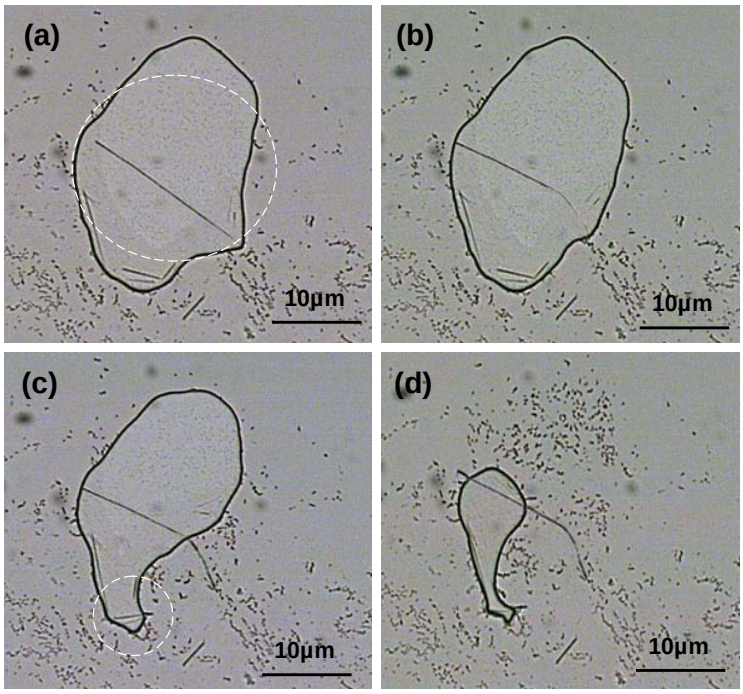


**Figure 11 Optical microscopy images of the deformation of lipid tubules trapped in a shrinking liquid droplet on a glass substrate. The liquid droplet was dried in air at ~ 23°. The radius of the droplet base decreases with the solvent evaporation. The long lipid tubule circled in (a) remains straight until it encounters the shrinking contact line. The Laplace pressure associated with the interface causes the lipid tubule to buckle (b). As the strain builds up in the bent tubule, it pokes through the interface (c) and adheres on the glass substrate (d). The short lipid tubule circled in (c) directly pokes the interface without buckling.**

3.2.2.2 Bending Rigidity and Elastic Modulus

The buckling of the lipid tubules trapped in a liquid droplet allows their bending rigidity to be estimated. The critical force for tubule buckling can be written as follows[104]

$$F_{crit} = \frac{EI\pi^2}{l^2} \quad (1)$$

where $l$ is the length of unbent tubules and $YI$, the bending rigidity, is the product of elastic modulus ($E$) and the area moment ($I$) of inertia. For a lipid tubule trapped in a liquid droplet, the compression force that the liquid interface exerts on the tubule ends is related to the interface tension[105,106]:

$$F_{comp} = 2\pi r_e \gamma \cos\theta \quad (2)$$

where $r_e$ is the external radius of the lipid tubule, $\gamma$ is the tension of the interface, and $\theta$ is the contact angle at the interface (Figure 12). If $F_{comp} > F_{crit}$, the lipid tubule buckles, otherwise, it remains straight. The balancing of the two forces yields a critical length ($l_c$). Below $l_c$, the lipid tubule remains straight, and above $l_c$, it buckles. The bending rigidity is given by:

$$EI = \frac{2r_e\gamma_c^2 \cos\theta}{\pi} \quad (3)$$

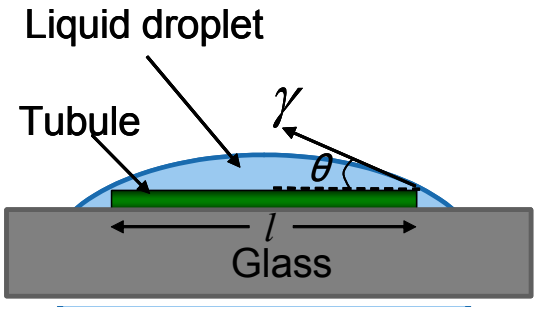


**Figure 12 Schematic of a lipid tubule with both ends trapped a liquid droplet on a substrate. Where $\gamma$ is the interface tension of liquid droplet, and $\theta$ is the contact angle of water with the hydrophilic tubule. The force ($F_{comp}$), which is applied on the tubule end, is related to the interface tension: $F_{comp} = 2\pi r_e \gamma \cos\theta$, where $r_e$ is the external radius of the lipid tubule.**

For a water droplet on a hydrophilic glass surface, interface tension ($\gamma$) is ~ 72 mN/mc. at room temperature. The lipid tubules terminated by the phosphochloline groups are hydrophilic. The contact angle ($\theta$) of water with the hydrophilic lipid tubules is expected to be very low. Given the small diameter of lipid tubules, it is difficult to measure the water contact angle on the lipid tubules. It is reasonable to assume $\cos\theta \sim 1$.

Figure 13a shows an optical microscopy image of the lipid tubules with different lengths on a glass substrate. As can be seen, longer tubules are semi-flexible and bent into loop-like shapes, while shorter tubules are stiff and remain straight. On the basis of the observation of tubules bent on glass substrates, we found that the critical length ($l_c$) was 15 ± 0.2 μm. Figure 13b is a transmission electron microscopy image of a typical $DC_{8,9}PC$ lipid tubule. The external radius ($r_e$) and internal diameters ($r_i$) of the hollow lipid tubule are found to be ~0.25 μm and 0.17 μm, respectively. The area moment ($I$) of inertia for a hollow lipid tubule can be written as:

$$I = \frac{\pi(r_e^4 - r_i^4)}{4} \tag{4}$$

Given these parameters, we estimate the bending rigidity ($IY$) of the $DC_{8,9}PC$ lipid tubule to be $\sim 2.6\times10^{-18}\,\mathrm{Nm}^2$ and the elastic modulus ($E$) to be ~ 1.074 GPa.

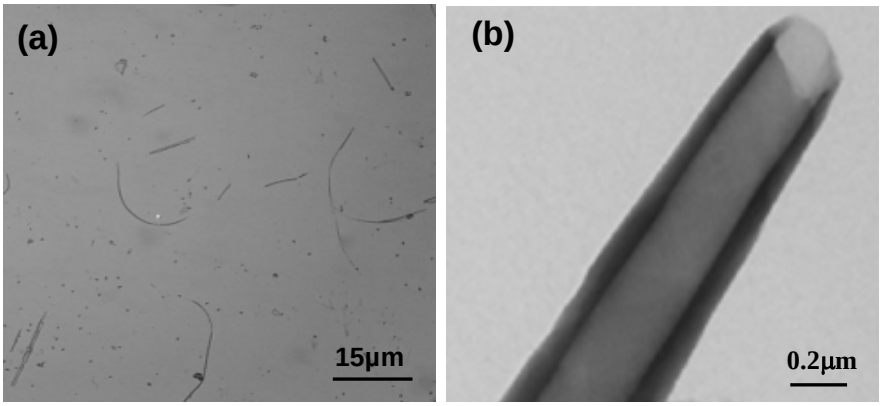


**Figure 13 (a) Optical microscopy image of lipid tubules with different lengths on a glass substrate. Dilute tubule solution was applied on the glass substrate. This image was taken after the tubule solution was completely dried in air at ~ 23°. The critical length of unbent tubules was estimated to be15 ± 0.2 μm from a number of optical images. (b) TEM image of a straight lipid tubule dried on carbon coated grids. The TEM image was taken at room temperature.**

To understand how meaningful the estimated modulus for the $DC_{8,9}PC$ tubules, we compared it with those of other self-assembled supramolecular structures. Shimizu and coworkers[107] used an optical tweezer to bend a lipid nanotube on a glass slide. The nanotube has a diameter of 50 nm and a wall thickness of 40 nm. By ignoring the interaction between the lipid nanotube and the glass surface, they estimated the Young's modulus of the lipid nanotube to be ~ 720 MPa. Compared with the lipid nanotubes, the $DC_{8,9}PC$ lipid tubules are slightly stiff, and they are much stiffer than self-assembled lipid vesicles with the Young's modules in the range of 0.2 to 1.3 MPa[108]. The Young's modulus of tubelin microtubules, which were measured by observing their thermal fluctuations, was ~1 GPa.30 Recently, de Pablo et al.[109] used atomic force microscope indentation to measure the local mechanical properties of tubelin microtubules and found that their Young's modulus is ~800 MPa based on a finite element calculation.

We note that Elbaum et al.[110] carried out a similar approach in measuring the mechanical properties of tubelin microtubules. They studied the deformation of tubelin microtubules in a lipid vesicle with micropipette aspiration. The tubelin microtubule

buckled as aspiration increased the tension in the membrane of the lipid vesicle. The *IE* of the tubelin microtubules was estimated to be $8.6\times10^{-23}\,\mathrm{Nm}^2$. In their approach, tubulin polymerized inside of the lipid vesicles forming a microtubule. But not all self-assembled supramolecular tubes and fibers can be easily synthesized in lipid vesicles. From this point of view, our approach is more simple and practical in studying mechanical properties of preformed soft tubes and fibers.

3.2.2.3 Strain Energy

The strain energy ($U$) of a rod confined in a liquid droplet can be written as follows[111]:

$$U = \frac{EI\pi^2}{3l}\left(1-\frac{d}{l}\right)\left(3+\sqrt{1-\frac{d}{l}}\right) \tag{5}$$

where $l$ the contour length of the rod and the $d$ is the diameter of the droplet. For the bent lipid tubule trapped inside a shrinking liquid droplet with the $d/l$ ratio of 0.86 (Figure 11b), the elastic energy of the bent lipid tubule is calculated to be $1.67\times10^{-11}\,\mathrm{Nm}$. The elastic energy continuously increases as the $d/l$ ratio decreases. If the train energy of the buckled lipid tubule is larger than the interface energy, it pokes through the interface (Figure 11c). As can be seen in Figure 13a, there are no cracks and breaks observed for the bent lipid tubules on glass substrates.

3.2.2.4 Persistence Length and Relative Flexibility

Persistence length, a parameter related to the stiffness of lipid tubules, is calculated with the techniques by Frontali et al[112], who used them to quantify the persistence length of DNA from scanning electron microscopy images of two-

dimensional (2-D) DNA conformation. The persistence length can be calculated based on the following assumptions: 1) The tubule consists of n rotating vectors of length *l* joined in succession, where each vector is oriented at an angle θ with respect to the previous vector (Figure 14a). The probability density $P(\theta(l))$ of the angle $\theta(l)$ between consecutive vectors is Gaussian and can be represented by

$$p(\theta(l)) = \sqrt{\frac{L_p}{2\pi l}} \exp(-\frac{L_p \theta(l)^2}{2l}) \tag{6}$$

where $L_p$ is the persistence of the tubule. 2) The observed 2D conformation is obtained by permitted deformation and is not a projection of the 3D structure. 3) The SAM surface does not change the local stiffness of the tubule. The odd moments of the distribution are all zero, whereas, the even moments are:

$$\left\langle \theta^2(l) \right\rangle = \frac{l}{L_p} \tag{7}$$

and

$$\frac{\left\langle \theta^4(l) \right\rangle}{\left\langle \theta^2(l) \right\rangle^2} = 3 \tag{8}$$

where equation (7) is used to calculate the persistence length $L_p$, while equation (8) is used to check whether the first assumption is valid. Figure 14b is a plot of $<\theta^2(l)>$ as a function of *l*. The intercept of the fit line is zero. The persistence length $L_p$ of the lipid tubule is calculated from the reciprocal slop of the plot to be 41 μm, which is much larger than that of DNA double helix (~ 50 nm) measured from AFM images of 2-D DNA conformation[113]. This suggests that the lipid tubules are much stiffer than DNA. To check whether the distribution is Gaussian, we plot the $\frac{\left\langle \theta^4(l) \right\rangle}{\left\langle \theta^2(l) \right\rangle^2}$ as a function of *l* (Figure 14d).

As can be seen, there are some deviations at large $l$, but for small $l$, the $\frac{\langle \theta^4(l) \rangle}{\langle \theta^2(l) \rangle^2}$ approaches to 3. The deviation from Gaussian in the analysis of the AFM images of 2-D conformations of DNA[113] and xanthan[114] was also observed.

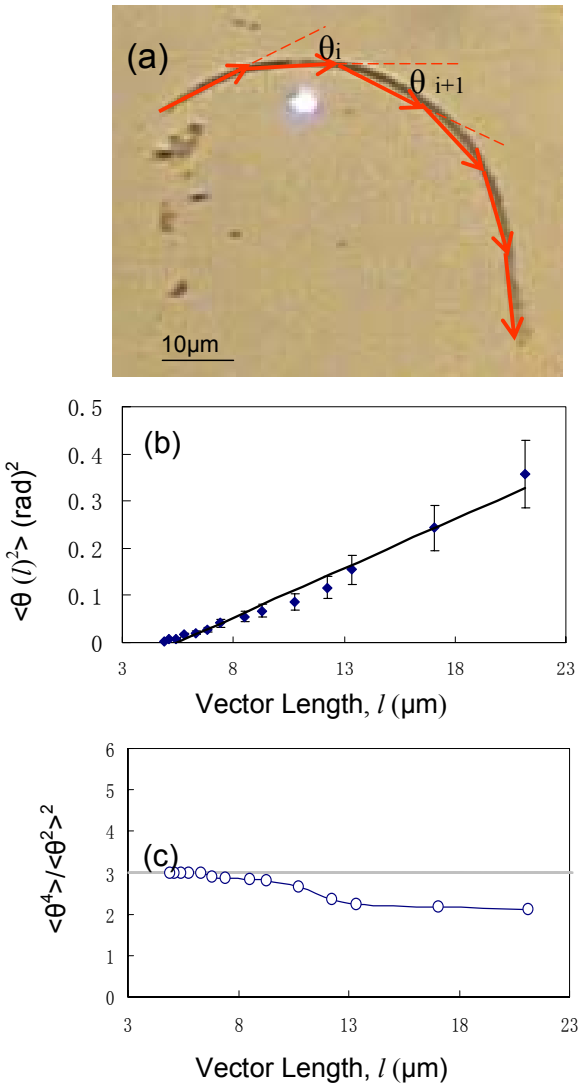


**Figure 14 (a) Optical microscopy image of a tubule loop with the projection of a vector (*l*). (b) A plot of the second moment as a function of vector length (*l*). The persistence length is determined from the inverse of the slop of the plot. (c) A plot of the fourth moment as a function of vector length (*l*) to check probability density $P(\theta(l))$ is Gaussian distribution.**

To reflect the flexibility of lipid tubules, we use the persistence length divided by tubule length. Obviously, for lipid tubules with 200 micron length, the relative value is

0.2 and it's pretty flexible, while for tubules with 200 micron length, the relative value is 8 and the tubule is very stiff. To compare with other rod structures, this is 7 orders of magnitude larger than DNA molecule, 1 order of magnitude smaller than Tobacco Mosaic Virus. Therefore our tubules have moderated flexibility.

3.2.2.5 Substrate Effect

The $DC_{8,9}PC$ lipid tubules, which are terminated by the phosphochloline groups, are hydrophilic. Lipid tubules could also be bent into loop-like shapes on hydrophobic DDT monolayers by shrinking liquid droplets. By digitizing the trace of these bent lipid tubules from optical microscopy images into pixels to give the spatial coordinates of each position along these bent tubules with MATLAB software, we measured the contour lengths ($L_c$) and end-to-end distances ($D_e$) of these bent lipid tubules on hydrophilic glass surfaces and hydrophobic DDT monolayers. Their distribution histograms are shown in Figure 15a and 15b, respectively. It is clear from these histograms that there is almost no difference in the extension of these bent tubules on the glass surface and the DDT monolayer. The average extension, defined as $\left(\frac{L_c - D_e}{L_c}\right)$, is ~ 14 % on both substrates. This suggests that the interaction of the lipid tubules with the substrates inside liquid droplets is not strong enough to affect their buckling. So we can ignore the substrate effect in calculating the bending rigidity (*IE*) and Young's modulus (*E*) of lipid tubules.

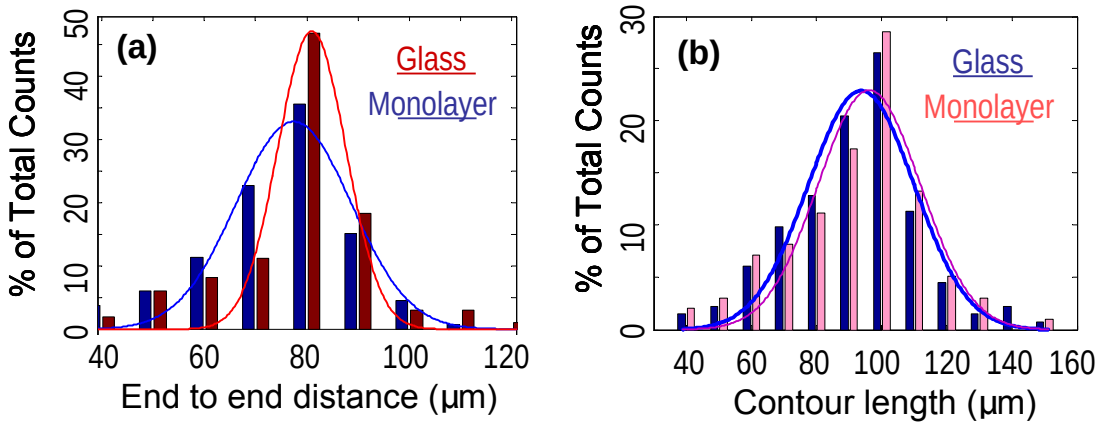


**Figure 15 Histograms of the end-to-end distances (a) and the contour lengths (b) of bent lipid tubules on hydrophilic glass substrates and hydrophobic DDT monolayers with Gaussian distributions. The contour length and end-to-end distance were measured by digitizing the trace of these bent lipid tubules from optical microscopy images into pixels to give the spatial coordinates of each position along the tubules with MATLAB software.**

## 3.3 Radial Compression

### 3.3.1 Experimental Methods

Atomic force microscope (AFM) (Dimension 3100, Digital Instruments) with software version 6.12r1 was used to study the structures and mechanical properties of the lipid tubules. The essential components of an AFM include (Fig.16): a tip mounted on a soft cantilever; a position sensitive photodetector to sense the cantilever’s deflection by tracing the laser from the laser diode and reflected by the cantilever and mirror; a feedback loop collect the information from the photodetector and control an actuator driver to move the probe by applying a high voltage; a display system collects the deflection value from the feedback loop and converts them into an image or a force-distance curve. In scanning mode, the tip will scan in xy direction; the actuator driver will apply a high voltage on the piezo and to move the probe in z-direction such that a

constant force is maintained between the tip and the sample. In force mode, the tip will move in z-direction only.

The advantage of using AFM as nanoindentor is it can apply very tiny amount of force, like in Pico Newton and sense very small displacement, like in astron, both in the z loading direction, and in the xy directions to locate the loading position. We can also control the loading rate, loading force, change the indentation environment to be air or liquid, and change the tip size and shape.

There are two different types of probe we used. One is a sharp tip; and the other is a modified tip, attached a silica particle with the diameter comparable to that of the lipid tubules. With the sharp tip, we can probe the local mechanical property of lipid tubules, while the large one allows us to study the global mechanical property of lipid tubules.

Silicon nitride cantilevers (Nanosensors) were employed and have a spring constant of 0.051 N/m, which is measured by the thermal fluctuations in air. The size of the cantilever tips (radius of curvature) is about 20 nm according to the manufacturer. AFM images were obtained in contact mode at a scanning rate of 0.5Hz in solution. To measure the mechanical properties of the lipid tubules, an indentation experiment was performed with the AFM employed in force mode. $SiO_2$ particles with 600 nm diameter were attached to tipless cantilevers with the similar spring constant of 0.053 N/m (Novascan). The modified probe was positioned exactly on top of a single lipid tubule, which was located by performing line scans at right angles to the tubule just before indentation. To better position the probe in the middle of the lipid tubule, the long axial of AFM cantilever is parallel to that of the lipid tubule, and the X Rotate parameter was

set to be 22 degree to prevent the probe from plowing surface laterally during indentation. Force-distance curves were recorded by measuring the deflection (force) of the AFM cantilever as it approaches the samples. For each measurement, approximately 100 force-distance curves were performed at a loading rate of 2.54μm/s. To avoid lipid tubules' damage during an experiment, the deflection of the cantilever was maintained within the range of 1~1.25V, which corresponds to a maximal loading force of approximately 9nN. All AFM experiments were performed in ethanol/water solution at 20-23℃.

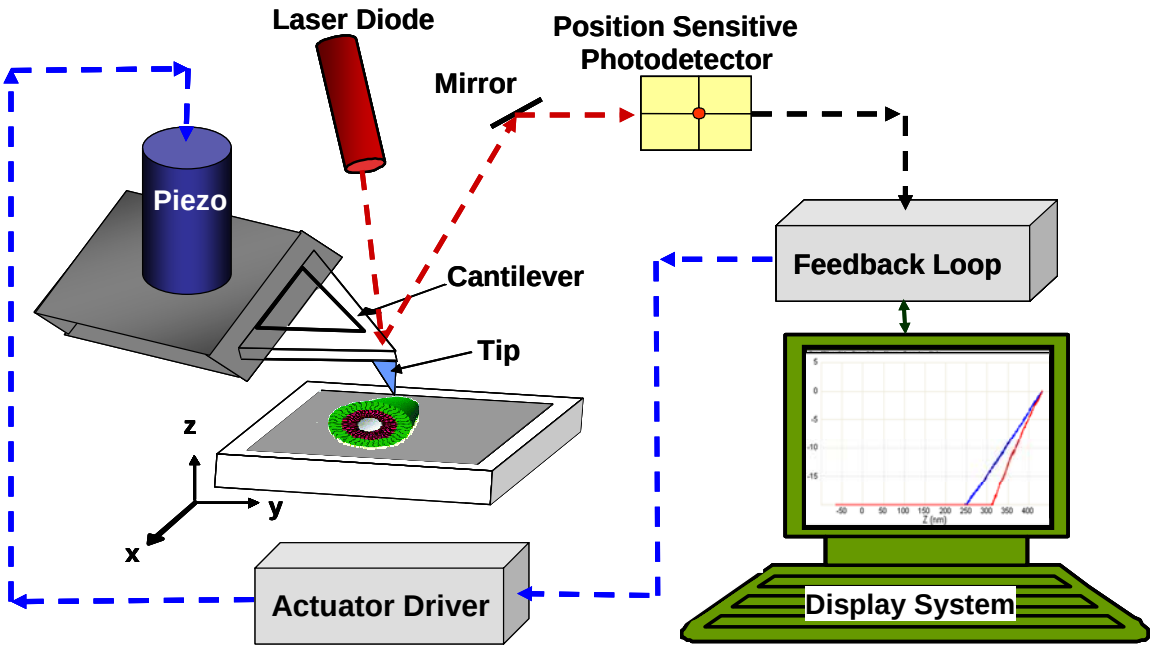


**Figure 16 Instrumental set up of Nanoindentation by AFM. The essential components include: a tip mounted on a soft cantilever; a position sensitive photodetector to sense the cantilever's deflection by tracing the laser from the laser diode and reflected by the cantilever and mirror; a feedback loop collect the information from the photodetector and control an actuator driver to move the probe by applying a high voltage; a display system collects the deflection value from the feedback loop and converts them into an image or a force-distance curve.**

### 3.3.2 Results and Discussion

#### 3.3.2.1 Small Deformation—Elastic Properties

##### 3.3.2.1.1 Stiffness

A typical force-distance curve for a lipid tubule is plotted in Figure 17a, together with the corresponding cantilever deflection curve on a glass substrate, which can be considered as an infinitely stiff material compared to the cantilever, and one that can not deform. The difference between the z-distance of the lipid tubule and the cantilever deflection on the glass substrate for a given loading force corresponds to the indentation depth of the lipid tubule by the AFM probe. As seen in Figure 17a, the loading force and z piezo distance on lipid tubules has a linear relationship. The linear relationship indicates firstly that the lipid tubules in water are hollow structures, because for a solid object the expected force-distance relationship is non-linear and follows Hertz 3/2 power law. The linear relationship secondly confirms that the radial deformation of lipid tubules is within the elastic region. It has been proved that the lipid tubules may maintain their elastic behavior when the radial deformation was up to ~20%[115]. In each of our indentation experiments, we applied repeated force up to 9nN at a loading rate of 2.54μm/s for about 100 times. At the maximal applied loading force, the indentation depth was about 75nm, about 15% of the original tubule diameter. Maintaining small indentation depths is important for minimizing damage to lipid tubules and ensures that the rigid supporting substrate will not contribute to the measured stiffness[116] during the experiment. The individual measured effective spring constant values obtained during a single experiment were plotted against the experiment number/count (Figure17b). The small standard deviations (5%) of the effective spring constants demonstrate that the lipid tubule did not

undergo a significant irreversible deformation during the indentation measurements. For 31 lipid tubules with outer diameter of 500±10 nm, we performed at least two experiments for each of them at different spots, and plotted their distribution as a histogram (Figure 17c). The Gaussian fit (performed on the cumulative histogram) gives an effective spring constant value of 0.0347±0.0017 N/m. The narrow distribution of spring constants from different $DC_{8,9}PC$ tubules indicates the elastic deformation during each measurement and the homogenous materials property for those tubules.

Considering the AFM probe and the lipid tubule as two springs in series, both the cantilever bending and the deformation of lipid tubule will result in the measured effective spring constant. From the slope of the linear sections of the FZ curves, we could, therefore, calculate a sprint constant (stiffness) of the lipid tubule ($k_{\text{tubule}}$) using the equation:

$$k_{tubule} = \frac{k_e k_{eff}}{k_e - k_{eff}} \tag{9}$$

where $k_{\text{eff}}$ is the effective (measured) spring constant and $k_{\text{c}}$ is the spring constant of the cantilever. The calculated stiffness of lipid tubules is ~0.113±0.006 N/m.

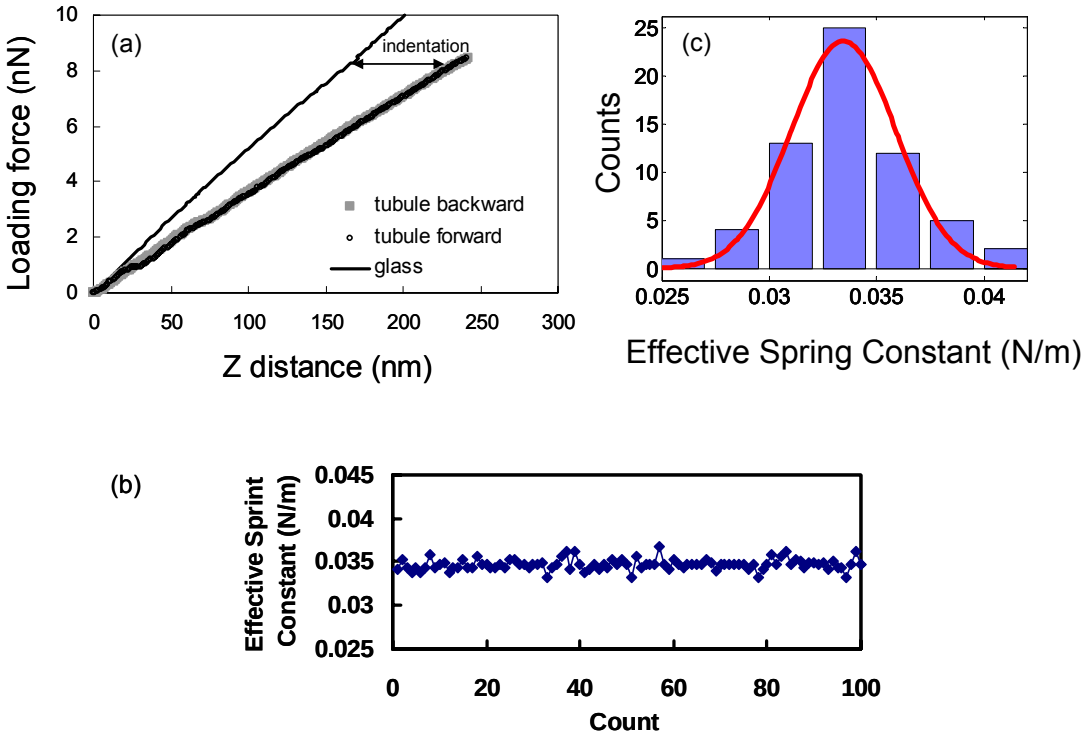


**Figure 17 Measure and calculate effective spring constants of lipid tubules. (a) Typical force-distance curves taken on a single lipid tubule (black for loading, gray for unloading) and on glass slide (only show loading curve). The abscissa measures the vertical position of the tip. The point of contact between lipid tubule and tip is set to z=0. The ordinate measures the force exerted by the tip on the sample, which is derived from the cantilever deflection using a calibration factor. (b) For one spot on one tubule, we applied repeated force for 100 times, the measured effective spring constants were plotted against the experiment number (count). (c) Histogram and Gaussian-fitted curves of effective spring constant smeasured from 31 individual lipid tubules.**

3.3.2.1.2 Young's Modulus

To get the Young's modulus from the calculated tubule stiffness, we utilized finite element analysis. In software Ideas-12, the tubule was modeled as a tube made of a homogeneous material, sitting on a flat rigid surface and loaded by a spherical rigid indenter with radius of 300 nm similar to the AFM tip used in the experiments. The thickness/radius/length ratio (t/r/l) of the modeling tubes was the same with that of lipid tubules used in experiments. To reduce computing time, considering the axial symmetry of the problem, the model was reduced to a quarter by using the two mirror symmetry

planes intersecting at the loading point (Fig.18). This quarter was then divided into 3000 - 4500 three dimensional brick elements and subjected to axisymmetrical boundary conditions. For more details, please see the finite element analysis programming codes attached in the appendix.

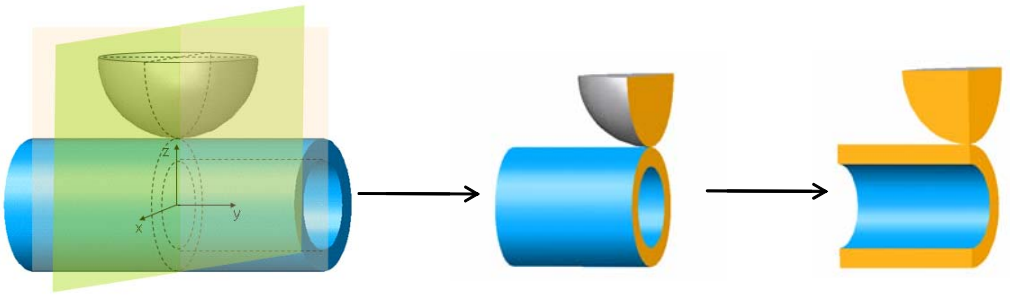


**Figure 18 The FEM model was reduced to a quarter by considering axial symmetry.**

The postprocessing was done by software ABAQUS-6.6. Loading was simulated by prescribing the downward movement of 75nm of the rigid indenter, calculated in 100 increments. This finite element simulation comprised of a linear elastic material behavior and nonlinear geometric kinematics which allow for large displacements. As the geometric nonlinearity was included in the model, the small-sliding algorithm accounted for any rotation and deformation of the indenter surface and updated the load path through which the contact forces are transmitted. A nonlinear problem was solved to find the distribution of forces in the contact area. Small sliding contact was assumed between the indenter and tubule, where a point on indenter surface contacting the tubule surface did not slide more than a typical element dimension.

The stiffness of the model was calculated as the loading force (simulation results) divided by the corresponding displacement. The Young's modulus and the wall thickness of the modeled tube were adjusted and the analysis repeated until the calculated stiffness

fitted the measured stiffness. The Young's Modulus for lipid tubules with 10 bilayers wall was quantified (Figure 19) to be ~705MPa.

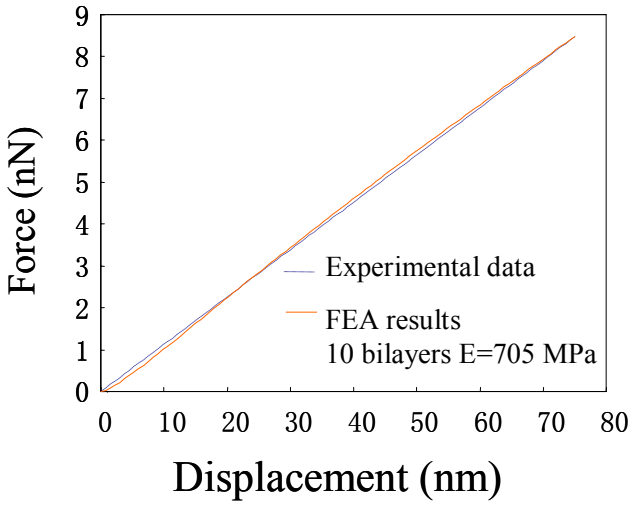


**Figure 19 Comparing experimental force-displacement curve and finite element simulation result, we got the Young's Modulus is 705 MPa for lipid tubules with 10 bilayers wall.**

3.3.2.1.3 Stress Analysis of the Modeled Tube with a Wall Thickness of 70nm

Figure 20 contains a series of images of a quarter of modeled tube under increasing loading. This modeled tube has a wall thickness of 70nm, corresponding to the thickness of 10 $DC_{8,9}PC$ bilayers. The color contours indicate the von Mises stress distributions. At the beginning (Figure 20a), compressive stress initiates at the external surface of the top tubule wall and then extends downward and laterally. No other stress appears until the loading force reaches 0.898nN and the displacement reaches 9nm. When the loading force is larger than 0.898nN (eg., Figure 20b, 1.812nN), von Mises stress also appears at the internal surface of the top tubule wall and spreads upward and laterally. Raising the loading to 3.791nN (Figure 20c), deformation of the tubule happens not only

at the top wall but also expands to the whole tubular structure, which is indicated by small stress spreading through the side and the bottom tubule wall. Increasing loading to 4.492nN (Figure 20d), the deformation of hollow structure of the tube increases further. When the loading is 6.191nN (Figure 20e), the stress on the side wall of the tube increases largely in the lateral direction. Stress concentrates in the internal surface area under indenter. Finally, the stress reaches maximum at the inner surface of the upper wall (Figure 20f).

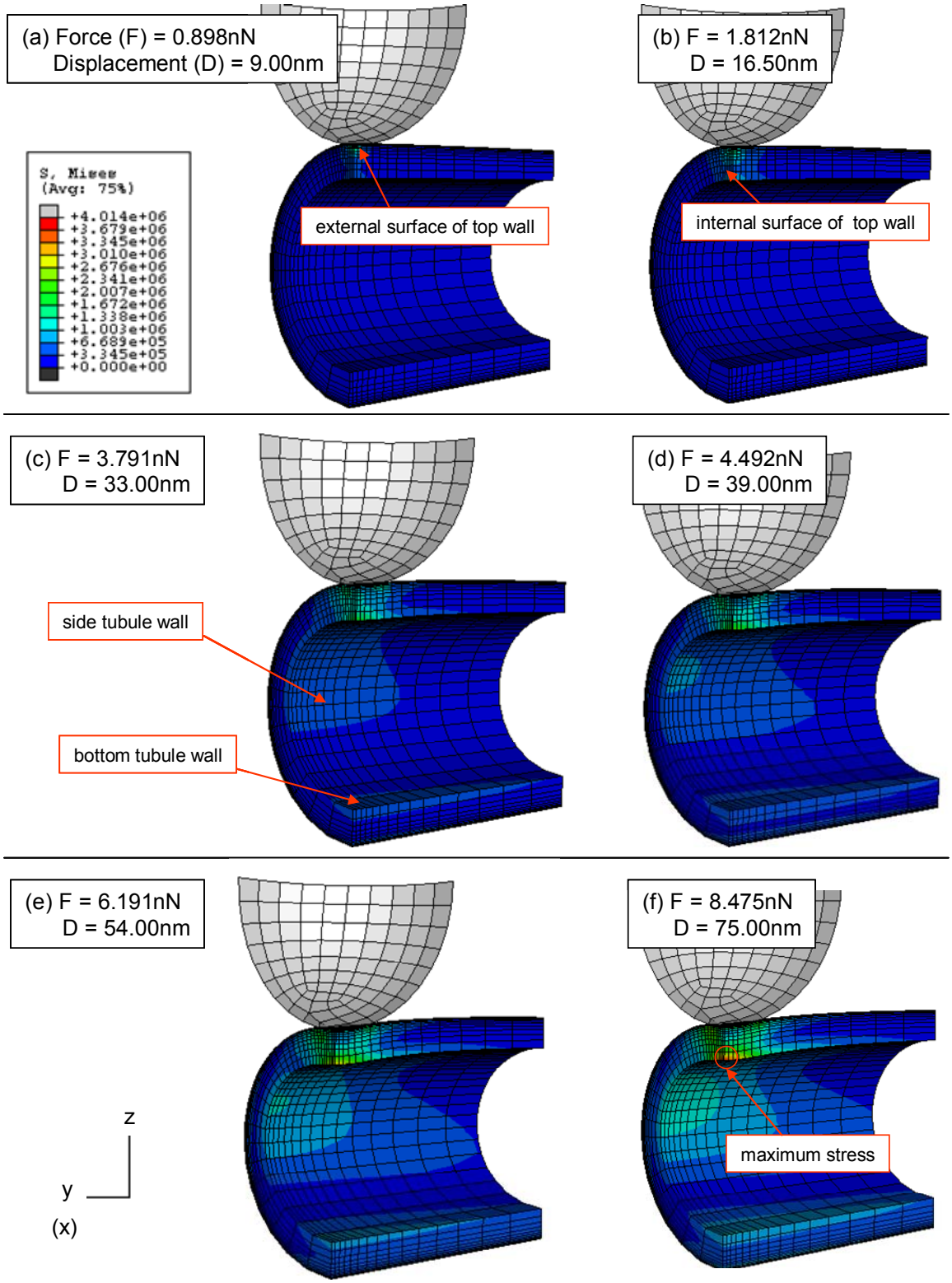


**Figure 20 Von Mises stress analysis for the modeled tubes with 70nm wall thickness under different loadings (F) and displacements (D).**

3.3.2.1.4 Shape Analysis in Thin and Thick Walled Tubes

Figure 21 shows cross section views of the initial and final states of two modeled tubes with thick walls and thin walls, respectively. These two modeled tubes have the same outer diameter of 500nm. The thickness of the thick walls (Figure 21a and b) is 70 nm, corresponding to 10 $DC_{8,9}PC$ lipid bilayers, while the thickness of the thin walls (Figure 21c and d) is 14 nm, corresponding to about 2 lipid bilayers. The simulated indentation depth is 75nm for both cases. At the same indentation depth, the thick walls still keep a convex shape (Figure 21b), while the thin walls change from a convex to a concave shape (Figure 21d).

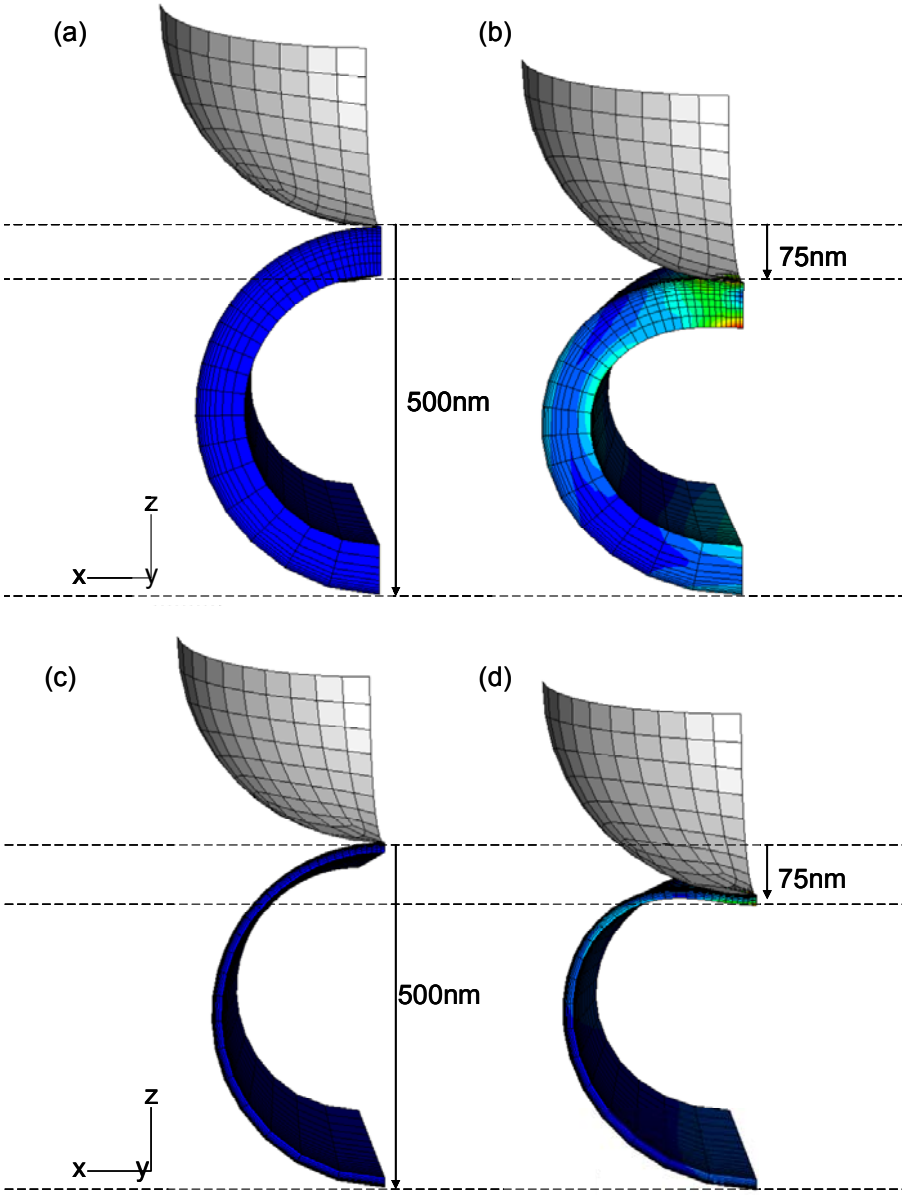


**Figure 21 Cross section views of the initial and final states of two modeled tubes with thick walls and thin walls, respectively. The outer diameter of both tubes are 500nm, wall thickness is 70 nm for thick walls (a,b), and 14 nm for thin walls (c,d). At the indentation depth of 75nm, the thick walls still keep a convex shape (b) while the thin walls change from a convex to a concave shape (d).**

3.3.2.1.5 Stress Analysis in Thin and Thick Walled Tubes

Fig. 22 is the contour plot of Von Mises stress on the modeled tubes with different wall thickness at 75nm displacement.

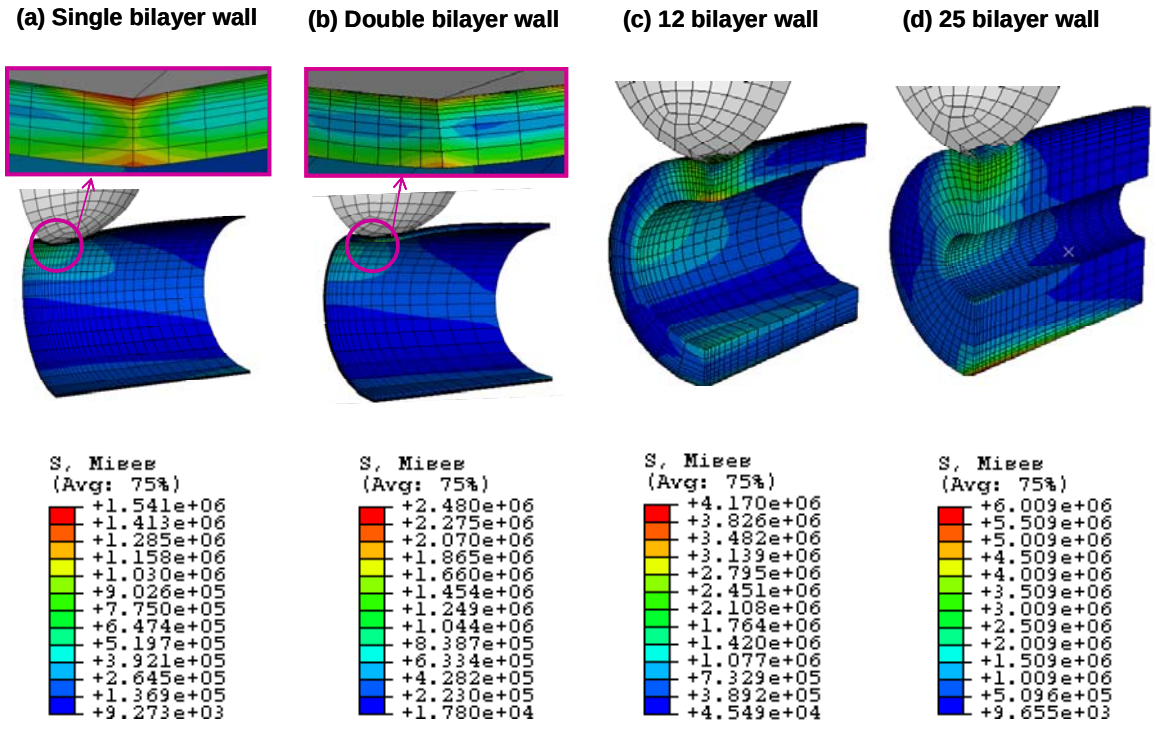


**Figure 22 The contour plot of Von Mises Stress on tubule models with different wall thickness. With increasing tubule wall thickness from 1 bilayer to 25 bilayers (a-d), the maximum stresses at the same displacement (75nm) increased from 1.541 MPa to 6.009 MPa.**

For the modeled tube with a single bilayer wall, a large portion of the tube structure deflects under the indenter. Stress persists throughout the tube wall under the indenter, and changs direction from compressive stresses in the outer surface to tensile stresses in the inner surface. The value of the maximum compressive stress is larger than that of the maximum tensile stress. Therefore, the break of the tube wall is explained to firstly occur at the contact point of the outer surface. This state of stress resembles the bending of a thin wall. As a consequence, the movement of the indenter comprises of the sum of a global deflection of the thin wall under the applied load and a local indentation into the thin wall, and the global deflection dominated.

Similar to the single bilayer wall, the shape of double bilayer walls changes from a convex to a concave at the maximum displacement of 75 nm. The difference is that at

the same maximum displacement, the maximum von Mises stress increases from 1.541 MPa for the single bilayer wall to 2.480 MPa for the double bilayer wall. At the final deformed state, the compressive stress in the top wall is larger than the tensile stress, indicating that the crack should firstly occur at the inner surface of the top wall.

In the modeled tube with 12 bilayers walls, a large portion of the tube structure deforms under the indenter. This tubular structure retains convex at the maximum displacement. At the deformed state, stresses persist throughout the tube wall and converge toward the spot far from the indenter. The break of the wall thus should happen at the inner surface. This state of stress resembles the bending and compressing of a thick wall. The movement of the indenter caused a global deflection and a local compression of the thick wall.

For the modeled tube with 25 bilayers, the compressive stresses are concentrated at the indenter-tubule contact region and the tubule-substrate contact region. The compression of tubule walls (top wall and bottom wall) plays a dominating roll in the deformation process. Compressions of the core will happen only when the indentation depth reaches ~50nm. Before this point, the state of stress resembles Hertzian contact[117]. The final stress concentrates at the out surface of the bottom wall. Here, the lipid tubule-substrate contact region was modeled by fixing the line at the bottom of the lipid tubule. So the real stress distribution at the bottom of the lipid tubule will be less than this simulation results due to the increased contact areas.

For the practical purpose, we hope that the lipid tubules are rigid in radial direction which will require a thick wall. But it will use more lipids. The lipid tubulew with thin walls are therefore preferred for economic reasons. Figure 22 and Table 2

convey the same information that the increase in tubule wall thicknesses will not cause the same amount of increase in tubule's rigidity. With the increase of the number of lipid bilayers from 1 to 25 (25 times increase), the maximum stress at the same displacement of 75nm increases only from 1.541 MPa to 6.009 MPa, even less than 4 times. Considering rigidity and economy issues, the optimum wall thickness of lipid tubules for applications should be 2 bilayers. What's more, knowing the failure/break mechanism of lipid tubules with different wall thicknesses is also helpful in developing their specific applications. For example, lipid tubules with the crack initiating at the outer surface are not good candidates for using the outer surface as template to synthesize inorganic materials. Similarly, lipid tubules with the crack initiating at the inner surfaces are not very suitable of applications in encapsulation, as it may affect the releasing rates. I summarized the comparison results from finite elements models and foresaw the suitable application catalogs for lipid tubules with different wall thicknesses based on their failure mechanisms (Table 2).

**Table 2 Comparisons of finites element models of lipid tubules with different wall thickness.**

| Bilayers # | Max. Stress | Place Where Crack Initiates | Preferred Application |
|---|---|---|---|
| 1 | 1.541 MPa | Outer surface | Encapsulation |
| 2 | 2.480 MPa | Inner surface | Template |
| 10 | 4.014 MPa | Inner surface | Template |
| 12 | 4.170 MPa | Inner surface | Template |
| 25 | 6.009 MPa | Outer surface | Encapsulation |

3.3.2.2 Large Deformation-Pushing the Limits

3.3.2.2.1 Hysteresis and Collapse

After probing elastic properties of lipid tubules in the small deformation region, a series of consecutive indentations was carried out to explore the limits of lipid tubules. When the loading force was less than 0.9nN (Figure 23a), there was a linear regime extending to indentations ranging from 15% to 20% of the lipid tubules. The FZ curves were highly reproducible, as evidenced by the overlap of the curves for repeated indentations in Figure 23a. At the loading force of 1.0nN~1.4nN, the retraction curves show a small hysteresis (Figure 23b). The resilience, which is the fraction of the indentation energy returned upon retraction, was larger than 90%. There was no detectable loss in height, and images taken immediately after indentation show no evidence of damage. With the loading force beyond a threshold value (1.5nN in this case), the continuously linear regime typically ended with a catastrophic drop in the force (Figure 23c), indicating a buckling or collapse of tubule walls. The buckling or collapse usually occurred when the indentations were larger than 25% of tubule diameters and the forces were larger than 1.5nN. The force then increased with further indentation, and an additional smaller drop was observed at 1.7nN.

Figure 23d shows FZ curves of a series of indentations and the inset schematic illustrations present the tip-sample contacts and the deformation process of lipid tubules. In the beginning part of the f-d curves, as the AFM tip (silica particle with a diameter of 600nm) approached the lipid tubule, the tip sensed no force. There was likewise no force applied on the tubule, and the tubule maintained its original state. When the tip contacted the lipid tubule, the total force exerted on the sample increased linearly. The tubule wall

which was in contact with the indenter tip was first compressed in the normal direction. With the increase of loading force, the tubule wall that was in contact with the rigid substrate was compressed, and the hollow core of the tubule began to deform. When the loading force reached the threshold value of 1.5nN, the top wall changed its shape from a convex to a concave. Finally, the hollow core was further squeezed against the supporting substrate, and the compression of the tubule wall became severely.

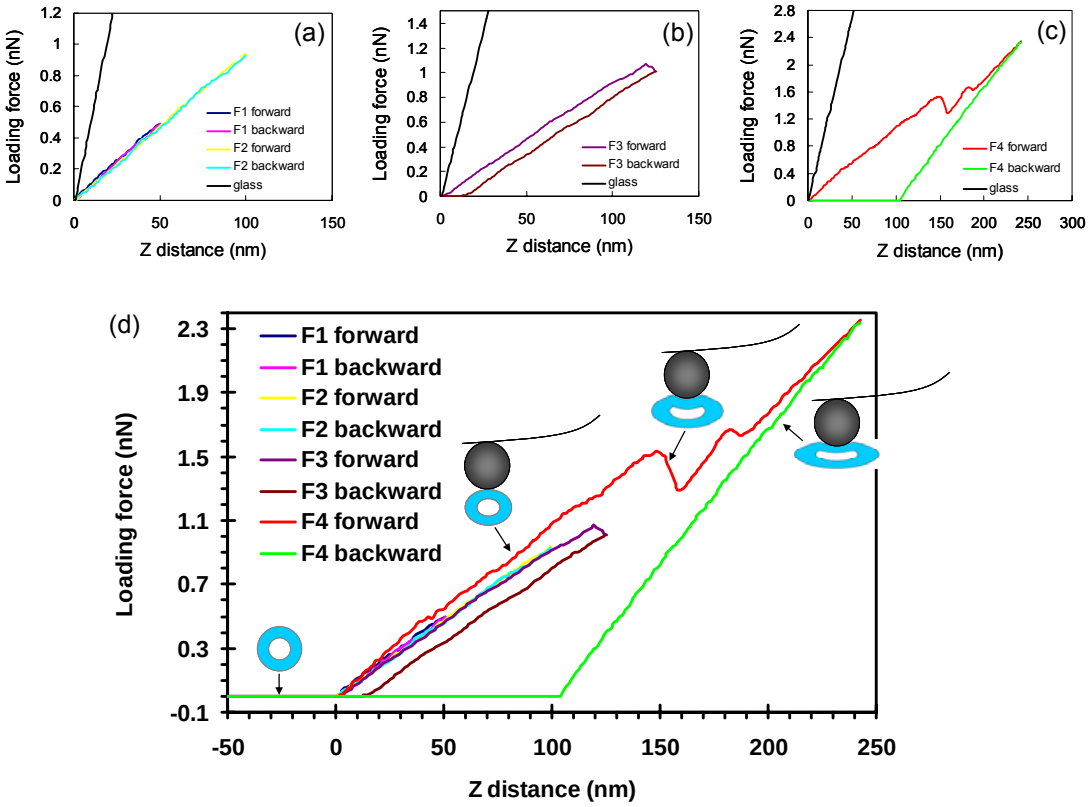


**Figure 23 FZ curves of lipid tubules on glass substrate in water. The loading force is shown as a function of the distance traveled downward by the cantilever from its initial raised position. Four successive force curves are shown. F1 and F2 show repeated small indentations, followed by a larger indentation (F3) beyond the reversible region. The purple-brown curve shows the hysteresis upon retraction. F4 shows a large indentation with a jump at the force beyond 1.5 nN, indicating a damage or collapse and the backward curve shows that the deformation is irreversible.**

3.3.2.2.2 Recovery

It was clearly observed from our studies that the collapsed tubule wall recovers in water after 6 minutes. Figure 24 is contact mode images of a lipid tubule in water with the respective cross sections. AFM silicon nitride tip with a diameter of 30nm was employed during scanning and indentation experiments. Figure 24A shows the lipid tubule before indentation. Although the apparent width of the tubule in the AFM image is broad by the geometry of the AFM tip, the cross section plot (Figure 24a) along the dash line in Figure 24A manifests that the lipid tubule has a cylindrical shape and a height of 520nm. After imaging, the tip was positioned exactly on the top of the lipid tubule in the middle area of the image, and an indentation was carried out with the same tip at a loading force of 5nN and a loading rate of 297nm/s. An AFM image was taken for the same tubule right after the indentation (Figure 24B) and the deformation of the smooth surface of the tubule can be clearly seen. The corresponding cross section plot (Figure 24b) shows the deformation of the cylindrical shape of tubule walls, and the losses in height of 100nm, about 20% of the tubule diameter. After 6 minutes, I retook the image of the same tubule by AFM contact mode scanning (Figure 24C), and found that the collapsed tubule wall recovered, with the smooth outer surface and the height of 510nm (98% of the original height) as shown in the cross section (Figure 24c). We may conclude that the relaxation time of the lipid tubule is less than 6mins. This recovery phenomenon can be explained by the diffusion of lipids.

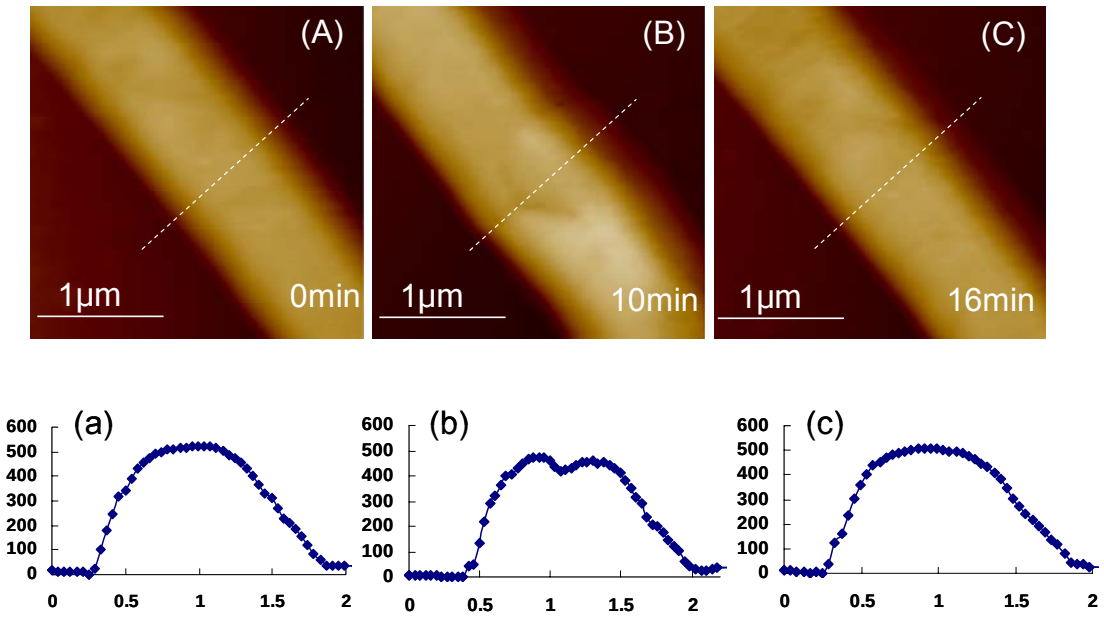


**Figure 24 (A-C) AFM image of a lipid tubule before and after indentations in water. The images taken time was indicated. (a-c) Plots of cross sections of tubule before and after indentation (a,b) and before and after recovery (b,c).**

3.3.2.2.3 Critical Force

A striking dissimilarity between small deformation and large deformation is that the FZ curve of the latter one contains a drop in the force, which manifests the buckling or collapse of tubular walls. We define the critical force as the force at which the drop begins (Figure 25).

Figure 25 shows three FZ curves obtained from the same spot of a lipid tubule in water. The inset cartoons are schematic drawings of the indentation process. There was a 6 minutes interval in between indentations. In order to precisely locate the same indentation position, the indentation rate was kept at a low value of 182nm/s. Even though the elastic deformation region did not show much variation in the slop of the curves, the critical force decreased dramatically from 4.4nN to 3.9nN and further to 3.4nN. It seems that in a period of 6 minutes, the recovery of lipid tubule was almost

completed for the small deformation and partially completed for the large deformation. The ultimate force under which the lipid tubule retained its elasticity still decreased after the recovery.

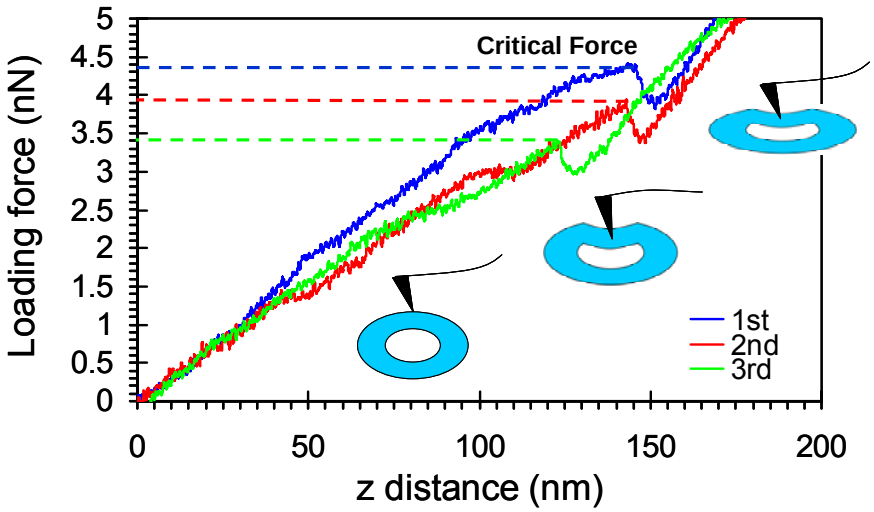


**Figure 25 Typical force-distance (FZ) curves of lipid tubules in water and illustrations of the tip-sample contacts. The FZ curves contain drops in the force, which manifests the buckling or collapse of tubular walls. We define the critical force as the force at which the drop begins. The indentation rate was 182nm/s.**

3.3.2.2.4 End Effect

It is expected from the finite element model of lipid tubule that the deformed area under a radial load will extend to both sides in axial direction for several tens of nanometers. For tubules with 10 lipid bilayer walls, when they were indented by tips with 15nm radius and maximum indentations of 27.75nm, the deformed area was simulated to be around 30nm in radius (Figure 26). As mentioned before, the modeled tubes were reduced to quarter tubes taking advantage of symmetries. There were two mirror planes of symmetry perpendicular to the supporting substrate, one parallel and another one

perpendicular to the long axis of tube. At the end of tubule, the mirror plane which was perpendicular to the long axis of tube disappeared. The break of symmetry implied that the end of lipid tubules should appear softer, which is named as the end effect[109].

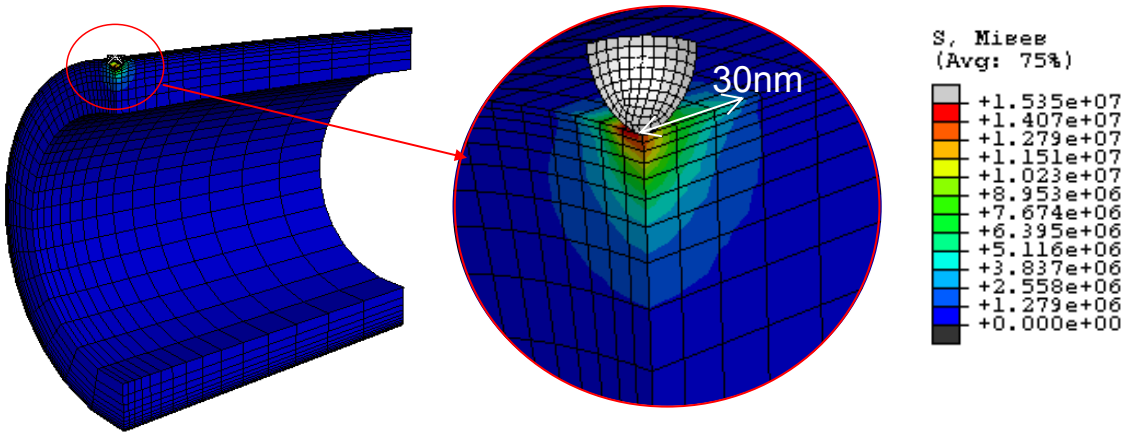


**Figure 26 The contour plot of Von Mises stress on a finite element model of the deformed tube under a radial load. The radius of the indenter is 15nm, the maximum displacement of the indenter is 27.75nm, and the deformed area extends in axial direction for about 30nm.**

To probe the end effect, a series of precisely positioned indentations was carried out close to the end of a lipid tubule. Figure 27a is a 2D contact mode AFM image showing a $DC_{8,9}PC$ tubule immobilized on glass substrate under water. Figure 27b is the corresponding 3D AFM image with three red arrows indicating three indentation positions near the tubule end. Along the dash line indicated in Figure 27a, the height of tubule was plotted in Figure 27c. It can be seen that the height of tubule decreased steeply without notable steps at the area of 500nm distance from the tubule end. This observation suggests the decrease of height is not caused by the decrease of the number of lipid bilayers but very probably due to the tip geometry effect.

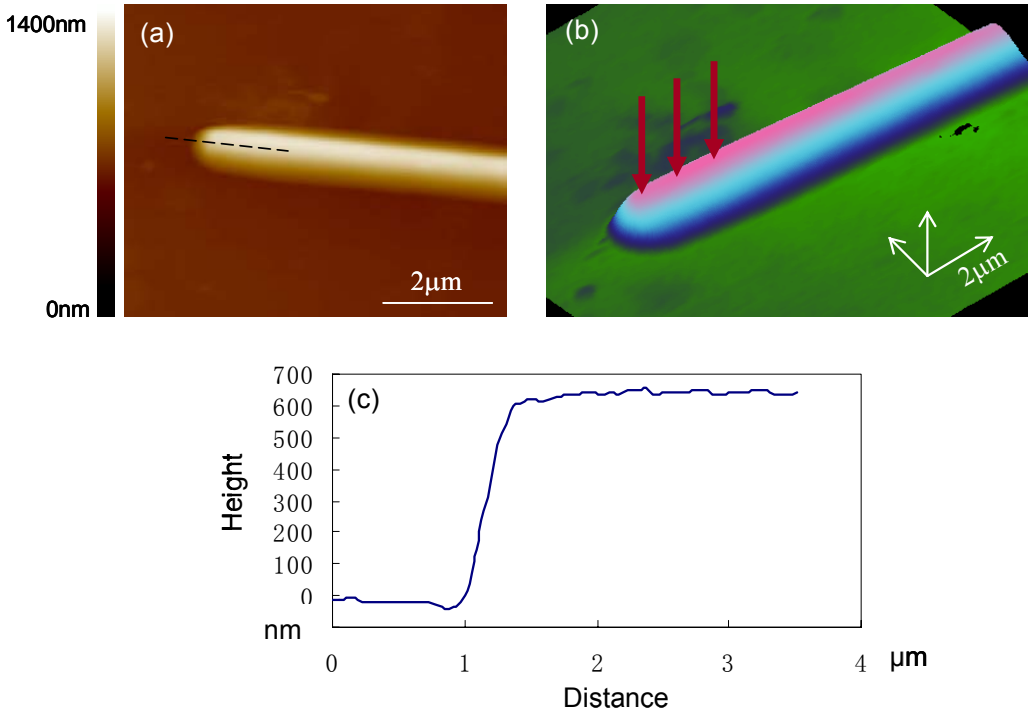


**Figure 27 AFM 2D (a) and 3D (b) image of a lipid tubule on glass substrate. The red arrow pointed the indentation direction and showed some of the indentation positions on the end of the lipid tubule. (c) Cross section plot of the tubule height along the dash line indicated in (a).**

Twenty indentations were conducted every 100nm from the end, with an interval of 10 minutes to allow the maximum recovery of tubular structure. The results were plotted in Figure 28. Spring constants were got from the slop of FZ curves, normalized to the values obtained on the same lipid tubule far from the end. Critical forces were the force at which the lipid tubule collapsed. At distances less than 1 micron from the end, the rigidity of lipid tubule seemed to be affected. For the modeled tube with 10 bilayer walls in Figure 26, the deformed area extends to both sides in axial direction for ~30nm. It is reasonable to assume the end effect caused by symmetry break up extends to ~60nm from the tubule end. In disagreement with the modeling, the end effect is still seen ~1000nm distance from the end. Therefore, the breaking of symmetry should not be the

only reason for the end effect. Generally, the rigidity and critical force of collapse should relate to the material structural perfection. The observed end effect could be explained with assumptions based on the molecular ordering in the lipid tubules. It is likely that lipid could be less ordered at the tubule end and contain more defects than the lipid in the middle part of the tubule. As indentation positions approaches the tubule end, the fraction of molecular ordering decreases, and the rigidity should decrease as it is observed. In order to avoid end effects, it is important to perform indentation experiments at least 1 micron away from the tubule ends.

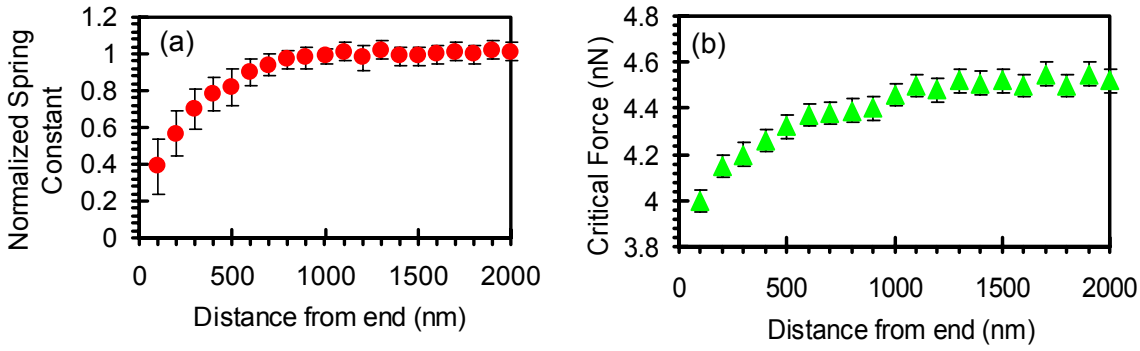


**Figure 28 End effect on normalized spring constant of the indentation force-distance curves (a) and the critical forces for lipid tubules collapse (b).**

3.3.2.2.5 Surface Stiffening

Figure 29a shows a contact mode AFM image of a $DC_{8,9}PC$ lipid tubule on a glass substrate in water. The tubule is formed by rolled-up lipid bilayer ribbons. Here, the step edges of helical bilayer ribbons forming the tubules are visible. Figure 29b is a cross section plot along the dash line indicated in Figure 29a, suggesting the cylindrical shape of the tubule. The height of the tubule along the line was 510 nm. Figure 29c is a plot along the axial direction of the tubule as shown by the arrow in Figure 29a. The

remarkable steps in heights along the tubule axis can be measured to be 16.7±1.0nm, corresponding to a stack of two lipid bilayers, because the thickness of a single $DC_{8,9}PC$ bilayer in the tubule wall has been measured to be about 6.6 nm[57]. Conducting indentations on the four spots indicated in Fig 29a, the stiffness of tubule at different wall thicknesses was calculated from the slops of the FZ curves. With finite element models, the dependence of Young's Modulus on the wall thicknesses of lipid tubules has been studied.

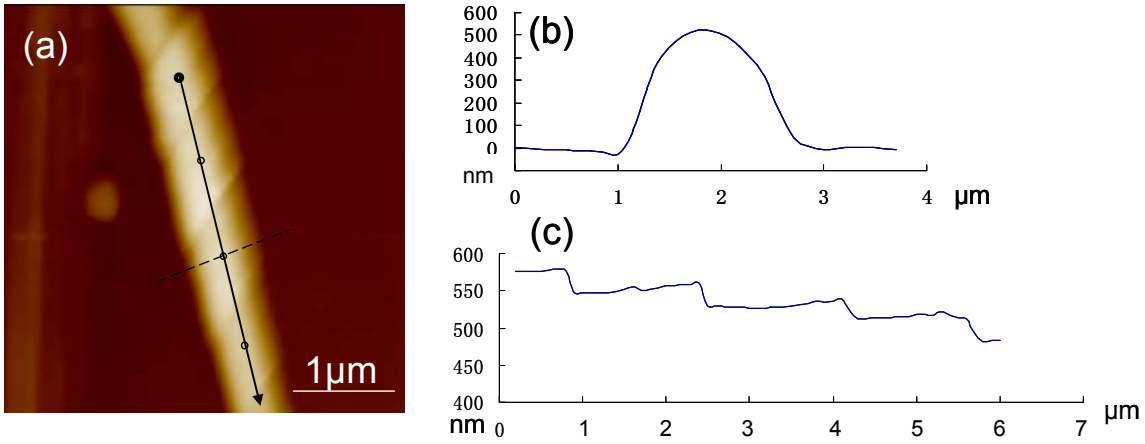


**Figure 29 (a) Contact mode AFM image of a $DC_{8,9}PC$ tubule on glass substrate in water. (b) Corresponding cross section of the dash line shown in (a). (c) Corresponding cross section of the solid arrow indicated in (a). The four dots in (a) pointed out the indentation positions.**

Due to the hollow nature of lipid tubules, the thickness of the tubule wall can not be directly measured by AFM. However, the outer diameters of the tubule could be measured from Figure 29c, and their values are 581.0nm, 551.4nm, 523.9nm, and 496.8nm. The corresponding stiffness could be calculated from their FZ curves, and their values are plotted in Figure 30a-d as the reference lines. For one outer diameter (e.g., 496.8nm), knowing its corresponding stiffness (0.058nN/nm), we built a series of finite

element models with the fixed outer diameter of 496.8nm and different wall thicknesses satisfying n×13.2nm, where n=1, 2, 3, …, integer. Figure 30a only shows simulation results of modeled tubes with wall thicknesses of 13.2nm, 26.4nm, 39.6nm, and 52.8nm, corresponding to a stack of 2, 4, 6, and 8 bilayers. By changing the Young's modulus in the material properties of each finite element models, different simulated force-indentation curves were plotted and compared with the reference line (the dash line in Figure 30a). The best fitting results for each modeled tubes are: 2 bilayers, E=5.6 GPa (the purple curve in Figure 30a); 4 bilayers, E=1.4 GPa (the blue curve); 6 bilayers, E=740 MPa (the pink curve); 8 bilayers, E=360 MPa (the green curve). Among those models, the one with 4 bilayers wall fits the reference line best, and the Young's modulus of lipid tubules with outer diameter of 496.8nm was estimated to be 1.4GPa.

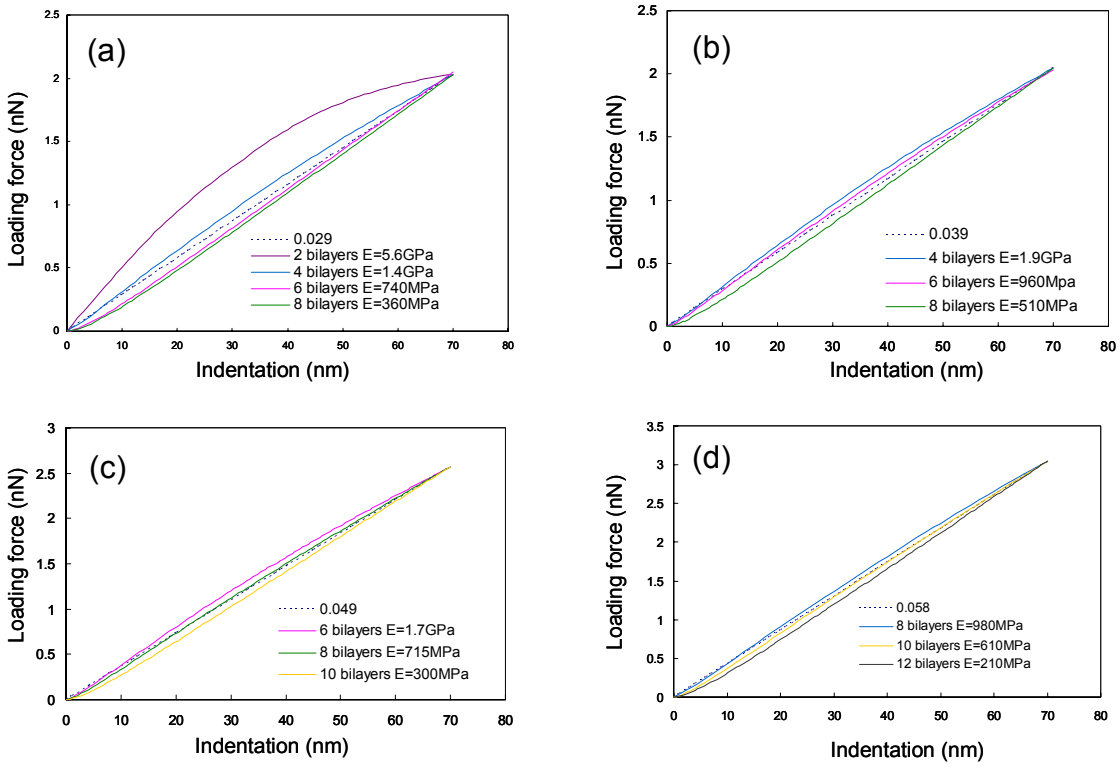


**Figure 30 Curve fittings by finite element modeling. The dash line is experimental results extracted from FZ curves at positions with four different wall thicknesses. Solid lines are force-displacement relations got from finite element models. The optimized fitting results are: (a) 4 bilayers, E=1.4 MPa; (b) 6 bilayers, E=960 MPa; (c) 8 bilayers, E=715 MPa; (d) 10 bilayers, E=610 MPa.**

Similar modeling and comparison process was employed to choose the wall thickness of the modeled tubes and estimate the corresponding Young's Modulus. For modeled tubes with outer diameter of 523.9nm, the best fitting results conveys it has a 39.6 nm thickness and a Young's modulus of 960MPa (Figure 30b). For modeled tubes with outer diameter of 551.4nm, the best fitting results come from the modeled tube with 52.8nm thickness and a 715MPa Young's modulus (Figure 30c). For the 581.0nm outer diameter, the best fitting results suggests that the corresponding tubule portion has a 66nm thickness (10 bilayers walls) and the Young's modulus of 610MPa. These results are summarized in Table 3.

**Table 3 Young's Modulus of the lipid tubule (LT) decreased with increasing outer diameters.**

| Measurement # | Outer diameter (nm) | Thickness of LT wall (nm) | Young's Modulus (MPa) |
|---|---|---|---|
| 1 | 496.8 | 26.4 | 1440 |
| 2 | 523.9 | 39.6 | 960 |
| 3 | 551.4 | 52.8 | 715 |
| 4 | 581 | 66.0 | 610 |

Inner diameters of those tubule portions with different thicknesses are calculated. For measurement # 1-4, their inner diameters are 444nm, 445nm, 446nm, and 449nm, respectively. The small variations indicate that the lipid tubule in Figure 29 has an almost constant inner diameter.

The portion of lipid tubule with 10 bilayers walls are compared with the lipid tubules with 10 bialyers walls studied in section 3.3.2.1.2. The differences between these two tubules are the outer diameter of the former one is 581nm while that of the latter one is around 500nm (with ±10nm variations). The portion of lipid tubule with a 80nm larger outer diameter has a Young's modulus 95MPa smaller.

The measured moduli of the $DC_{8,9}PC$ lipid tubule decreased dramatically with the constant inner diameter and increasing diameters. This dimensions dependant elastic mechanical behavior was also described by Miller and Shenoy [118] for Si and Al nanobeams. Zhu et al. built a core-shell composite nanowire (NW) model in terms of the surface stiffening effect correlated with significant bond length contractions, to explain the size dependence of Young's modulus in ZnO nanowires.

Lipid molecules at the surface of a lipid tubule experience a different environment[119,120] from those in the internals and thus can be treated as a modified lipid layer with a radius of $r_s$ as shown in Figure 31. We define $EI$ as the effective rigidity of the "composite" lipid tubule in Fig.31, where E is the effective Young's modulus and I is the moment of inertia of cross section of the whole tubule. Neglecting shear deformation, we obtain:

$$EI = E_0 I_0 + E_s I_s \tag{10}$$

where $I_0$ and $I_s$ are the moment of inertia of cross section of the internal lipid tubule and the modified lipid layer, respectively. Rearranging equation (9), the effective Young's modulus can be described as equation (10):

$$E = E_0 \frac{I_0}{I} + E_s \frac{I_s}{I} = E_0 (1 - \frac{I_s}{I}) + E_s \frac{I_s}{I} = E_0 + (E_s - E_0) \frac{I_s}{I} \tag{11}$$

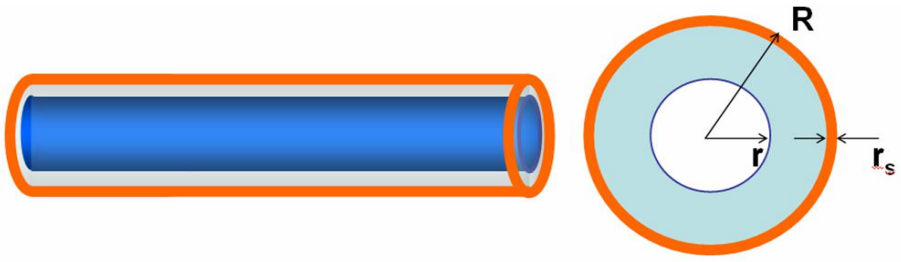


**Figure 31 Schematic illustration of the surface stiffening model. Left: 3D view. Right: cross section view. The layer with organ color indicated the stiffening layer.**

The moment of inertia of cross section of the modified lipid layer is:

$$I_s = \frac{\pi}{4}\left[R^4 - (R - r_s)^4\right] \tag{12}$$

The moment of inertia of cross section of the whole tubule is:

$$I = \frac{\pi}{4}(R^4 - r^4) \tag{13}$$

Substituting $I_s$ and $I$:

$$\frac{I_s}{I} = \frac{R^4 - (R - r_s)^4}{R^4 - r^4} = \frac{1}{R^4 - r^4}\left[4r_s R^3 - 6r_s{}^2 R^2 + 4r_s{}^3 R - r_s{}^4\right] \tag{14}$$

Neglecting the high order parameters, we obtained:

$$\frac{I_s}{I} \approx \frac{4r_s R^3}{R^4 - r^4} \tag{15}$$

Substituting equation (14) to equation (10):

$$E = E_0 + (E_s - E_0)\frac{4r_s R^3}{R^4 - r^4} \tag{16}$$

Equation (15) is used to fit the experimental results. The fitting curve is shown in Fig. 32. It can be seen that the tendency of the Young's modulus versus the outer radius of the lipid tubule described by Eq.(15) derived from the surface stiffening model fits reasonably well with the experimental results. The optimized curve fitting yields the values for three parameters, namely, bulk Young's modulus $E_0$ = 530 MPa, surface Young's modulus $E_s$ = 1400 MPa, and surface stiffening radius $r_s$ = 6.6 nm.

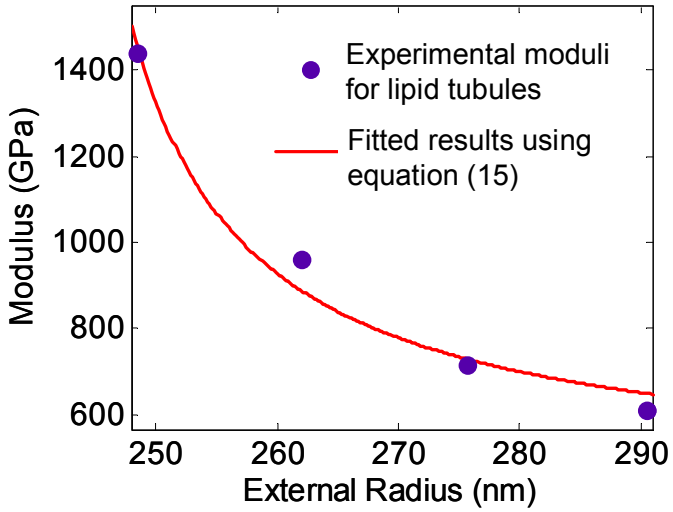


**Figure 32 Outer radius dependence of effective Young's modulus. Purple dots are experimental results, red line is fitted result by the surface stiffening model.**

## 3.4 Conclusion

In this chapter, axial and radial mechanical properties of $DC_{8,9}PC$ lipid tubules were studied with different loading methods: shrinking liquid droplet and nanoindentation.

Buckling of lipid tubules was studied by shrinking liquid droplet method. The interface tension of the shrinking liquid droplets exerted a compression force on the ends of the trapped lipid tubules, and caused them to buckle. This provided an efficient method to measure their axial mechanical properties. The axial bending rigidity and axial Young's modulus were calculated to be ~2.6×10-18Nm2 and ~1.07 GPa, respectively. As the strain energy of the buckled tubules built up, they poked through the interface of shrinking liquid droplets and then adhered onto glass substrates to form looplike shapes.

The persistence length of $DC_{8,9}PC$ lipid tubules was calculated to be ~ 41 μm by applying worm-like chain model and thus the relative flexibility of lipid tubules was estimated.

Radial deformation of $DC_{8,9}PC$ lipid tubules was studied using AFM tips as nanoindenters. From measured force-distance curves, a reversible linear region that persisted up to indentations of 15% of the tubule diameter was observed. Finite element model was established to model the lipid tubule—AFM tip system and to simulate the indentation process. Comparing simulating results with experimental force-displacement curves, the radial Young's modulus was estimated to be 705 MPa for $DC_{8,9}PC$ lipid tubules with 10 bilayer walls. Possible failure mechanisms for lipid tubules with different wall thickness were discussed by detailed von Miese stress analysis. For indentations larger then 15% of the diameters of $DC_{8,9}PC$ lipid tubules, a hysteresis and an instability/collapse corresponding to a drop in the FZ curve were observed. The recovery of the collapse of tubule walls was found after 6 minutes in water. The radial mechanical properties (in terms of elastic modulus and critical force for collapse) of $DC_{8,9}PC$ lipid tubules were found to be sensitive to the position along the long axel and the thickness of tubule walls. The axial dependency (end effect) could be explained by the break up of symmetric boundary conditions and the radial dependency (surface stiffening) was modeled by a composite lipid tubule with a modified lipid surface layer.

Comparing axial and radial elastic moduli calculated by different loading methods, we concluded that the elastic mechanical properties of $DC_{8,9}PC$ lipid tubules are anisotropic, which could be interpreted by the interactions between lipid molecules and lipid layers. Figure 33 is a schematic illustration of the origin of anisotropic mechanical properties of $DC_{8,9}PC$ lipid tubules. When $DC_{8,9}PC$ tubules were bearing an axial load,

the main resistance to axial deformation was from polymerized ene-yne linkages between lipid molecules (Fig. 33b). If $DC_{8,9}PC$ tubules were under radial loading, the interdigitations (intersectings) between lipid layers would be the dominant deformation form (Fig. 33c).

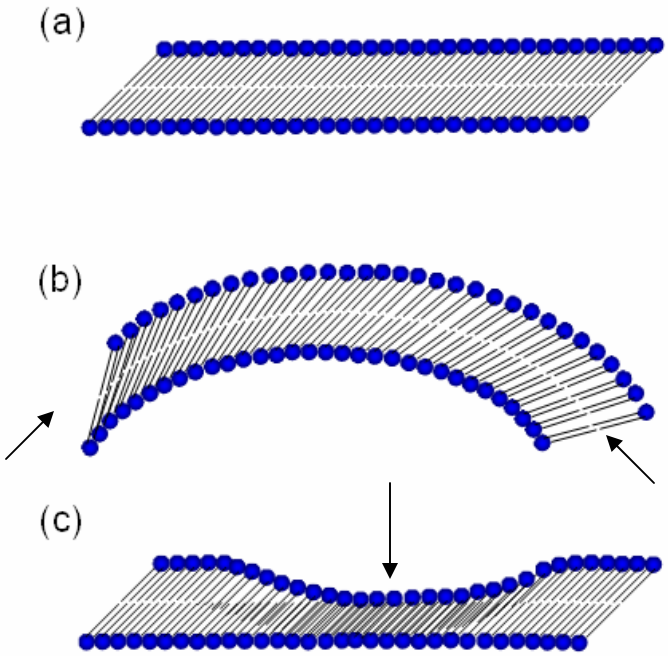


**Figure 33 Schematic illustration of the origin of anisotropic mechanical properties of $DC_{8,9}PC$ lipid tubules. A portion of lipid bilayer walls (a) without loading; (b) with axial loading; (c) with radial loading. The main resistance to axial deformation (b) came from polymerized ene-yne linkages between lipid molecules, while the radial deformation resulted in interdigitations between lipid layers (c).**

# CHAPTER 4
# ORDERED ARRAYS OF LIPID TUBULES

## 4.1 Introduction

Lipid tubules with hollow cylindrical shape have great potential as building blocks and organic templates in nanoelectronics and photonics[121]. However, this potential is limited in part by difficulties in precise control over their density, position, and orientation on substrates. Soft lithography, as a versatile and cost effective method for nano- and micro-fabrication, offers a solution.

### 4.1.1 Soft Lithography

Nuzzo noticed how long chain alkanethiolates could self-assemble on gold surfaces to give well-ordered monolayer films[122], now known as self-assembled monolayers (SAMs). Whitesides expanded upon the SAM methodology to develop the process of soft lithography. Soft lithography refers to a set of methods for fabricating or replicating structures using "elastomeric stamps, molds, and conformable photomasks"[123]. It is called "soft" because it uses elastomer such as poly-dimethylsiloxane (PDMS) as a mask, stamp, or mold. With this simple process, high-quality patterns and structures can be created with lateral dimensions from about 5nm to 500mm. Patterns can be two- and three- dimensional, and often cannot easily be achieved by photolithography.

Soft lithography includes the technologies of micro contact printing (μCP), microfluidic network (μFN), replica molding (REM), microtransfer molding (μTM),

micromolding in capillaries (MIMIC) and solvent-assisted micromolding (SAMIM), Patterning by etching at the nanoscale (PENs).

### 4.1.2 Hierarchical Assembly of Lipid Tubules on Substrates

It's well recognized that the assembly of lipid tubules into designed architectures on substrates over a large area is critical in developing their applications, and therefore, many efforts have been given in this research direction. Orwar and co-workers reported the assembly and manipulation of lipid tube networks with micropipet and electrofusion techniques[124,125]. Shimizu and collaborators described an approach in which a tubule of synthetic cardanyl-$\beta$-D-glucopyranoside could be aligned by microextruding an aqueous dispersion on glass substrates with a needle[126]. Fang's group developed a method that combines microfluidic networks and dewetting to produce two-dimensional ordered arrays of aligned tubules of $DC_{8,9}PC$ lipid on glass substrates[127]. It was found that the lipid tubules could be pulled into the microfluidic networks by the capillary force-induced channel flow and aligned along the channels. Locascio and co-workers reported the self-assembly of lipid tubules within microfluidic channels[128]. The bundles of self-assembled lipid tubules were found to grow along the microchannels. Recently, Lin and Dittrich fabricated epoxy microchips comprising microsized apertures and microchannels for the manipulation of lipid tubules by microfluidic technology[129,130].

## 4.2 Experimental Methods

### 4.2.1 Surface Pattern and Dip-coating Method

#### 4.2.1.1 Surface Design

##### 4.2.1.1.1 Substrate

There are five characteristics of gold that make it a good choice as a substrate for forming SAMs in our study. First, gold thin film is easy to obtain. It is straightforward to prepare gold substrate by physical vapor deposition, sputtering, or electrodeposition. Second, gold is a reasonably inert metal: it does not oxidize at temperatures below its melting point; it does not react with atmospheric $O_2$; it does not react with most chemicals. These properties make it possible to handle and manipulate samples under atmospheric conditions instead of under UHV-a great practical convenience for conducting experiments that require "dirty" conditions, e.g., microfabrication (outside of a clean room environment). Third, gold binds thiols with a high affinity[131], and it does not undergo any unusual reactions with them, e.g., the formation of a substitutional sulfide interphase[132]. Because thiols have a high affinity for gold, they also displace adventitious materials from the surface readily. Fourth, thin films of gold are common substrates used for a number of existing spectroscopies and analytical techniques, including SPR spectroscopy, quartz crystal microbalances (QCM), RAIRS, and ellipsometry. This characteristic is particularly useful for applications of SAMs as interfaces for studies in biology. Fifth, gold is compatible with most physiological environments. For instance, cells can adhere and function on gold surfaces without evidence of toxicity. SAMs

formed from thiols on gold are stable for periods of days to weeks when in contact with the complex liquid media required for cell studies[133,134].

4.2.1.1.2 Self-Assembled Monolayers (SAMs)

For SAMs formed from n-alkanethiols on Au substrate, the alkane chains adopt a quasi-crystalline structure where the chains are fully extended in a nearly all-trans conformation. The tilt of the chain projects an orientation of the average chain in which the sign of the tilt angle is conserved regardless of the number of carbons in the alkane chain. The chain tilt angle α was found pretty large on Au (111) surface compared to other metal surfaces, and it is about 30°[135,136]. This feature of the assembly leads to very different surface projections of the methyl groups for SAMs with odd and even numbers of methylene groups and correlates strongly with the unique wetting behaviors of SAMs on gold: SAMs of thiolates with an odd number of methylene groups produce surfaces whose free energies are systematically slightly larger than those with an even number of methylenes[137,138,139]. This is the so called "odd-even" effect for SAMs on gold substrates. Base on this effect, we considered thiolates with even number of methylenes to form SAMs deceasing surface energy greatly of Au substrate.

The other consideration is the length of the chain. Long-chain adsorbates are somewhat more robust in their applications than are short-chain adsorbates ($n < 10$) for reasons that are both kinetic and thermodynamic. Chain organizations within the SAM arise in part as a consequence of attractive lateral interactions. Longer chains are strongly driven to order by these contributions to the energetics, an effect that is further correlated with improvements in stability (thermal, chemical, etc.)140. So we chose 1-dodecanethiol (DDT, n=12) as monomers.

4.2.1.2 Dip-Coating

We developed a method by combining surface pattern and dip-coating. Fig.34a shows a schematic illustration of the preparation of a patterned Au substrate with the microcontact printing (μCP) technique. A poly(dimethylsiloxane) (PDMS) stamp having parallel channels was wet with 1mM 1-dodecanethiol (DDT) ethanol solution and then brought to contact with an Au (111) substrate for forming a pattern composed of alternating bare Au stripes and DDT self-assembled monolayers (SAMs) stripes. Fig.34b is a friction mode AFM image of the patterned Au substrate. As can be seen, the exposed Au stripes with a width of ~ 2 μm appear brighter than the methyl-terminated DDT SAMs stripes with a width of ~ 7 μm because they have higher friction force. We used the patterned Au substrate for guiding the adsorption of $DC_{8,9}PC$ tubules (Fig. 34c). It is clear from Fig. 34d that the tubules selectively adsorb on the bare Au stripes and aligned along the stripe direction. The AFM image shows that the tubules have a considerably smooth external surface and the helical markings are visible near the ends of tubules.

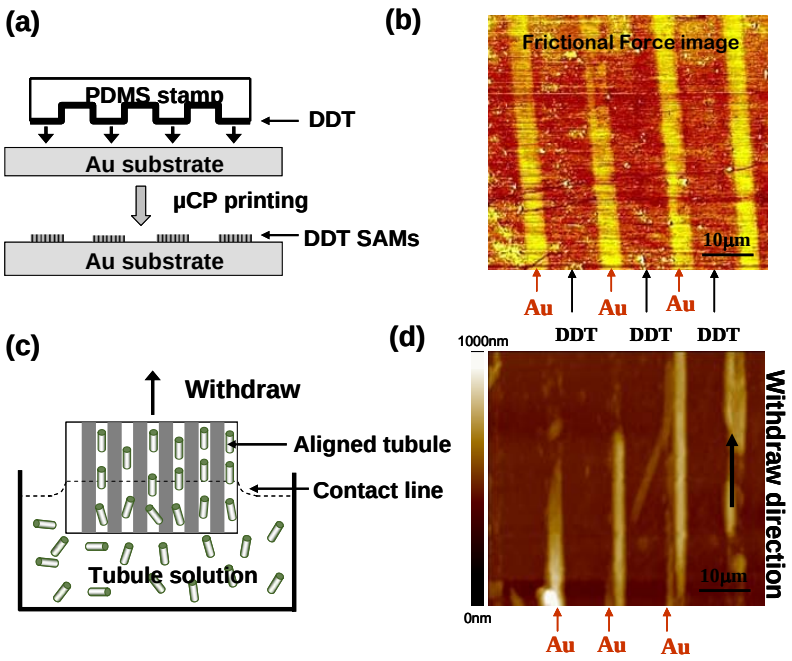


**Figure 34 Schematic illustration of the combination of μCP (a) and dip-coating (c) to position and align lipid tubules. (b) Contact mode frictional force images of patterned Au substrate. (d) Tapping mode topographic image of aligned tubules.**

The selective adsorption is likely due to the hydrophilic interactions between the Au stripes and the tubules. The gold surface is hydrophilic with a water contact angle of 38°, whereas the DDT SAMs surface is hydrophobic with a water contact angle of 110°. Because the external surfaces of $DC_{8,9}PC$ tubules are terminated by hydrophilic head groups, they prefer gold surface to DDT SAMs surface.

The withdrawal-induced alignment of the lipid tubules can be explained in the frame of moving contact line (Figure 35). When the patterned Au substrate is immersed into tubule suspension, a meniscus of the liquid is formed due to the surface tension. During withdrawing process, the tubules which adsorb on bare Au stripes are aligned perpendicular to the moving contact line which related to the surface tension.

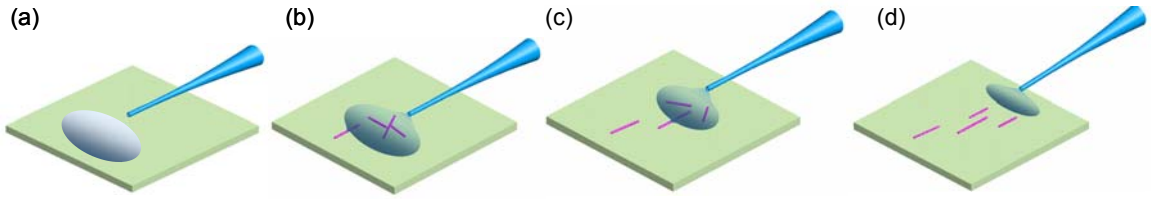


**Figure 35 Schematic illustration of aligning lipid tubules by the moving contact line method.**

### 4.2.2 Directly printing method

Figure 36 illustrates our approach which was used to align lipid tubes in the recessed channels of a thin PDMS stamp. A thin oxygen plasma treated PDMS stamp with parallel channels was carefully placed on a planar glass slide to form rectangular capillaries (Figure 36a). The capillaries are 0.8μm high and 1.0μm wide. The water contact angle on the glass slide and the oxygen plasma treated PDMS is about 8° and 12°, respectively. A drop of $DC_{8,9}PC$ tube suspension was placed along one of the opened ends of the hydrophilic rectangular capillaries, lipid tubes were pulled into individual capillaries by capillary action and aligned along the capillary direction (Figure 36b). The PDMS stamp was then quickly removed from the glass slide before the tube solution-filled capillaries were dried (Figure 36c). As can be seen from the optical microscopy image shown in Figure 36d, the aligned lipid tubes are kept inside the recessed channels of the PDMS stamp by surface tension.

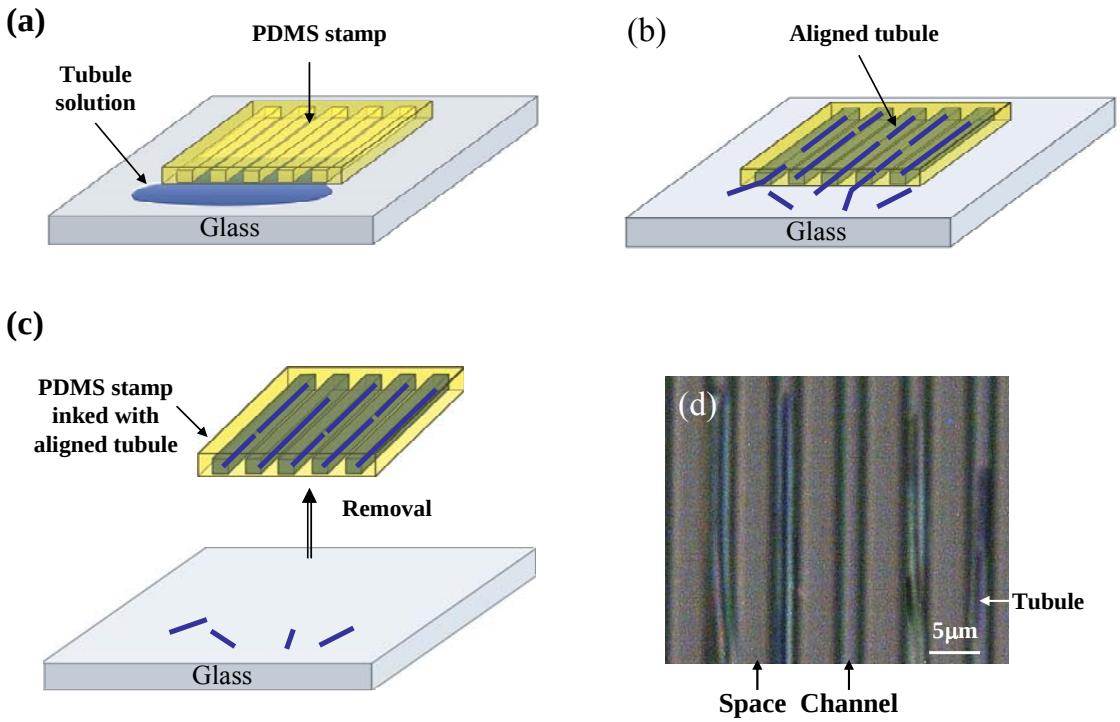


**Figure 36 PDMS stamp with aligned lipid tube "ink". (a-c) Schematic illustration of the microfluidic technique used to align lipid tubes in the recessed channels of a thin PDMS stamp. (a) Rectangular capillaries were formed by placing a PDMS stamp on a glass substrate. A drop of tube solution was placed along the one of opened ends. (b) The alignment of lipid tubes in the rectangular capillaries by capillary action. (c) The PDMS stamp was removed from the glass substrate before the tube solution-filled capillaries were dried. (d) Optical image of the aligned lipid tubes confined in the recessed channels of the PDMS stamp.**

## 4.3 Results and Discussion

### 4.3.1 Surface Pattern and Dip-coating Method

Examination of the aligned tubules on a large length scale with an optical microscope shows that a large number of the lipid tubules are aligned on the patterned Au substrate (Figure 37a). The position of the bare Au stripes on the patterned surface can be identified from the selective adsorption of impurities from tubule solution in the optical microscopy image. Several experiments were carried out for understanding the factors effecting the alignment of the lipid tubules on the patterned Au substrate.

4.3.1.1 Degree of Alignment vs. Withdrawal Rate

First, we found that the degree of the alignment of the lipid tubules depends on the withdrawal rate. Figure 37b shows the angular distribution of the aligned tubules at the withdrawal rate of 1 mm/min; 58% of the tubules are aligned within ±5° of the withdrawal direction. When the withdrawal rate increases to 10 mm/min, the angular distribution of the aligned tubules becomes substantially narrower (Figure 37c). More than 90% of the tubules are aligned within ±5° of the withdrawal direction.

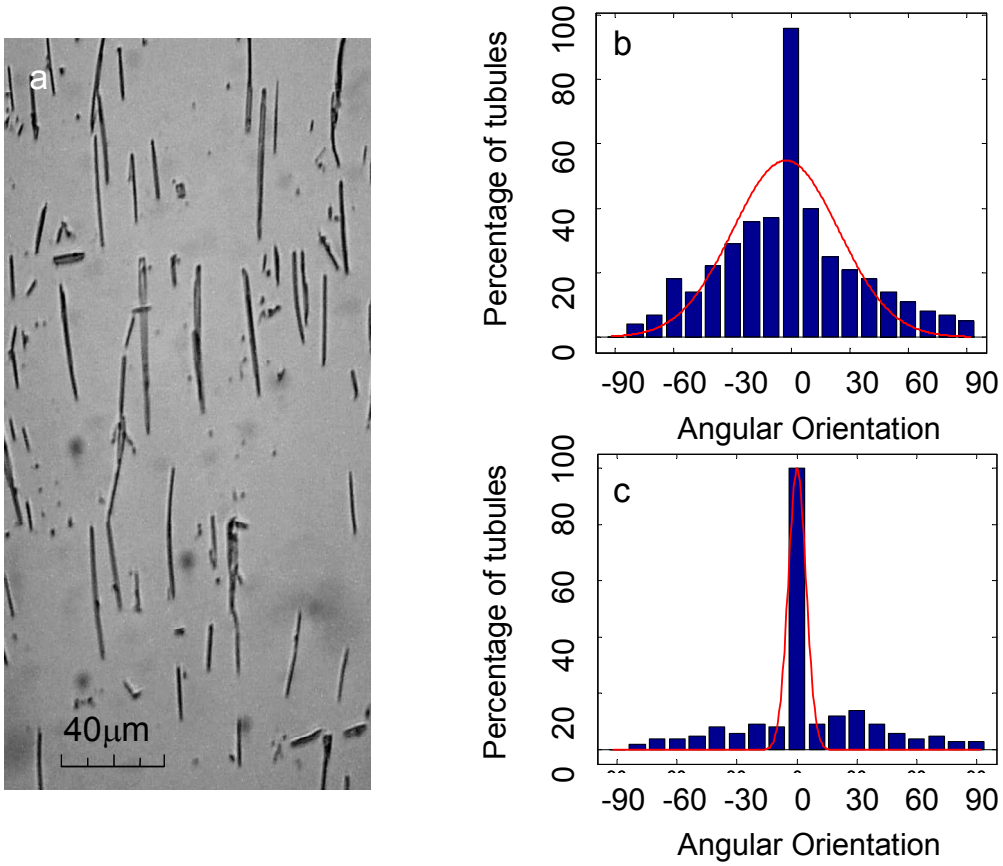


**Figure 37 (a) Optical microscope image of aligned lipid tubules on the patterned Au substrate. Histograms of the angles of the aligned lipid tubules away from the withdrawal direction with the fitted Gaussian distribution at the withdrawal rate of 1 mm/min (b) and 10 mm/min (c).**

4.3.1.2 Density of Alignment vs. Adsorption Time

Second, we found that the number of the aligned tubules increased as increase of the adsorption time at a constant withdrawal rate of 10 mm/min (Figure 38a,b). As can be seen from Figure 38c, the density of the aligned tubules increased quickly with the adsorption time and saturated with about 330 tubules per 500μm×500 μm after 8 hours. It is clear that a large number of lipid tubules can be aligned at a high density on patterned Au substrate.

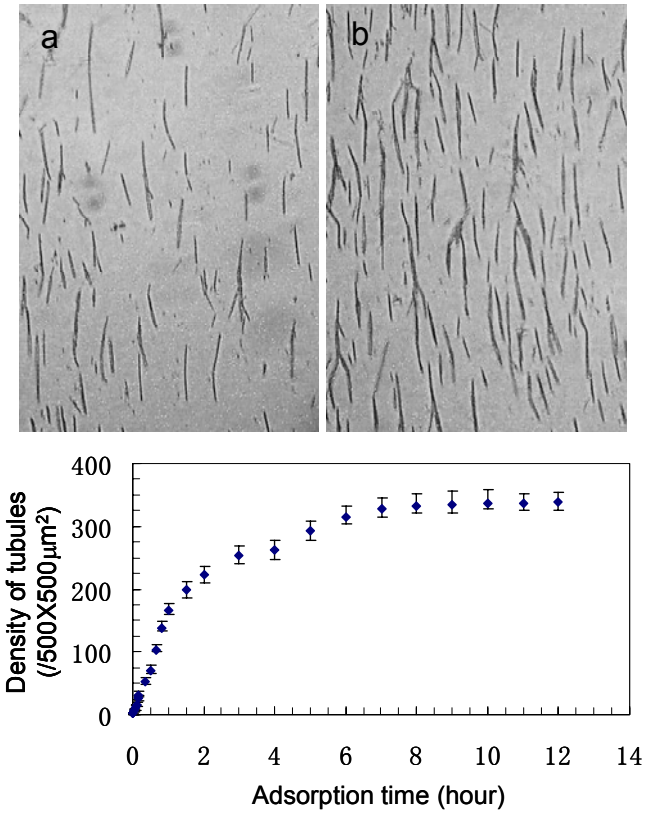


**Figure 38 Optical microscope images of aligned lipid tubules on the patterned Au substrate at a constant withdrawal rate of 10 mm/ min after 1 h (a) and 12 h adsorption (b). (c) Plots of the density of the aligned tubules vs adsorption time.**

4.3.1.3 Density of Alignment vs. Withdrawal Times

Third, we observed that the aligned tubules could be gradually added on the patterned Au substrate by multiple withdraws from the tubule solution. In this process, the tubules aligned on the patterned Au substrate by the first withdraw (Figure 39a) were dried in air at room temperature for 5 min and then immersed in the tubule suspension. The tubules that are aligned on the patterned Au substrate by the second withdrawal are circled in Figure 39b. The aligned tubules by the first withdrawal are stable during the second withdrawal process. Plots of the density of the aligned tubules vs withdrawal times at different withdrawal rates are shown in Figure 39c.

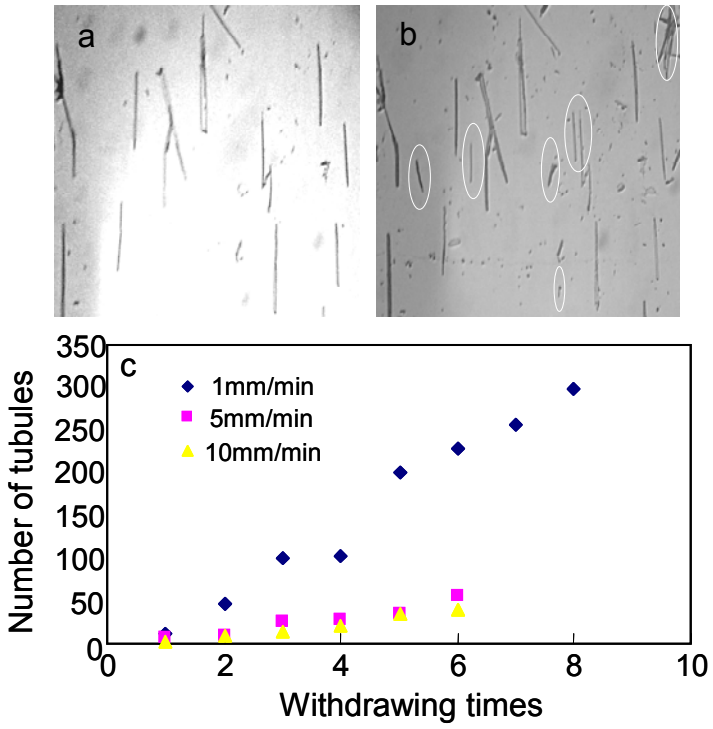


**Figure 39 Optical microscope images of aligned lipid tubules on the patterned Au substrate by first (a) and second (b) withdrawal processes at a constant withdrawal rate of 10 mm/min. (c) Plots of the density of the aligned tubules vs withdrawal times at different withdrawal rates.**

Based on those experiments, we conclude that the most efficient way to align tubules by dip-coating method is fast withdrawal rate (10mm/min), moderate adsorption time (1 hour), and multiple times withdrawing.

4.3.1.4 Degree of Alignment vs. Width of Au Stripes

I should point out that the patterned Au substrate alone does not provide good control of the tubule orientation. Figure 40a shows an optical microscopy image of the adsorption of lipid tubules on the patterned Au substrate. This image was taken in tubule solution. Some long lipid tubules tend to orient along the Au stripe direction due to the minimization of the lateral and rotational translations by the patterned surface. However, they show a large angular distribution with respect to the direction of the Au stripes. There is no orientation order observed for the short lipid tubules. This becomes clearer when the width of the Au stripes increases. As can be seen from Figure 40b, the short lipid tubules are preferentially adsorbed on the bare Au stripes with a width of about 10μm, but the orientation of the adsorbed short tubules is random.

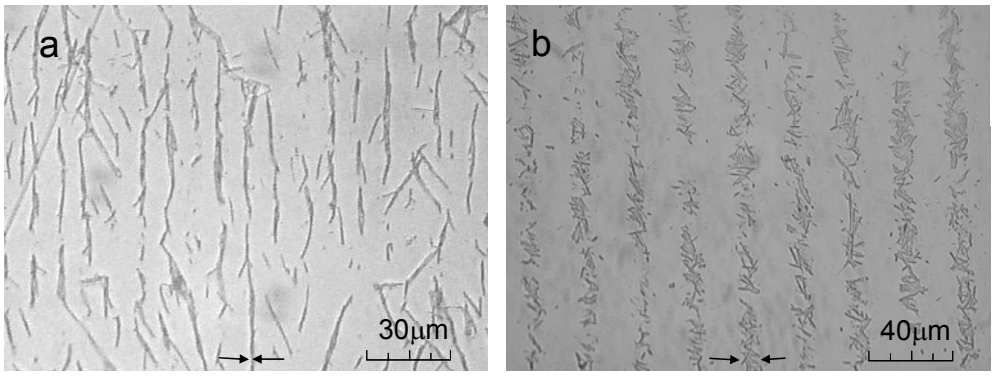


**Figure 40 Optical microscopy images of the lipid tubules absorbed on the patterned Au substrates. The width of the Au stripes is 2 μm (a) and 10 μm (b). These images were taken in tubule solution.**

### 4.3.2 Directly printing method

#### 4.3.2.1 2-D Ordered Arrays

##### 4.3.2.1.1 On Planer Au Surface

The PDMS stamp with lipid tubule "inks" provides a simple approach to directly print lipid tubules onto substrates of different types. For example, by bringing the tubule-inked PDMS stamp to contact with Au-coated mica and allowing the confined tube solution to dry in air at room temperature for a few hours, we find that the aligned lipid tubules are transferred onto the Au-coated mica from the recessed channels of the PDMS stamp. After removal of the PDMS stamp from the Au-coated mica, a 2D ordered array of aligned lipid tubules leaves behind (Figure 41a). This transfer process is determined by interfacial free energies. Since the interfacial free energy of PDMS (21.6 dyn/cm) [40] is much lower than that of the Au substrate (>72dyn/cm), lipid tubules preferentially adhere to the high surface energy Au-coated mica. The measured height of the aligned tubules shown in Figure 41a is about 425 nm, which agrees with the diameter of single $DC_{8,9}PC$ lipid tubules. The apparent width of the aligned lipid tubules in the AFM image is broad by the geometry of the AFM tip. The separation of the parallel-aligned tubules is about 5 μm. By designing PDMS stamp, the separation of the parallel aligned lipid tubules can be changed.

Figure 41b shows a 2-D tubule array in which the separation of the parallel aligned lipid tubules alternatively changes from 3 μm to 5 μm. It is known that the diameter of the $DC_{8,9}PC$ lipid tubules is ~ 500 nm with little variation. The height variation of the aligned lipid tubules can be seen in Figure 41b. We also note that the

aligned lipid tubules exhibit a flattened surface. The deformation is a result of the drying in air during the sample preparation. Despite the deformation, there are no cracks observed on the tubule surfaces.

A cyanine dye (3,3'-dipropylthiadicarbocyanine iodide) was used to examine whether the aligned lipid tubes are still hollow. In our experiments, the aligned lipid tubules were dried in air at room temperature for a week to remove water from their hollow cores and then exposed to an ethanol solution containing the dye molecules at a concentration of $2.28 \times 10^{-4}$ mol/L for 5 min. The dye molecules were loaded into the lipid tubules by capillary action. After loading, the sample was gently washed with ethanol to remove the dye molecules adsorbed on the external surface of the aligned lipid tubules. The state of the dye-loaded tubules was observed by a fluorescence microscope. Figure 41c shows a fluorescent tubule array. As can be seen, not all the aligned lipid tubules exhibit uniform fluorescence. A partially loaded tubule with aligned florescent dots is also observed. It is likely that the air trapped in the lipid tubule prevents the loading of the dye solution. To identify the nature of the fluorescent tubule, we performed a control experiment by exposing the hydrated tubule array to the same dye solution for 5 min. No fluorescent tubules are observed. Thus, we concluded that the fluorescence shown in Figure 40c is from the dye molecules loaded in the hollow cores of the aligned lipid tubules and rather than from their external surfaces. The aligned lipid tubules are still hollow.

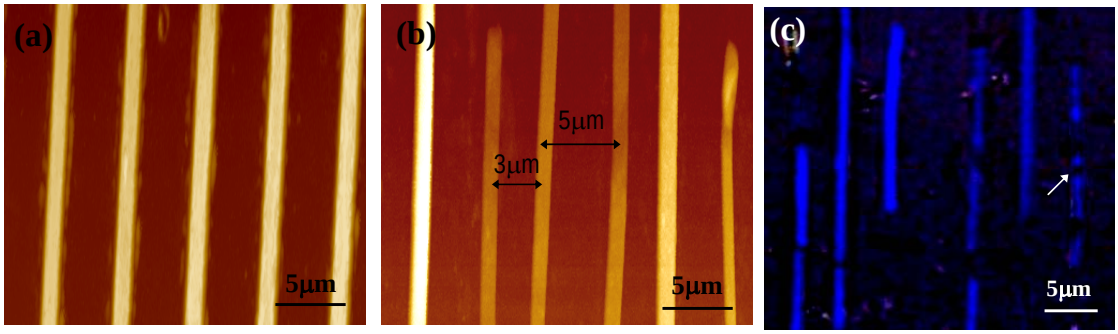


**Figure 41 2-D ordered arrays of aligned lipid tubules on planar Au-coated mica. Tapping-mode AFM images of parallel aligned lipid tubes with a constant separation (a) and varied separations (b) on Au-coated mica. (c) Fluorescence microscopy image of cyanine dye-loaded tubule arrays. The white arrow in (c) indicates a partially loaded lipid tubule**

4.3.2.1.2 On Patterned Au Electrodes

One of the advantages of our method is that the aligned lipid tubes can be directly printed at predetermined sites of a patterned substrate. Figure 42a shows a 2D array of aligned lipid tubes which are selectively printed on a square Au electrode with a thickness of ~250 nm which are fabricated on a $SiO_2$ substrate by lithographical technique. As can be seen, a number of parallel aligned lipid tubes are across the square Au electrode. Figure 42b shows a 2-D array of aligned lipid tubes crossing stripe Au electrodes. The aligned lipid tubes span the stripe Au electrodes in an orthogonal configuration. The aligned tubes are bent the edges of the stripe Au electrodes (Figure 42c). High profiles along the lines shown in Figure 42c reveal that the height of the aligned lipid tube on the $SiO_2$ substrate and the protruded Au electrode is fairly constant (Figure 42d), suggesting that the tube is in contacting with both the $SiO_2$ substrate and the protruded Au electrode. In this case, the attractive interaction with the $SiO_2$ substrate and the Au electrode forces the printed lipid tubes to maximize its area of contact with these surfaces and conform to the topography of the patterned substrate. From the optical

microscopy images shown in Figure 4a and 4b, we see no breaks on these aligned lipid tubes on pattern Au electrodes despite the bending at the edges of Au electrodes. The broken tubes observed in the AFM image (Figure 42c) is a result of the tip scans. The ability of directly printing ordered tube arrays on patterned electrodes suggests that our approach is capable of being integrated with current fabrication technology.

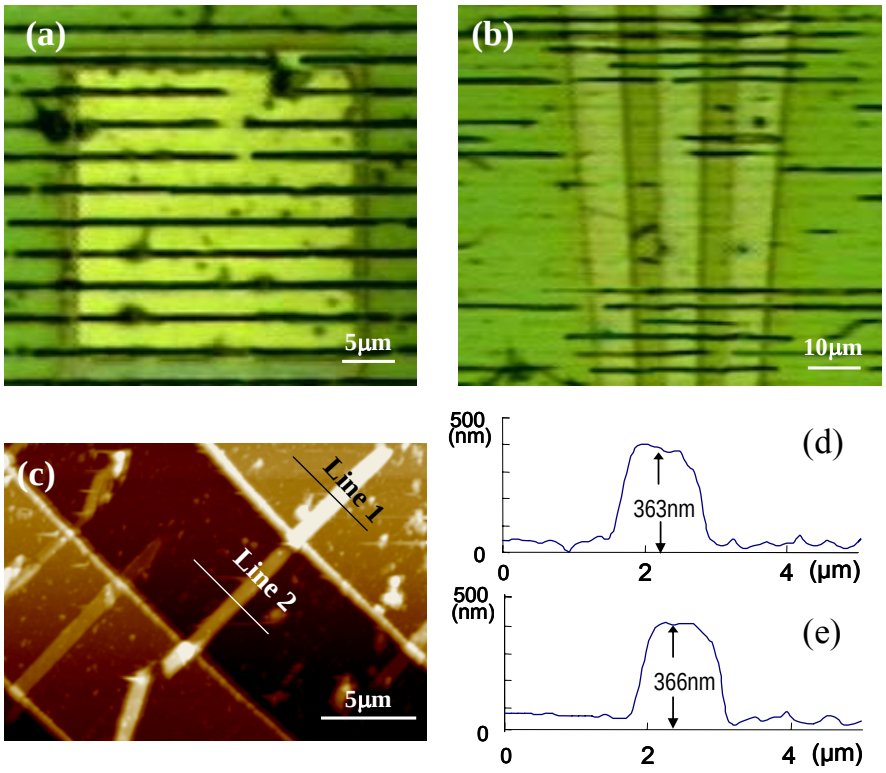


**Figure 42 2-D ordered arrays of aligned lipid tubules on patterned Au electrodes. Optical microscopy images of 2-D ordered tubule arrays printed on a square Au electrode (a) and stripe Au electrodes (b) which are fabricated on silicon wafers. Tapping mode AFM image (c) of an aligned tube across the stripe Au electrodes and high profiles (d and e) along the line 1 and line 2 shown in (c).**

4.3.2.1.3 On Curved Glass Tubes

To further test the feasibility of this approach, we printed the aligned lipid tubules on curved substrates. A glass capillary tube with a diameter of 1 mm was used in

our experiments. A thin PDMS stamp inked with aligned lipid tubules was brought to contact with the glass tube (Figure 43a). Because of elastic properties, the thin PDMS stamp can be bent to form a conformal contact with the curved surface of the glass tube. After the confined tubule solution was dried in air at room temperature, we peeled the PDMS stamp from the glass tube (Figure 43b). We found that the aligned lipid tubules could be transferred onto the curved glass tube from the recessed channels of the PDMS stamp. By changing focal planes, we observed that 2D tube arrays can be achieved seen over a large area on the curved glass tube (Figures 43c and d). Although fluidic flow has been successful in aligning elongated biomolecules such as DNA molecules[141, 142], peptide tapes[91], and tobacco mosaic virus[92], the separation of these parallel aligned biomolecules is essentially no control. It is also difficult to use fluidic flow to construct ordered arrays of elongated biomolecules on patterned and curved surfaces. It is believed that our approach can be used to print ordered arrays of these elongated biomolecules on patterned and curved substrates, which will open up a simple way to integrate them into chemical sensors, nanofluidic systems, and electronic devices.

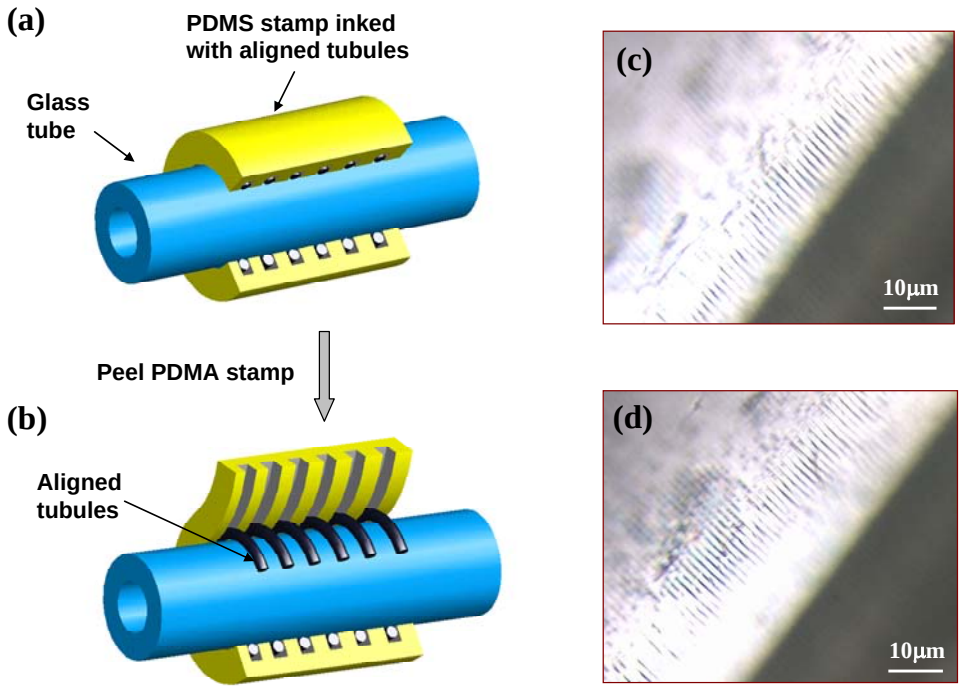


**Figure 43 2-D arrays of aligned lipid tubules on curved glass tubes. (a-b) Schematic illustration of printing 2-D ordered tubule arrays on a glass tube with a thin PDMS stamp inked with aligned lipid tubules. (c-d) optical microscopy images of 2-D tubule arrays on the glass tube at different focal planes.**

4.3.2.2 3-D Ordered Arrays

After printing the first layer of aligned lipid tubules, the process can be repeated by transferring the second layer of aligned lipid tubules for constructing a more complex, multilayered pattern of lipid tubules. For example, by rotating the tubule-inked PDMS stamp 90° during the second print we formed a 3D cross-bar junction of two aligned lipid tubules (Figure 44a). As can be seen, the upper tubule bends when it flexed around the lower tubule. It has been shown that the stiffness of $DC_{8,9}PC$ lipid tubules is about 0.8-1.5 N/m[143]. The molecular weight and the interaction with the Au surface forced the upper tubule with moderate stiffness to bend at the junction to maximize its area of contact with the surface. In addition, we noted that both upper and lower tubules in the

cross-bar configuration were flattened when they were imaged in air under ambient condition. If the cross-bar junction of two aligned tubules was imaged with AFM in a humidity chamber, we found that the flattened tubules resumed their cylindrical shapes, suggesting that the deformation was elastic. Figure 44c is an AFM image of a 3-D network of lipid tubules in a cross-bar configuration which was constructed on Au-coated mica by the layer-by-layer printing. It is known that there is a repulsive force between lipid tubules. The formation of the 3-D cross-bar junction network suggests that the interaction of the lipid tubules with the Au-coated mica is sufficiently strong so the transfer of the second layer takes place. It is also clear that the first layer tubules is stable on the Au surface and do not destroyed by the second printing.

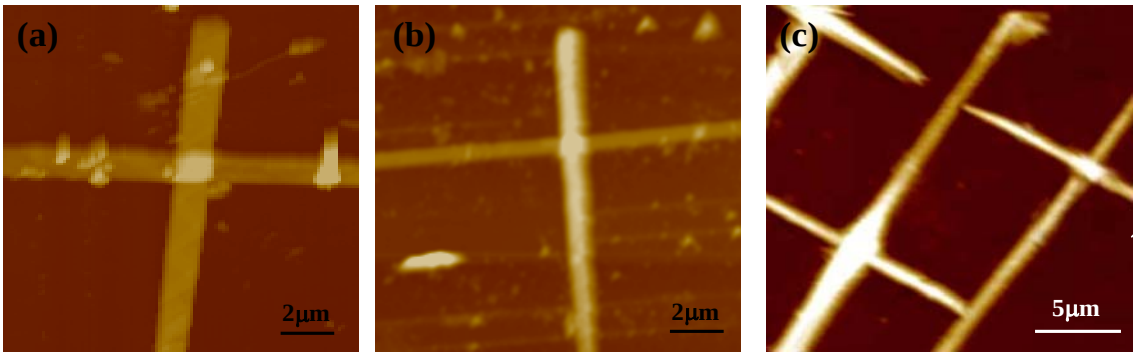


**Figure 44 3-D cross-bar junctions of aligned lipid tubes on planar Au-coated mica. Tapping-mode AFM images of a cross-bar junction of two aligned lipid tubules (a and b) and a cross-bar junction network of aligned lipid tubules (c). Figure 3a was taken in air. Figures 3b and 3c were taken in a humidity chamber.**

## 4.4 Conclusion

In this chapter, we reported a method for positioning and aligning the self-assembled lipid tubules by withdrawing a patterned Au substrate with alternating bare Au stripes and thiol monolayer stripes from tubule solution. We find that the tubules

selectively adsorb on the bare Au stripes. The moving contact line during the withdrawing process is responsible for the alignment of the lipid tubules. The angular distribution and the density of the aligned tubules depend on the withdrawal rate and the adsorption time, respectively. This method allows us to rapidly align a large number of lipid tubules on substrates, which is critical in developing some of the applications of the lipid tubules.

Another convenient method for construction of 2-D arrays and 3-D cross-bar junctions of aligned lipid tubules on planar Au coated mica, patterned Au electrodes, and curved glass tubules that is an extension of the standard μCP technique has been demonstrated, wherein the aligned lipid tubules which are confined in the recessed channels of a thin PDMS stamp serve as an "ink" in the printing process. The ordered arrays and 3-D cross-bar junctions of aligned lipid tubules have been characterized by optical microscopy and atomic force microscopy.

The comparisons of these two methods are summarized in Table 4.

**Table 4 Comparisons of methods for aligning and assembly lipid tubules.**

| Dip-coating and surface pattern | Direct printing |
|---|---|
| *Pro:*<br>1.Mass production<br>2. Large area ($3\times2cm^2$). | *Pro:*<br>1. Precision of position and orientation.<br>2. Varity of surfaces.<br>3. Layer by layer structures.<br>4. High density. |
| *Con:*<br>1. Precision of position and orientation.<br>2. Substrates' surface has to be smooth and planar.<br>3. Cannot form 3-D ordered structures.<br>4. Low density. | *Con:*<br>1. Number of tubules aligned.<br>2. Small area ($1\times1cm^2$). |

# CHAPTER 5
# TUBULE ARRAY TEMPLATING

## 5.1 Introduction

The hollow cylindrical shape, crystalline molecular order of bilayer walls, axial flexibility, and radial stiffness make lipid tubules attractive as templates for the synthesis of functional materials with controlled shapes and sizes[144,,145146,147,148,149]. There has also been great interest in using the self-assembled supramolecular structures of amphiphilic surfactants as templates for synthesizing ordered silica structures because of their potential applications in catalysis, separation technology, photonics, and bioengineering[150,151,152]. Baral and Schoen[153] reported the formation of silica hollow cylinders by the gel of ~10 nm silica colloidal particles on lipid tubules. However, the templated silica hollow cylinders have thick walls. Shimizu and co-workers[154,155] found that silica hollow cylinders with ultrathin walls could be formed by direct sol-gel reaction of tetraethoxysilane (TEOS) on the nanotubes of amino acid based and cholesterol-based lipids. Mann and co-workers[156] synthesized silica-lipid lamellar tubules by carrying out the acid hydrolysis and condensation of TEOS coupled with the self-assembly of $DC_{8,9}PC$ in solution.

Filling hollow cylindrical lipid tubules with guest materials opens up a new route in designing supramolecular materials for a variety of applications. For example, Letellier et al.[157] observed the distribution of charged magnetic particles with a diameter of 7nm around $DC_{8,9}PC$ lipid tubules. They found that the positively charged magnetic nanoparticles could be filled into the hollow core of the lipid tubules, forming uniform

magnetic rods. Shimizu and coworkers[158] loaded the hollow tubules of glycolipid N-(11-*cis*-octadecennoyl)-*β*-D-glucopyranosylamine with gold and silver nanoparticles through capillary force. A continuous gold nanowire with a diameter of 20-30 nm was formed by removing the lipid tubule shell under the firing at 500-750°C. The loaded lipid tubules with drugs, proteins, and plasmid DNA has shown promise as a new controlled release system for marine antifouling and tissue regeneration[159, 160]. Liquid crystals are anisotropic "fluids" with a large birefringence and tunable refractive index[81]. Here, we report the fabrication of optical anisotropic fibers with straight, zigzag, and loop shapes by filling and aligning of nematic liquid crystals in the hollow core of the cylindrical $DC_{8,9}PC$ through capillary action. The birefrongent nature of the lipid tubules with the 5CB core is examined by a polarizing optical microscope. By filling the 5CB liquid crystal into parallel aligned tubules, we form an ordered array of optical anisotropic fibers.

## 5.2 Experimental Method

### 5.2.1 Hybrid Silica-Lipid Tubes

Tetraethoxysilane (TEOS) was obtained from Aldrich and used as received. In our experiments, 20.6 μL of TEOS was first added to 2 mL of $DC_{8,9}PC$ tubule suspension. A solution (1.8 mL), which was prepared from $H_2O$ (50 mL) and 35.5 wt % aqueous HCl (10 μL), was added to the tubule/TEOS mixture. The mixture was allowed to stand undisturbed at room temperature for 1 week and then centrifuged at 5000 rpm for 10 min, and the supernatant was decanted. A drop of solution containing the hybrid silica-lipid cylinders was placed on carbon-coated grids and Au-coated mica substrates and then dried in air at room temperature.

To get ordered silica-lipid tubes arrays, $DC_{8,9}PC$ tubules were first aligned on the Au substrate by methods described in Chapter 4. Then, the ordered arrays of $DC_{8,9}PC$ tubules were used as templates to form ordered arrays of hybrid silica-lipid tubes by TEOS sol-gel reactions described above (Figure 45).

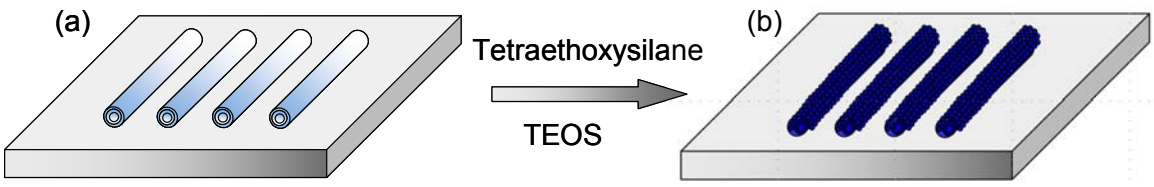


**Figure 45 Schematic illustration of formation of lipid tubule array-templated synthesis of aligned and patterned silica-lipid hybrid cylinders.**

Scanning electron microscope (JEOL 6400F) was used to obtain high resolution images of the silica-lipid hybrid tubes. The images were taken at the voltage of 10kV and the magnification of 20,000x. The sample (2-3mm in length) was prepared on the thin gold substrates and tried at room temperature for about 12 hours. The chemical composition of individual hybrid tubes was analyzed by energy-dispersive spectroscopy (EDS). Reflection Fourier transform infrared (FT-IR) spectra of hybrid silicalipid cylinders on Au-coated mica substrates were recorded with a Perkin-Elmer (100) spectrometer operating at 4 $cm^{-1}$ resolution. Each spectrum represents an average of eight scans.

### 5.2.2 Optical Anisotropy Fibers

The $DC_{8,9}PC$ lipid tubules were placed on a cleaned glass substrate and then dried in nitrogen environment for a week to remove water from the hollow core of the

tubules. Microfluidic networks (μFN) were used to align lipid tubules on glass substrates. In the μFN technique, an oxygen plasma treated PDMS stamp having parallel channels was carefully placed on a cleaned glass substrate to form parallel channels. The channels have a height of 0.8 μm and a width of 1.0 μm. The separation of the parallel channels is 5 μm. A droplet of the tubule suspensions was pulled into the rectangular channels from one of the opened ends by capillary action. The tubule solution-filled capillaries were dried in air at room temperature before removal of the PDMS stamp. 4-pentyl-4'-cyanolbiphenyl (5CB) (BDH, Ltd.) liquid crystal was filled into the hollow core of dried lipid tubules at the isotropic phase (T > 35°C) by capillary action and then cooled into the nematic phase. The 5CB liquid crystal adsorbed on the external surface of the tubules was washed away with ethanol.

A polarizing optical microscope (BX 40 Olympus) with a digital camera (Olympus C2020 Zoom) was used to observe optical textures of the lipid tubules with the 5CB core. For the polarizing microscope, the optics was adjusted to complete extinction before placing samples on the stage. Image analysis was performed with MATLAB software. AFM (Dimension 3100, Digital Instruments) was used to image the external surface of the lipid tubules. Silicon nitride cantilevers (Nanosensors) with a normal spring constant of about 30 N/m and a resonant frequency of about 260 kHz were used. The size of the cantilever tips (radius of curvature) is about 20 nm according to the manufacturer. The cantilever was excited just below its resonant frequency. All AFM measurements were performed in the tapping mode at a scan rate of 0.5 Hz in air under ambient conditions.

## 5.3 Results and Discussion

### 5.3.1 Hybrid Silica-Lipid Tubules

#### 5.3.1.1 Scanning Electron Microscopy

We find that 2-D arrays of aligned $DC_{8,9}PC$ tubules can be transcribed into 2-D ordered arrays of aligned silica-lipid cylinders through the templated sol–gel reaction of TEOS on tubule walls (Figure 46a). The deposition occurs on the external surface of aligned lipid tubules, which is exposed to the solution. The templated silica-lipid cylinders are expected to be hollow half-cylinders. The templated 2-D silica-lipid hybrid cylinder array appears to have smooth surfaces. The presence of P from the lipid head-groups and Si from silica thin films is confirmed in the EDS (Figure 46b).

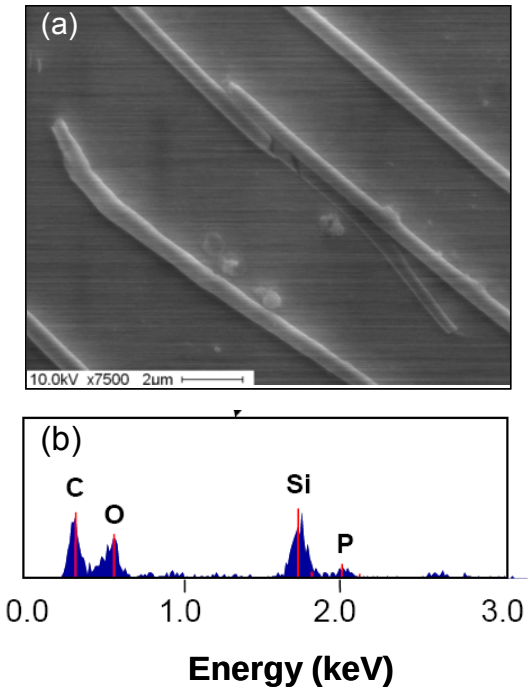


**Figure 46 (a) SEM image of 2-D arrays of templated silica-lipid hybird cylinders formed by sol-gel reaction of TEOS on tubule walls on Au-coated mica substrate. (b) Energy dispersive spectrum confirms the deposition of silica.**

Figure 47 shows FT-IR spectra of thermally treated hybrid silica-lipid cylinders which were dried on an Au-coated mica substrate. The FT-IR spectra were taken at room temperature after thermal treatment at 110°C in air for 2 h. The hybrid silica-lipid cylinders retain their hollow cylindrical geometries. In the region from 3000 to 2800 $cm^{-1}$ (Figure 47a), we observe two bands at 2916 and 2849 $cm^{-1}$, respectively. They can be straightforwardly assigned to the asymmetric and symmetric stretching vibrations of the $CH_2$ in the acyl chains of $DC_{8,9}PC$ molecules. The stretch frequency and the full width at half-maximum of the $CH_2$ symmetric stretching are in good agreement with the earlier reports of infrared spectra for $DC_{8,9}PC$ tubules in solution at room temperature by Rudolph and Burke[161]. They found that the asymmetric and symmetric stretching vibrations of the $CH_2$ in $DC_{8,9}PC$ tubules started to shift at 47°C. This suggests that the deposition of the silica films improves the thermal stability of lipid tubules and the lipid bilayer wall confining the hybrid silica-lipid cylinders retains its crystalline structure after the thermal process. The bands at 968, 804, and 719 $cm^{-1}$ correspond to C-C stretching, C-H bending, and $CH_2$ rocking, respectively. It is known that Si-O-Si vibration band appears as a broad feature between 1000 and 1200 $cm^{-1}$. In the region between 700 to 1500 $cm^{-1}$ (Figure 47b), we observe an intense band with a maximum at 1084 $cm^{-1}$, with a shoulder at 1200 $cm^{-1}$, which is consistent with the formation of highly cross-linked Si-O-Si networks on $DC_{8,9}PC$ tubules. It is clear that the deposition of the silica film improves the thermal stability of $DC_{8,9}PC$ tubules

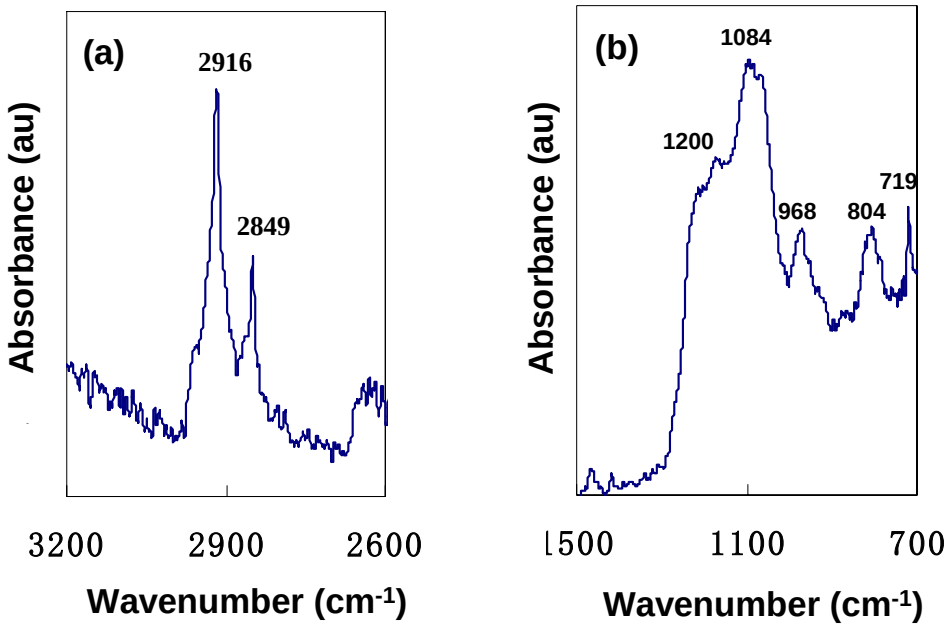


**Figure 47 FT-IR spectra of hybrid silica-lipid tubules placed on Au-coated mica. (a) Region between 3200 and 2600 $cm^{-1}$. (b) Region between 1500 and 70 $cm^{-1}$. The hybrid silica-lipid cylinders were dried on Au-coated mica and then were heated to 110 °C for 2 h. The spectra represent an average of four scans taken with a 2 $cm^{-1}$ resolution at room temperature.**

It is known that the $DC_{8,9}PC$ lipid is zwitterionic rather than charged, so the deposition of acid hydrolyzed TEOS on $DC_{8,9}PC$ tubules cannot be explained by charge interactions. Mann and co-workers suggested that $Br^-$ counterions served as a bridge for the deposition of positively charged TEOS on zwitterionic $DC_{8,9}PC$ lipids in HBr aqueous solution[156]. In our experiments, The deposition and condensation of TEOS on $DC_{8,9}PC$ tubules were carried out in HCl aqueous solution. However, the presence of $Cl^-$ counterions in the hybrid lipid-silica cylinders is not confirmed by EDS (Figure 46b). On the other hand, the curvature of bilayer membranes is known to induce a net electrostatic polarization normal to the membrane, producing a flexoelectric effect[162]. The curvature of a cylindrical lipid tubule can lead a polarization of $\sim 10^{-12}$ C/m[163]. The flexoelectric effect of lipid tubules should have a substantial impact on the adsorption of charged

particles on their surfaces. It is known that under acid condition the alkoxide groups of TEOS are protonated[164].We speculate that the deposition of positively charged TEOS on the $DC_{8,9}PC$ tubules in HCl aqueous solution at pH 2.0 is due to the flexoelectric effect. The condensation of the deposited TEOS leads to the formation of silica films on $DC_{8,9}PC$ tubules. The advantage of our approach is that the synthesis, alignment, and pattern of the silica cylinders are achieved in a single-step process.

### 5.3.2 Optical Anisotropic Fibers

#### 5.3.2.1 Formation and Characterization

As known from everyday experience, when a capillary is set in contact with a wetting fluid, the fluid will be spontaneously filled into the capillary. The filling process of the 5CB liquid crystal in the hollow core of the $DC_{8,9}PC$ tubules by capillary action is described schematically in Figure 48a. A drop of the 5CB liquid crystal was brought to contact with one end of the dried lipid tubules on glass substrates. After filling the hollow core of the $DC_{8,9}PC$ tubules with the 5CB, the sample was washed with ethanol to remove the 5CB adsorbed on the external surface of the tubules. Figure 48b is a polarizing optical microscopy image of a partially filled tubule under crossed polarizers. The optical contrast in a polarizing optical microscope reflects the birefringence of materials. The hollow core of the tubule is lighted up by the 5CB in Figure 47b. The location of the liquid crystal-air interface is clearly visible in the partially filled tubule. The empty part of the tubule appears dark. The partially filled tubules are often observed if we fill the tubules in the nematic phase of the 5CB. Figure 48c is a polarizing optical microscopy image of a fully filled tubule under crossed polarizers. The entire core of the tubule is lighted up by the 5CB. Both edges of the tubule can also be identified in Figure

48c. We find that the birefringence is lost when the sample is heated into the isotropic phase (>35°C) of the 5CB but reappears when the sample is cooled down to the nematic phase, suggesting that the observed birefringence comes from the 5CB confined in the tubules. Also the diameter of the 5CB birefringence fibers is smaller than the external diameter of the tubules, again suggesting that the 5CB is indeed confined within the core of the tubule, rather than adsorbs on the external surface of the tubule. We also note that the filling of the 5CB into the tubules only occurs when water is removed. This can be achieved by drying the tubules in nitrogen environment for a week. There is no filling observed if the tubules are dried in air for a few days.

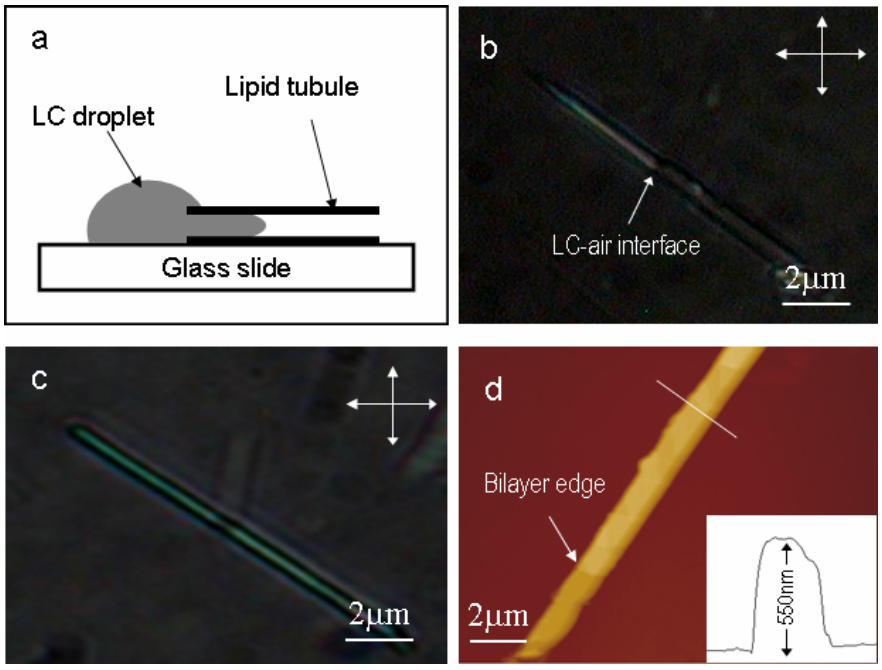


**Figure 48 (a) Schematic illustration of the filling process of lipid tubules with the 5CB. (b and c) Polarizing optical microscopy images of lipid tubules with the 5CB core. (d) AFM image of lipid tubules with the 5CB core. The directions of polarizer and analyzer were indicated by white arrays in b and c. The high profile along the white line drawn in d is inserted.**

After being dried for a week in nitrogen, we find that the tubules adsorbed on glass substrates deforms with a flattened external surface. If we fill the 5CB into the flattened tubules with the capillary action, they resume their cylindrical shapes. Figure 48d is a tapping AFM image of a tubule with the 5CB core. The external surface of the tubule appears to be considerably smooth and shows a cylindrical shape with a height of about 550 nm. The edge of helical bilayer ribbons forming the tubules is indicated with an arrow in Figure 48d. The measured thickness of the helical ribbons is about 14 nm, corresponding to a stack of two lipid bilayers. There are no liquid crystals observed on the external surface of the tubule. We also like to point out that if a thin 5CB layer adsorbed on the external surface of the tubules, imaging the tubules with AFM becomes impossible because of the fluidic nature of the 5CB at room temperature.

5.3.2.2 Optical Anisotropy

It is known that birefringent materials can change the incident polarization by splitting linearly polarized light into two perpendicularly polarized components, creating an elliptically polarized beam of light with a component capable of passing through the polarizer. When the incident light beam is vibrating parallel to the optical axis of birefringent materials, they appear dark under crossed polarizers because there is no splitting of the beam; this orientation is called the position of extinction. As the birefringent materials rotate away from the position of extinction, splitting of the beam occurs, and they appear bright. Therefore, the brightness of birefringent materials viewed under crossed polarizers relates to their orientation with respect to the polarization angle. The birefringent nature of the lipid tubules with the 5CB core is evident, when they are rotated between crossed polarizers. Here we find that the brightness of the tubules with

the 5CB core changes upon rotation of the tubules. The tubules become dark and disappear in the liquid crystal image if the direction of their axis is parallel to the polarizer and becomes bright if the direction is angle 45° to the polarizer the polarizer (Figure 49a-d).

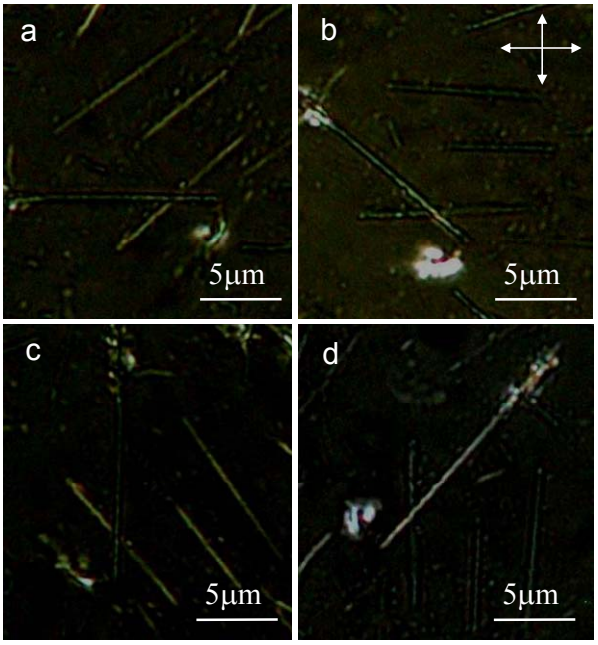


**Figure 49 (a-d) Polarizing microscopy images of lipid tubules with the 5CB core. Images were taken the sample was rotated in the plane between crossed polarizers. White arrows in (b) indicate the directions of polarizer and analyzer.**

The intensity of the transmitted light through a number of the tubules with the 5CB core was carefully measured during their rotation to quantify the uniformity of the 5CB orientation within the tubules with the image analysis. The strong modulation in the intensity of the transmitted light is observed (Figure50a). The tubules with the 5CB core show the maximum transmittance when they are oriented by 45° with respect to the polarizer and the minimum transmittance when they are either parallel or perpendicular to

the polarizer. This suggests that the 5CB confined the hollow core of the tubules have uniform orientation. The nematic director of the 5CB is further validated by observing the change of birefringence colors when a 1/4 wave plate is inserted into the optical path of the polarizing optical microscope, suggesting that the nematic director of the confined 5CB is indeed parallel to the tubule axis (Figure 50b), rather than perpendicular to the tubule axis.

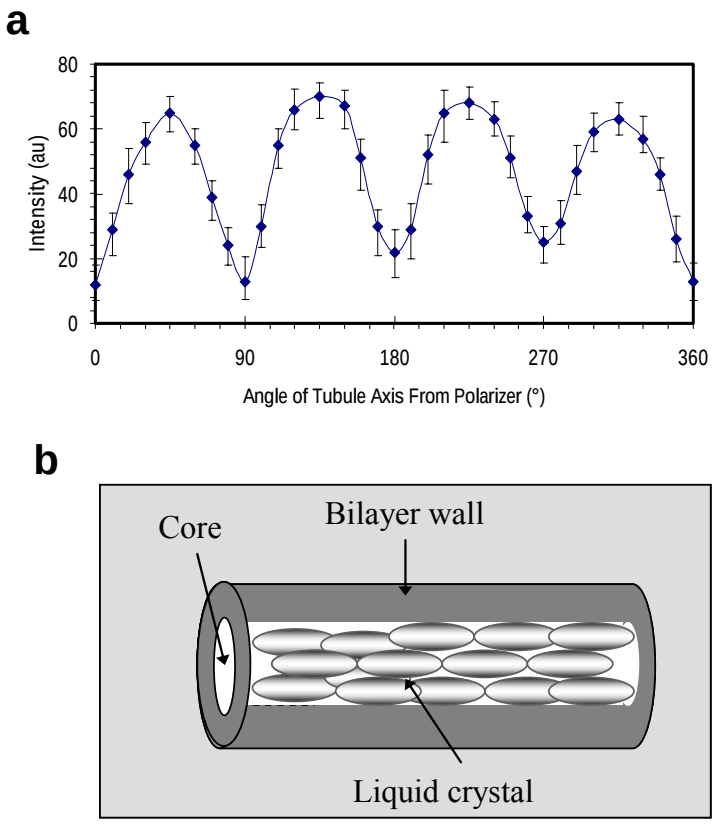


**Figure 50 (a) Plots of the intensity of the transmitted light through the tubules with the 5CB core as function of the angle between the direction of the tubules and the analyzer. The intensity measurements on different tubules were performed by image analysis with MATLAB software. (b) A possible alignment of the 5CB in the hollow core of the cylindrical tubule.**

In chapter 2, we studied that the orientation of the 5CB on the external surface of the tubules. In order to prevent the filling the 5CB in the tubules, water confined within the tubules core were not removed. We found that the organization of the molecular tilt

azimuth in the lipid tubules can induce an azimuthal orientation in the 5CB adsorbed on the external surface. On the uniform tilt tubules, we observed a uniform azimuthal orientation of the 5CB in a direction that was approximately 45° to the tubule axis. On the modulated tilt tubules, the 5CB showed a birefringence helical stripe. The transmitted intensity of light changed across the birefringence helical stripe. The change reflected the variations of the tilt azimuth direction of the 5CB across the birefringence stripes. The orientation of the 5CB confined in the hollow core of the tubules was different from that of the 5CB on the external surface of the tubules. The planar orientation of the 5CB in the tubule core is likely caused by capillary flow during the filling process. The capillary flow-induced orientation has been reported in different liquid-crystal cells[165,166].

5.3.2.3 Ordered Arrays by Microfluid Method

Nematic liquid crystals confined to cylindrical cavities have been extensively studied because of their applications in electro-optic devices[167,168,169,170]. One of the advantages of using the hollow lipid tubules as cylindrical cavities is their axial flexibilities as studied in Chapter 3. They can be easily assembled into ordered array and bent into defined shapes on substrates. Recently, our group has developed a method that combines microfluidic networks and dewetting to produce ordered arrays of aligned lipid tubules on glass surfaces[171]. Briefly, a PDMS stamp was brought to contact with a glass surface to form parallel rectangular channels. A droplet of tubule solutions was pulled into the parallel channels from one of the opened ends by capillary action (Figure 51a). Once the PDMS stamp was removed, parallel aligned tubules remained on the glass surface (Figure 51b). The parallel aligned tubules on a glass substrate were dried in nitrogen environment for a week to remove water from the core of the tubules. The filling

of the 5CB led to the formation of an ordered array of the optical anisotropy fibers (Figure 51c). AFM image shows that the parallel aligned tubules with flattened surfaces were separated by about 5 μm (Figure 51d). As can be seen from the polarizing optical microscopy shown in Figure 51e that after filling of the 5CB with capillary action the cores of the parallel aligned tubules were lighted up by the 5CB. Here the diameter of the confined 5CB birefringence fibers was smaller than the external diameter of the tubules. A two-dimensional ordered array of the optical anisotropy fibers with a separation of ~ 5 μm was formed.

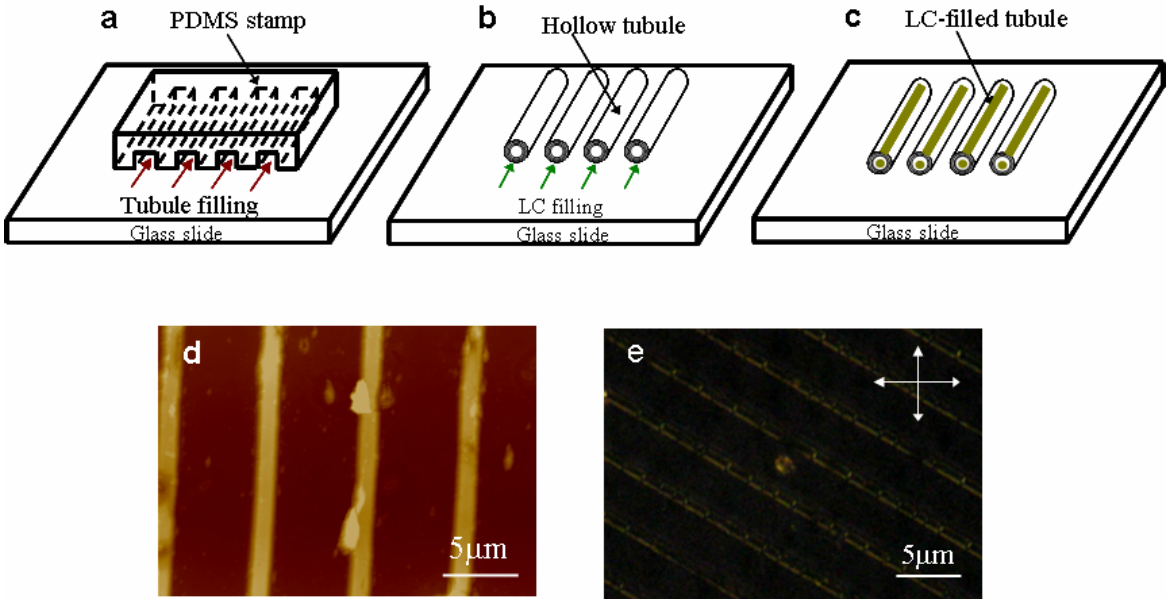


**Figure 51 (a-c) Schematic illustration of the microfluidic technique used to align lipid tubule on a glass substrate and the formation of 2-D ordered arrays of aligned lipid tubules with the 5CB core. (d) AFM image of parallel aligned lipid tubules on a glass substrate. (e) Polarizing optical microscopy image of the parallel aligned lipid tubules with the 5CB core. White arrows indicate the directions of polarizer and analyze.**

5.3.2.4 Zigzag Shapes by Moving Contact Line Method

Figure 52a is a schematic illustration showing how zigzag shaped tubules formed by moving contact line of $DC_{8,9}PC$ tubule solution in a confined space between substrates and PDMS stamps. For the bent tubule with zigzag shapes (Figure 52b), we found that the bending angle (the deviation angle from the long axis) was approximately 45°. Small buckling at the bending regions was visible. By filling the 5CB into these bent tubules by capillary action, we formed optical anisotropic fibers with zigzag shapes. It was clear that the portions of the zigzag shaped tubule were dark when they were parallel to the polarizer (indicated by white arrows in Figure 52c), while the portions appeared bright when they were oriented by 45° with respect to the polarizer. This also suggested that the hollow core of the cylindrical tubule was not closed by the bending.

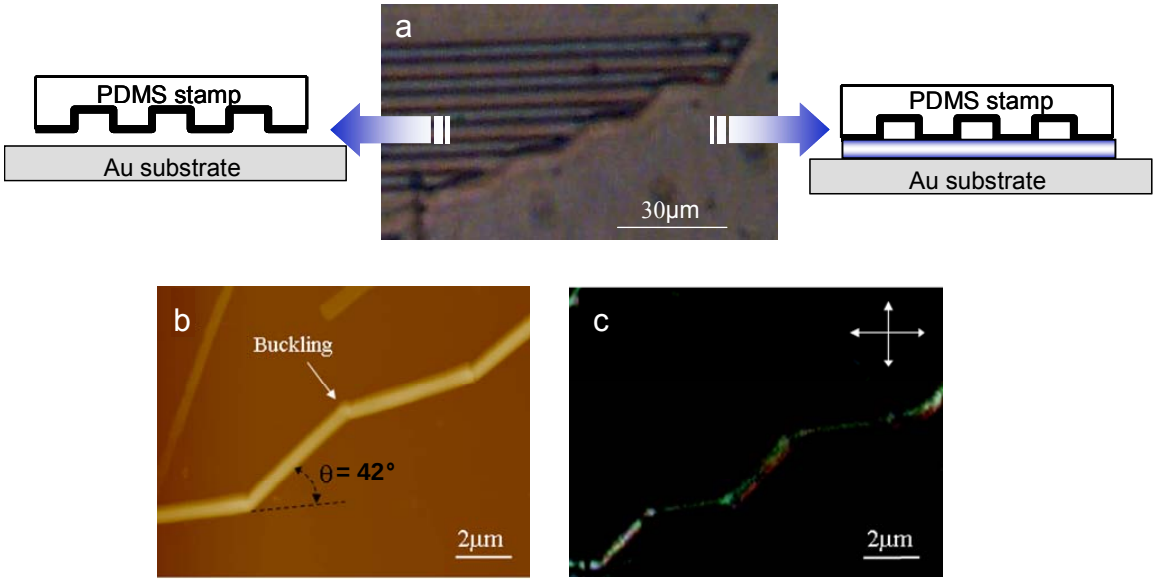


**Figure 52(a) Schematic illustration of the moving contact line in a confined space method used to form zig-zag shaped lipid tubules on a glass substrate. (b) AFM image of a zigzag shaped lipid tubule on a glass substrate. (c) Polarizing microscopy image of the zigzag shaped optical anisotropic fiber formed by lipid tubules with a 5CB core. White arrows in (c) indicate the directions of polarizer and analyzer.**

5.3.2.5 Loop-like Shapes by Shrinking Contact Line Method

Figure 53a is a schematic illustration of the formation of loop like shaped tubules by shrinking contact line of droplet method. Figure 53b is AFM image of the tubule with loop-like shape, the bending appeared to be gradually with a considerably smooth external surface. There were no wrinkles observed, suggesting a uniform bending stress distributed over the entire length of the tubules. By filling the 5CB into these loop-like shaped tubules by capillary action, we formed optical anisotropic fibers with loop-like shapes (Figure 53c). The portions of the loop-like shaped tubule were dark when they were parallel to the polarizer, while the portions appeared bright when they were oriented by 45° with respect to the polarizer. This also suggested that the hollow core of the cylindrical tubule was not closed during the bending process.

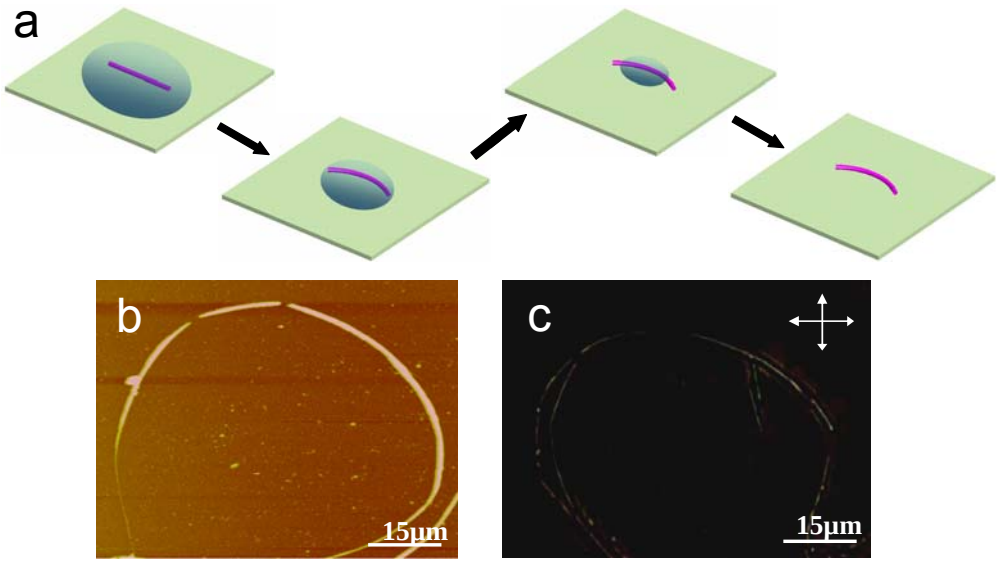


**Figure 53 (a) Schematic illustration of the shrinking contact line of a droplet method used to form loop-like shaped lipid tubules on a glass substrate. (b) AFM image of a loop-like shaped lipid tubule on a glass substrate. (c) Polarizing microscopy image of a loop-like shaped optical anisotropic fiber formed by lipid tubules with a 5CB core. White arrows in (c) indicate the directions of polarizer and analyzer**

## 5.4 Conclusion

In this chapter, potential applications of the 2-D ordered arrays of lipid tubules were developed by templating technique. The sol-gel condensation of tetraethoxysilane (TEOS) on 2-D ordered arrays of $DC_{8,9}PC$ tubules on glass substrates was reported. SEM revealed that the templated silica-lipid hybrid tubes in 2-D arrays had smooth surfaces. The deposition of the silica film substantially improved the thermal stability of lipid tubules. We found that the crystalline ordering of lipid bilayer walls confined in the hybrid silica-lipid cylinders is stable up to 110°C. The advantage of this approach is that the synthesis, alignment, and pattern of the silica cylinders are achieved in a single-step process. The ordered arrays of hybrid silica-lipid cylinders might have potential applications in heterogeneous chiral catalysis and separation.

By filling nematic liquid crystals into parallel aligned $DC_{8,9}PC$ tubules, an ordered array of optical anisotropic fibers was formed. The ability of synthesizing nano- and micron-sized optical fibers with well-defined shapes and of manipulating them on substrates are one of the keys in future miniaturized optoelectronics. Therefore, the filling of the flexible cylindrical lipid tubules with liquid crystals represented a simple route to fabricate optical anisotropic fibers with tunable sizes, shapes, and refractive indexes. The lipid tubules with the birefringent liquid-crystal core could have potential applications in sensors, photonic devices, and optical communications.

# APPENDIX
# FEA PROGRAMMING CODES

```
*HEADING
SDRC I-DEAS ABAQUS FILE TRANSLATOR  23-Oct-07   19:19:26
*NODE, NSET=ALLNODES, SYSTEM=R
        12, 4.2831360E-02, 0.0000000E+00, 1.8395014E+00
        13, 4.6788175E-02, 0.0000000E+00, 2.0094369E+00
      ..................................................
      7016, 0.0000000E+00, 6.0000000E+00,-2.5000000E+00
      9001, 0.0000000E+00, 6.0000000E+00, 2.6500000E+00
*SYSTEM
 0.0000E+00,-8.9888E-03,-3.1096E-03, 1.0000E+00,-8.9888E-03,-3.1096E-03
 0.0000E+00, 9.9101E-01,-3.1096E-03
*NODE, NSET=ALLNODES, SYSTEM=R
      8001, 1.5000000E-01, 6.0089888E+00, 2.6531096E+00
      8002, 0.0000000E+00, 5.8589888E+00, 2.6531096E+00
      ..................................................
      8103, 2.7289324E-02, 5.9456268E+00, 2.5199159E+00
*NSET,NSET=TR000001, GENERATE
     8001,     8103,        1
*TRANSFORM,NSET=TR000001,TYPE=R
 1.0000E+00, 0.0000E+00, 0.0000E+00, 0.0000E+00, 1.0000E+00, 0.0000E+00
*ELEMENT, TYPE=R3D4      , ELSET=INDENTERELEMENTS
   5001,   8001,   8021,   8090,   8004
   5002,   8078,   8022,   8002,   8012
   .....................................
   5087,   8101,   8103,   8102,   8100
*ELEMENT, TYPE=C3D8H    , ELSET=TUBEELEMENTS
      1,   6501,   6502,     13,     12,   6512,   6513,    354,    353
      2,   6502,   6503,     14,     13,   6513,   6514,    355,    354
   ..........................................................................
   4500,   5103,   5104,   7015,   6840,   6329,   6330,   7016,   6851
*SOLID SECTION,
 ELSET=TUBEELEMENTS,MATERIAL=LIPID
*MATERIAL,NAME=LIPID
*ELASTIC,TYPE=ISOTROPIC
 2.06800E+07,  3.90000E-01
*NSET,NSET=TOPTUBENODES,GENERATE
6001,6341,1
6666,6676,1
6842,6851,1
7016,7016,1
*NSET,NSET=CUTPLANENODES,GENERATE
6501,6852,1
*NSET,NSET=SUBSTRATENODES,GENERATE
7001,7016,1
*ELSET,ELSET=CONTACTBLANK,GENERATE
4210,4330,10
```

.....
1810,1930,10
**----------BOUNDARY CONDITIONS----------
*BOUNDARY
 TOPTUBENODES,2
 SUBSTRATENODES,1
 SUBSTRATENODES,3
 CUTPLANENODES,1
 9001,1,2
 9001,4,6
**----------CONTACT PARAMETER----------
*SURFACE,TYPE=ELEMENT,NAME=TUBE, TRIM=YES
 CONTACTBLANK,S4
*SURFACE,TYPE=ELEMENT,NAME=INDENTER
 INDENTERELEMENTS,SNEG
*RIGID BODY,REF NODE=9001, ELSET=INDENTERELEMENTS
*SURFACE INTERACTION,NAME=INDENTATION
*CONTACT PAIR,INTERACTION=INDENTATION
 TUBE,INDENTER
**----------DISPLACEMENT PARAMETERS----------
*STEP,NLGEOM
*STATIC
 0.01,1,0.01,0.01
*BOUNDARY
9001,3,3,-0.75
**----------OUTPUT PARAMETERS----------
*NSET,NSET=OUTPUTNODES
 6676,7016
*NODE PRINT, NSET=OUTPUTNODES
 U3,RF3
*ELSET, ELSET=OUTPUTELEMENTS
 4210
*EL PRINT, ELSET=OUTPUTELEMENTS
 S
*END STEP
**----------

# REFERENCES


1 Appenzeller, T. *Science* **1991**, *254*, 1300.

2 Xiang, J.; Lu, W.; Hu, Y.; Wu, Y.; Yan H.; Lieber, C.M. *Nature* **2006**, *441*, 489.

3 Whitesides, G. M.; Wong, A. P. *MRS Bulletin* **2006**, *31*, 19.

4 Salaita, K. S.; Wang, Y.; Mirkin, C. A. *Nature Nanotech.* **2007**, *2*, 145.

5 Whitesides, G. M.; Grzybowski, B. *Science* **2002**, *295*, 2418.

6 Isaacs, L.; Chin, D. N.; Bowden, N.; Xia, Y.; Whitesides, G. M. *Supramolecular Technology;* Wiley: New York, 1999.

7 Olenyuk, B.; Whiteford, J. A.; Fechtenkotter, A.; Stang, P. J. *Nature* **1999**, *398*, 796.

8 Piguet, C.; Borkovec, M.; Hamacek, J.; Zeckert, K. *Coordination Chem. Rev.* **2005**, *249*, 705.

9 Ozin, G. A.; Arsenault, A. C. *Nanochemistry—A Chemical Approach to Nanomaterials;* Royal Society of Chemistry: Cambridge, UK, 2005.

10 Danov, K.D.; Kralchevsky**,** P.A.; Ananthapadmanabhan, K.P.; Lips, A. *Langmuir* **2006,** *22*, 106.

11 Lehn J.M., *Science* **2002,** *295*, 2400.

12 Whitesides, G. M.; Boncheva, M. *Proc. Natl. Acad. Sci. U.S.A.* **2002,** *99*, 4769.

13 Lehn, J.M. *Supramolecular Chemistry: Concepts and Perspectives*; VCH press: Weinheim, Germany, 1995.

14 Lehn, J.M. *Science* **1993**, *260*, 1762.

15 Desiraju, G. R. *Crystal Engineering: The Design of Organic Solids;* Elsevier: New York, 1989.

16 Jakubith, S.; Rotermund, H. H.; Engel, W.; von Oertzen, A.; Ertl, G. *Phys. Rev. Lett.* **1990**, *65*, 3013.

17 Philip, D.; Stoddart, J. F. *Angew. Chem. Int. Ed.* **1996,** *35*, 1155.

18 Jones, M. N.; Chapman, D.; *Micelles, Monolayers and Biomembranes*; Wiley-Liss: New York, 1995.

19 Aizenberg, J.; Black, A. J.; Whitesides, G. M. *Nature* **1999**, *398*, 495.

20 Loudet, J. C.; Barois, P.; Poulin, P. *Nature* **2000**, *407*, 611.

21 Bowden, N.; Choi, I.; Grzybowski, B. A.; Whitesides, G. M. *J. Am. Chem. Soc.* **1999**, *121*, 5373.

22 Grzybowski, B. A.; Bowden, N.; Arias, F.; Yang, H.; Whitesides, G. M. *J. Phys. Chem. B* **2001**, *105*, 404.

23 Gracias, D.; Tien, J.; Breen, T. L.; Hsu, C.; Whitesides, G. M. *Science* **289**, 1170.

24 Shimoyama, N.; Sugawara, K.; Mizuguchi, T.; Hayakawa, Y.; Sano, M. *Phys. Rev. Lett.* **1996**, *76*, 3870.

25 Bonabeau, E.; Dorigo, M.; Theraulaz, G. *Nature* **2000**, *406*, 39.

26 Schnur, J.M. *Science* **1993**, *262*, 1669.

27 Singh, A.; Schnur, J. M. *Phospholipid Handbook;* G. Cevc, Ed. Dekker: New York, 1993.

28 Rudolph, A. S.; Calvert, J. M.; Schoen, P. E.; Schnur, J. M. *Biotechnological Applications of Lipid Microstructures*; B. P. Gaber, J. M. Schnur, D. Chapman, Eds. Plenum: New York. 1988.

29 Ringsdorf, H.; Schlarb, B.; Venzmer, J. *Angew. Chem. Int. Ed. Engl*. **1988**, *27*, 113.

30 Lasic, D.D. *Liposomes: From Physics to Applications*; Plenm: New York, 1993.

31 Johnston, D. S.; Sanghera, S.; Pons, M.; Chapman, D. *Biochim. Biophys. Acta* **1980**, *602*, 57.

32 Hub, H. H.; Hupfer, B.; Koch, H.; Ringsdorf, H. *Angew. Chem. Int. Ed. Engl.* **1980**, *19*, 938.

33 Kusumi, A.; Singh, M.; Tirrell, D. A.; Oehme, G.; Singh, A.; Samuel, N. K. P.; Hyde, J. S.; Regen, S. L. *J. Am. Chem. Soc.* **1983**, *105*, 2975.

34 Yager, P.; Schoen, P. E. *Mol. Cryst. Liq. Cryst.* **1984**, *106*, 371.

35 Yager, P.; et al., *Biophys. J.*, **1985**, *48*, 899.

36 Yager, P.; et al., *Biophys. J.*, **1986**, *49*, 320.

37 Georger, J. H.; Singh, A.; Price, R. R.; Schnur, J. M.; Yager, P.; Schoen, P. E. *J. Am. Chem. Soc.* **1987**, *109*, 6169.

38 Singh, A.; Schnur, J. M. *Polym. Prepr. Am. Chem. Soc. Div. Polym. Chem*. **1985,** *26*, 184.

39 Singh, A.; Schnur, J. M. U.S. Patent 4867917 (**1989**).

40 Johnston, D. S.; Chapman, D. *Liposome Technology*; G. Gregoriadis. Ed.; vol. 1; CRC Press: Boca Raton, FL, 1984.

41 Rudolph, A. S.; Singh, B. R.; Singh, A.; Burke, T. G. *Biochim. Biophys. Acta* **1988,** *943***.** 454.

42 Schoen, P. E.; Yager, P. R.; Priest, G. *Polydiacetylenes: Synthesis, Structure, and Electronic Properties*; D. B. Bloor, D. Chance., Eds. Kluwer Academic: Norwell, MA, 1985.

43 Schoen, P. E.; Yager, P.; *J. Polym. Sci. Polym. Phys. Ed.* **1985**, *23*, 2203.

44 Rhodes, D. G.; Blechner, S. L.; Yager, P.; Schoen, P. E. *Chem. Phys. Lipids* **1988**, *49*. 39.

45 Caffrey, M.; Hogan, J.; Rudolph, A. S. *Biochemistry* **1991**, *30*, 2134.

46 Lando, J.; Sudiwala, R. V. *Chem. Mater.* **1990,** *2*. 596.

47 Singh, A.; Schoen, P. E.; Schnur, J. M. *J. Chem.Soc. Chem. Commun.* **1988**, *1222*.

48 Singh A.; Marchywka, S. *Polym. Mater. Sci. Eng.* **1989**, *61*, 675.

49 Markowitz, M.; Singh, A. *Langmuir* **1991**, *16*.

50 Markowitz, M.; A. Schnur. J. M.; Singh, A. *Chem. Phys. Lipids* **1992**, *62*, 193.

51 Markowitz, M. A.; Baral, S.; Brandow, S.; Singh, A. *Thin Solid Films* **1993,** *224*. 242.

52 Markowitz, M. A.; Schnur. J. M.; Singh, A. *Synthetic Microstructures in Biology;* J. M. Schnur, M. Peckerar., Eds. Plenum: New York, 1992.

53 Kunitake, T.; Nakashima, N.; Shimomura, M.; Okahata, Y.; Kano, K.; Ogawa, T. *J. Am. Chem. Soc.* **1980**, *102*, 6642.

54 Schnur, J. M.; Ratna, B. R.; Selinger, J. V.; Singh, A.; Jyothi, G.; Easwaran, K. R. K. *Science* **1994**, *264*, 945.

55 Spector, M. S.; Easwaran, K. R. K.; Jyothi, G.; Selinger, J. V.; Singh, A.; Schnur, J. M. *Proc. Natl. Acad. Sci. U.S.A.* **1996**, *93*, 12943.

56 Spector, M. S.; Selinger, J. V.; Singh, A.; Rodriguez, J. M.; Price, R. R.; Schnur, J. M. *Langmuir* **1998**, *14*, 3493.

57 Thomas, B. N.; Corcoran, R. C.; Cotant, C. L.; Lindemann, C. M.; Kirsch, J. E.; Persichini, P. J. *J. Am. Chem. Soc.* **1998**, *120*, 12178.

58 Schoen, P.; Yager, P.; Schnur, J. U.S. Patent 852596 (**1986**).

59 Burke, T. G; Rudolph, A. S.; Price, R. R.; Sheridan, J. P.; Dalziel, A. W.; Singh, A.; Schoen, P. E. *Chem. Phys. Lipids* **1988,** *48*, 215.

60 Singh, A.; Burke, T. G; Calvert, J. M.; Georger, J. H.; Herendeen, B.; Price, R. R.; Schoen, P. E.; Yager, P. *Chem. Phys. Lipids* **1988,** *47*,135.

61 Schnur J. M.; *et al.* U.S. Patent 4877501 (**1989**).

62 Rudolph. A. S.; Calvert. J. M.; Ayers, M. E.; Schnur, J. M.; *J. Am. Chem. Soc.* **1989,** *1*, 8516.

63 de Gennes, P.G. *C. R. Acad. Sci. Paris* **1987,** *304*, 259.

64 Chappell, J. S.; Yager, P. *Biophys. J.* **1991,** *60*, 952.

65 Lubensky, T. C.; Prost, J.; *J. Phys. (France) II* **1992,** *2*, 371.

66 Helfrich, W.; Prost, J. *Phys. Rev. A* **1988,** *38*, 3065.

67 Ou-Yang, Z. C.; Liu, J. X. *Phys. Rev. Lett.* **1990,** *65*, 1679.

68 Ou-Yang, Z. C.; Liu, J. X. *Phys. Rev. A* **1991,** *43*, 6826.

69 Chappell, J. S.; Yager, P. *Chem. Phys. Lipids* **1991**, *58*, 253.

70 Yager, P.; Chappell, J.; Archibald, D. D. *Biomembrane Structure and Function—The State of the Art,* B. P. Gaber, K. R. K. Easwaran, Eds.; Adenine: Schenectady, 1992.

71 Nelson, P.; Powers, T. *Phys. Rev. Lett.* **1992,** *69*, 3409.

72 Nelson, P.; Powers, T. *J. Phys. (France) II* **1993,** *3*, 1535.

73 Selinger, J. V.; Schnur, J. M. *Phys. Rev. Lett*. **1993,** *71*, 4091.

74 Tu, Z. C.; Seifert, U. *Phys. Rev. E*. **2007,** *76*, 031603 .

75 Saito, R.; Fujita, M.; Dresselhause, G.; Dresselhaus, M. S. *Mater. Sci. Eng.* **1993**, *019*, 185.

76 Shimizu, T; Masuda, M.; Minamikawa, H. *Chem. Rev.* **2005**, *105*, 1401.

77 Chung, D. S.; Benedek, G. B.; Konikoff. F. M.; Donovan, J. M. *Proc. Natl. Acad. Sci. U.S.A.*, **1993**, *90*, 11341.

78 Ratna, B. R.; Baral-Tosch, S. B.; Rudolph, A. S.; Schnur, J. M. *Chem. Phys. Lipids* **1992**, *63*, 47.

79 Tieke, B.; Wegner, G.; Naegele, D.; Ringsdorf, H. *Angew. Chem.*, **1976**, *88*, 805.

80 Ladik, J.; André, J. M.; Seel, M. *Quantum Chemistry of Polymers—Solid State Aspects.* Dordrecht: Boston, D. Reidel Pub. Co.: Hingham, 1984.

81 de Gennes, P. G. *The physics of Liquid Crystals*; Clarendon: Oxford, 1974.

82 Jerome, B. *Rep. Prog. Phys.* **1991**, *54*, 391.

83 Price, R. R.; Dressick, W. J.; Singh, A. *J. Am. Chem. Soc.* **2003**, *125*, 11259.

84 Patil, A. J.; Muthusamy, E.; Seddon, A. M.; Mann, S. *Ad*v. *Mater.* **2003**, *15*, 1816.

85 Schnur, J. M.; Price, R. R.; Rudolph, A. S. *J. Controlled Release* **1994**, *28*, 3.

86 Meilander, N. J.; Yu, X.; Ziats, N. P.; Bellamkonda, R. V. *J. Controlled Release* **2001**, *71*, 141.

87 de Gennes, P. G. *Rev. Mod. Phys.* **1985**, *57*, 827.

88 Petit, C. A. P.; Carbeck, J. D. *Nano Lett.* **2003**, *3*, 1141.

89 Kim, J. H.; Shi, W. X.; Larson, R. G. *Langmuir* **2007**, *23*, 755.

90 Zhao, Y.; Fang, J. Y. *Langmuir* **2006**, *22*, 1891.

91 Whitehouse, C.; Fang, J. Y.; Aggeli, A.; Bell, M.; Brydson, R.; Fishwick, C. W. G.; Henderson, J. R.; Knobler, C. M.; Owens, R. W.; Thomson, N. H.; Smith, D. A.; Boden, N. *Angew. Chem., Int. Ed.* **2005**, *44*, 1965.

92 Kuncicky, D. M.; Naik, R. R.; Velev, O. D. *Small* **2006**, *12*, 1462.

93 Radmacher, M.; Fritz, M.; Cleveland, J. P.; Walters, D. A.; Hansma, P. K. *Langmuir* **1994**, *10*, 3809.

94 Radmacher, M.; Fritz, M.; Kacher, C.M.; Cleveland, J. P.; Hansma, P. K. *Biophys. J.* **1996**, *70*, 556.

95 Fritz, M.; Radmacher, M.; Petersen, N.; Gaub, H. E. *J. Vac. Sci. Technol. B* **1994**, *12*, 1526.

96 Fotiadis, D.; Scheuring, S.; Muller, S. A.; Engel, A.; Muller, D. J. *Micron* **2002,** 33, 385.

97 Touhami, A.; Nysten, B.; Dufrêne, Y. F. *Langmuir* **2003**, *19*, 4539.

98 Laney, D. E.; Garcia, R. A.; Parsons, S. M.; Hansma, H. G. *Biophys. J.* **1997**, *72*, 806.

99 Matzelle, T. R.; Ivanov, D. A.; Landwehr, D.; Heinrich, L. A.; Herkt-Bruns, C.; Reichelt, R.; Kruse, N. *J. Phys. Chem. B* **2002**, *106*, 2861.

100 Lulevich, V. V.; Radtchenko, I. L.; Sukhorukov, G. B.; Vinogradova, O. I. *J. Phys. Chem. B* **2003**, *107*, 2735.

101 Jiao, Y.; Schäffer, T. E. *Langmuir* **2004**, *20*, 10038.

102 Shulha, H.; Zhai, X.; Tsukruk, V. V. *Macromolecules* **2003**, *36*, 2825.

103 Ivanovska, I. L.; de Pablo, P. J.; Ibarra, B.; Sgalari, G.; Mackintosh, F. C.; Carrascoa, J. L.; Schmidt, C. F. *Proc. Natl. Acad. Sci. USA***. 2004**, *101*, 7600.

104 Landau, L. D.; Lifshitz, E. M. *Theory of Elasticity*, 3rd ed.; Pergamon Press: Oxford, **1986**.

105 Elbaum, M.; Fygenson, D. K.; Libchaber, A. *Phys. Re*V. *Lett*. **1996**, *76*, 4078.

106 Cohen, A. E.; Mahadevan, L. *Proc. Natl. Acad. Sci. U.S.A.* **2003**, *100*, 12141.

107 Frusawa, H.; Fukagawa, A.; Ikeda, Y.; Araki, J. A.; Ito, K.; John, G.; Shimizu, T.

*Angew. Chem., Int. Ed.* **2003**, *42*, 72.

108 Cohen, A. E.; Mahadevan, L. *Proc. Natl. Acad. Sci. U.S.A.* **2003**, *100*, 12141.

109 de Pablo, P. J.; Schaap, I. A. T.; MacKintosh, F. C.; Schmidt, C. F. *Phys. Rev. Lett.* **2003**, *91*, 098101

110 Elbaum, M.; Fygenson, D. K.; Libchaber, A. *Phys. Rev. Lett*. **1996**, *76*, 4078.

111 Gittes, F.; Mickey, B.; Nettletion, J.; Howard, J. *J. Cell. Biol.* **1993**, *120*, 923.

112 Frontali, C.; Bore, E. Ferranto, A.; Gratton, E. *Biopolymers* **1979**, *18*, 1353.

113 Rivetti, C.; Guthold, M.; Bustamante, C. *J. Mol. Biol*. **1996**, *264*, 919.

114 Camesano, T. A.; Wilkinson, K. J. *Biomacromolecules* **2001**, *2*, 1184.

115 Zhao, Y.; Mahajan, N.; Fang, J. Y. *J. Phys. Chem. B* **2006**, *110*, 22060.

116 Persch, G.; Born, C.; Utesch, B. *Microelectron. Eng.* **1994**, *24*, 113.

117 Timoshenko, S. P.; Goodier, J. N. *Theory of Elasticity,* 3rd ed.; McGraw-Hill Book Company: New York, 1970.

118 Miller, R. E.; Shenoy, V. B. *Nanotechnology* **2000**, *11*, 139.

119 Gaines, G. L. *Insoluble Monolayers at Liquid-Gas Interfaces*; Interscience Publishers: New York, 1966.

120 Adamson, A. W.; Gast, A. P. *Physical Chemistry of Surfaces*, 6th ed.; Wiley-Interscience: New York, 1997.

121 Huang, Y.; Duan, X.; Wei, Q.; Lieber, C. M. *Science* **2001**, *291*, 630.

122 Nuzzo, R. G.; Fusco, F. A.; Allara, D. L. J. *J. Am. Chem. Soc.* **1987**, *109,* 2358.

123 Rogers, J. A.; Nuzzo, R. G. *Materials Today* **2005**, *8*, 50.

124 Karlsson, M.; Sott, K.; Cans A-S.; Karlsson, A.; Karlsson, R.; Orwar, O. *Langmuir* **2001**, *17*, 6754.

125 Karlsson, M.; Sott, K.; Davidson, M.; Cans, A.-S.; Linderholm, P.; Chiu, D.; Orwar, O. *Proc. Natl. Acad. Sci. U.S.A.* **2002**, *99*, 11573.

126 Frusawa, H.; Fukagawa, A.; Ikeda, Y.; Araki, J.; Ito, K.; John, G.; Shimizu, T. *Angew. Chem., Int. Ed*. **2003**, *42*, 72.

127 Mahajan, N.; Fang, J. Y. *Langmuir* **2005**, *21*, 3153.

128 Brazhnik, K. P.; Vreeland, W. N.; Hutchison, J. B.; Kishore, R.; Wells, J.; Helmerson, K.; Locascio, L. E. *Langmuir* **2005**, *21*, 10841.

129 Lin, Y. C.; Huang, K. S. *Sensors and Actuators B* **2006**, *117*, 464.

130 Dittrich, P. S.; Heule, M.; Renaud, P.; Manz, A. *Lab. Chip* **2006**, *6*, 488.

131 Nuzzo, R. G.; Allara, D. L. *J. Am. Chem. Soc.* **1983**, *105*, 4481.

132 Love, J. C.; Wolfe, D. B.; Haasch, R.; Chabinyc, M. L.; Paul, K. E.; Whitesides, G. M.; Nuzzo, R. G. *J. Am. Chem. Soc.* **2003**, *125*, 2597.

133 Chen, C. S.; Mrksich, M.; Huang, S.; Whitesides, G. M.; Ingber, D. E. *Biotechnol. Prog.* **1998**, *14*, 356.

134 Whitesides, G. M.; Ostuni, E.; Takayama, S.; Jiang, X.; Ingber, D. E. *Annu. Rev. Biomed. Eng.* **2001**, *3*, 335.

135 Laibinis, P. E.; Whitesides, G. M.; Allara, D. L.; Tao, Y. T.; Parikh, A. N.; Nuzzo, R. G. *J. Am. Chem. Soc.* **1991**, *113*, 7152.

136 Nishi, N.; Hobara, D.; Yamamoto, M.; Kakiuchi, T. *J. Chem. Phys.* **2003**, *118*, 1904.

137 Wenzl, I.; Yam, C. M.; Barriet, D.; Lee, T. R. *Langmuir* **2003**, *19*, 10217.

138 Lee, S.; Puck, A.; Graupe, M.; Colorado, R., Jr.; Shon, Y.-S.; Lee, T. R.; Perry, S. S. *Langmuir* **2001**, *17*, 7364.

139 Park, B.; Chandross, M.; Stevens, M. J.; Grest, G. S. *Langmuir* **2003**, *19*, 9239.

140 Schreiber, F. *Prog. Surf. Sci.* **2000**, *65*, 151.

141 Bensimon, A; Simon, A.; Chiffaudel, A.; Croquette, V.; Heslot, F.; Bensimon, D. *Science* **1994,** *265*, 2096.

142 Gueroui, Z.; Place, C.; Freyssingeas, E.; Berge, B. *Proc. Natal. Acad. Sci. U.S.A*. **2002,** *99*, 6005.

143 Zhao, Y., Mahajan, N. & Fang, J. Y. *J. Phys. Chem. B* **2006**, *110*, 22060.

144 Archibald, D. D.; Mann, S. *Nature* **1993**, *364*, 430.

145 Jung, J. H.; Kobayashi, H.; Masuda, M.; Shimizu, T.; Shinkai, S. *J. Am. Chem. Soc.* **2001**, *123*, 8785.

146 Price, R. R.; Dressick, W. J.; Singh, A. *J. Am. Chem. Soc.* **2003**, *125*, 11259.

147 Patil, A. J.; Muthusamy, E.; Seddon, A. M.; Mann, S. *Adv. Mater.* **2003**, *15*, 1816.

148 Dang, T. X.; Farah, S. J.; Gast, A.; Robertson, C.; Carragher, B.; Egelman, E.; Wilson-Kubalek, E. M. *J. Struct. Biol.* **2005**, *150*, 90.

149 Zhou, Y.; Ji, Q.; Masuda, M.; Kamiya, S.; Shimizu, T. *Chem. Mater.* **2006**, *18*, 403.

150 Ying, J. Y.; Mehnert, C. P.; Wong, M. S. *Angew. Chem., Int. Ed.* **1999**, *38*, 56

151 van Bommel, K. J. C.; Friggeri, A.; Shinkai, S. *Angew. Chem., Int. Ed.* **2003**, *42*, 980

152 Dujardin, E.; Blaseby, M.; Mann, S. *J. Mater. Chem.* **2003**, *13*, 696

153 Baral, S.; Schoen, P. *Chem. Mater.* **1993**, *5*, 145.

154 Jung, J. H.; Lee, S. H.; Yoo, J. S.; Yoshida, K.; Shimizu, T.; Shinkai, S. *Chem.-Eur. J.* **2003**, *9*, 5307.

155 Ji, Q.; Iwaura, R.; Kogiso, M.; Jung, J. H.; Yoshida, K.; Shimizu, T. *Chem. Mater.* **2004**, *16*, 250.

156 Seddon, A. M.; Patel, H. M.; Burkett, S. L.; Mann, S. *Angew. Chem., Int. Ed.* **2002**, *41*, 2988.

157 Letellier, D.; Sandre, O.; Menager, C.; Cabuil, V.; Lavergne, M. *Meter. Sci. Eng. C* **1997**, *5*, 153.

158 Yang, B.; Kamiya, S.; Shimizu, Y.; Koshizaki, N.; Shimizu, T. *Chem. Mater.* **2004**, *16*, 2826.

159 Schnur, J. M.; Price, R. R.; Rudolph, A. S. *J. Controlled Release* **1994**, *28*, 3.

160 Meilander, N. J.; Pasumarthy, M. K.; Kowalczyk, T. H.; Cooper, M. J.; Bellamkonda, R. V. *J. Controlled Release* **2003**, *88***,** 321.

161 Rudolph, A. S.; Burke, T. G. *Biochim. Biophys. Acta* **1987**, *902*, 349.

162 Petrov, A. G.; Spassova, M.; Fendler, J. H. *Thin Solid Films* **1996**, *285*, 845.

163 Lvov, Y. M.; Price, R. R.; Selinger, J. V.; Singh, A.; Spector, M. S.; Schnur, J. M. *Langmuir* **2000**, *16*, 5932.

164 Brinker, C. J.; Schere, G. W. *Sol-Gel Science. The Physics and Chemistry of Sol-Gel Processing*; Academic Press: New York, 1990.

165 Mi, X. D.; Yang, D. K. *Phys. Rev. E* **1998**, *58*, 1992.

166 Fazio, V. S. V.; Komitov, L.; Radüge, C.; Lagerwall, S. T.; Motschmann, H. *Eur. Phys. J. E* **2001**, *5*, 309.

167 Cladis, P. E.; Kleman, M.; *J. Phys. (Paris)*. **1972**, 33, 591.

168 Meyer, R. B. *Philos. Mag*. **1973**, *27*, 405.

169 Allender, D. W.; Crawford, G. P.; Doane, J. W. *Phys. Rev. Lett*. **1991**, *67*, 1442.

170 Kralj, S.; Žumer, S. *Phys. Rev. E.* **1995**, *51*, 366.

171 Mahajan, N.; Fang, J. Y. *Langmuir* **2005**, *21***,** 3153.